UNIVERSITA' DEGLI STUDI DI NAPOLI
FEDERICO II

Scuola Politecnica e delle Scienze di Base
Area Didattica di Scienze Matematiche Fisiche e Naturali

INTERNATIONAL PHD SCHOOL IN NOVEL TECHNOLOGIES FOR MATERIALS, SENSORS AND IMAGING

XXVIII cycle

Coordinatore: Prof. Antonio Cassinese

Methods for therapeutic optimization in radiation therapy: from dose measurement to NTCP modelling

Settore Scientifico Disciplinare FIS/07

Tutors:
Dott.ssa Laura Cella
Prof.ssa Mariagabriella Pugliese

Dottorando:
Vittoria D'Avino

Academic Year 2014-2015

Contents

Introduction

The present work has been performed at the Institute of Biostructure and Bioimaging (IBB) of the National Research Council (CNR) in cooperation with the Institute of Optics (INO) with a joint research project on “Detection of ionizing Radiation by means of intrinsic OPtical fiber Sensors” (DROPS). The research activity has been supported by investigators working at the Departments of Advanced Biomedical Sciences and of Physics of Federico II University.

The rationale of the research activity lies on the Radiation Therapy (RT) optimization issue. As advances in Radiotherapy technology have increased the complexity of a radiotherapy treatment, accurate dose monitoring must be performed, and organ response to the interaction of ionizing radiation must be well understood, in predicting and optimizing the effects of radiotherapy treatments. The research activity focuses on two topics of the optimization problem:

- development of new optical fiber sensor dosimeters and investigation of standard dosimeters for small field and *in vivo* dosimetry;
- dose optimization to the organs at risk.

The modern techniques usually use small fields or composite fields consisting of a multitude of small fields (<1 x 1 cm^2 or smaller). Conventional reference dosimetry is usually based on the absorbed dose to water calibration at 10x10 cm^2 fields as described in the standard dosimetry protocols. A standard protocol for small field dosimetry currently does not exist. Hence, adapted clinical reference dosimetry methods and appropriate dosimeters are required to establish an adequate quality assurance program to guarantee a standard of quality in novel technique applications.

The goal of DROPS is to realize a passive detector for ionizing radiation based on optical fiber sensor technology suitable for radiation dosimetry in a dose range relevant to clinical practice.

The presence of a radiation field significantly affects the fiber physical properties as well, introducing a modification of the optical signal itself. One of the effects of radiation exposure is well known to be an increase in optical transmission loss. Also, a correlated change of average refractive index occurs in the optical

waveguide, which can be exploited to extract the desired information. At the same time, immunity to electromagnetic interference, intrinsic safety, mechanical simplicity and small size as well as multiplexing and embedding capability make optical fiber sensors, in principle, ideal dosimeters.

The modern radiation treatments improves the dose conformality and the dose escalation to the target, however radiation induced toxicities to the surrounding healthy tissues remain major dose-limiting factors. The ultimate goal of radiotherapy treatment planning is to find a treatment that will yield a high tumor control probability (TCP) with an acceptable normal tissue complication probability (NTCP). In this framework, radiobiological models play an essential role and NTCP modeling may help to minimizes side effects for individual patients. Traditionally radiotherapy outcomes have been modelled using information about the dose distribution and the fractionation. Most well-known and accepted models for predicting toxicity after radiation treatment are based only on dose-volume parameters. Our basic idea is to perform "clinical" radiation biology studies through the development of robust predictive NTCP models. In the era of personalized evidence-based medicine, a data-driven multivariable modeling approach for prediction of radio-induced complication may represent a more effective and powerful approach to improve outcomes prediction.

In the general framework of RT treatment optimization, aim of the present research was to analyze the feasibility of developing a new generation of dosimeters based on passive optical fiber sensor. In addition, thermoluminescent dosimeters (TLDs), were evaluated for non-conventional treatment modalities, such as the Intraoperative Electron Radiation Therapy characterized by high dose-per-pulse electron beams. Lastly, multivariable NTCP predictive models for different cancer patients and organ at risks were developed and validated.

The structure of the thesis can be summarized as follow:

Chapter 1 describes the emerging radiotherapy techniques and the state of the art of the dosimeters for small field and *in vivo* dosimetry. Dosimetric aspects of non-conventional beams are discussed with a specific focus on water equivalence of the dosimetric material. In order to elucidate the relationship between radiation dosimetry and radiation therapy, the basic principles of treatment planning algorithms and the equations describing NTCP models are presented.

The aim of the Chapter 2 is to present the physical basis for ionizing radiation detection using Fiber Bragg Grating (FBG) sensors.

Chapter 2 provides an overview of the theory of the photosensitivity of the optical fiber sensor. Particularly, the main intrinsic and extrinsic defects and the theories proposed to explain photosensitivity of Ge-doped silica are illustrated.

The Chapter 3 is focused on the materials and methods description. It is structured in two sections: the first part presents the characteristics of FBG sensors and resonant cavities and the experimental set up for the irradiation and interrogation of the sensors, the second part presents the computational approaches to estimate the complication probability in the normal tissue organs using open source software packages and in-house made code packages.

The Chapter 4 shows the results and the discussions of the research activity. The first part describes the investigation of different dosimeters. The water equivalency assessment of the new optical fiber sensor has been performed modelling the interaction of ionizing radiation with fiber material. The radiological properties have been carried out, including electron density, photon interaction probabilities, mass attenuation and energy absorption coefficients and the effective atomic number. The results concerning the response of the optical fiber sensor to the irradiation with photon beam at different dose levels are presented. Finally the TLD-100 dose-response curves, obtained in high dose-per-pulse electron beams are reported. The second part presents the multivariable NTCP models developed for several patient cohorts, organ at risks and complications developed after radiation treatment.

On the base of the obtained results, the most relevant conclusions, as well as the future perspectives, are illustrated.

CHAPTER 1

Radiation Therapy Optimization

The rationale of the research activity will be given in this Chapter with an overview on the modern radiotherapy techniques and on the physical aspects of dose measurement.

The theoretical background of dose calculation for a radiotherapy prescription and the current models used to optimize and to evaluate a treatment planning will be discussed.

1.1 Background

In applications of ionizing radiation to problems related to medicine it is important to measure the amount of delivered radiation. In diagnostic procedures, such as x-ray examinations, nuclear medicine, CT scans, PET, and in radiation therapy, this measurement aims both at the optimization of image quality and radiation protection.

The evaluation of accuracy and precision of determination of absorbed dose is a very important component of any physical quality assurance program in radiation therapy for cancer. One of the aspects of an efficient treatment of cancer is the calibration of the clinical accelerator machines (reference dosimetry), but also accurate radiation beam shaping and measurement of dose delivered to the patient (relative and *in-vivo* dosimetry) must be taken into account.

An active area of research consists in treatment optimization taking into account the almost infinite variety of treatments possible with modern computer-controlled medical accelerators [1]. While the use of dosimetry based on biological response is the long term goal, practical clinical dosimetry today is based on the quantity of absorbed dose and its accurate measurement represents one of the major responsibilities of medical physicists.

Due to the development of new techniques in radiotherapy, such as Intensity Modulated Radiation Therapy (IMRT), Stereotactic Radiotherapy and Hadrontherapy, there is a growing need to more reliably measure the absorbed dose.

In vivo dosimetry is used to control the total accumulated dose in cases where the treatment planning system is less accurate, such as in the build-up region and in risk organs in the head and neck region. Small changes in absorbed dose could result in a significant change in the probability of cure and/or complications. The recent developments in radiotherapy delivery techniques have substantially increased the use of non-standard fields. A non-standard field is defined as a field with a size smaller than the lateral range of charged particles (*small field*) or whenever non-equilibrium conditions exist [2].

With the accepted need for accurate delivery of dose, development of novel instrumentation and more reliable techniques that ensure accurate dose measurements is of primary importance. In this context a new generation of optical fiber-based dosimeter would transmit dose information through optical fibers. Such sensors are immune to electromagnetic interference, which can be a serious issue for many electronic dosimeters. The ability of remotely monitor radiation is an additional advantage as the sensor can be placed at a long distance from the readout electronics. Also, optical fiber sensors can be multiplexed so that a single reading unit can control several sensors. Thanks to their mechanical nature and very small size, fibers lend themselves to the realization of miniature radiation detectors with different geometries without perturbing the dose measurement.

1.2 Emerging radiotherapy techniques

Modern external radiotherapy techniques are designed to improve the dose conformality and the dose escalation to the target. Some examples are summarized below.

Intensity modulated radiotherapy (IMRT): is a technique which uses the multi-leaf collimators (MLC) on a linear accelerator to vary the radiation beam intensity around a target field. The shape of the radiation beams may change hundreds of times during the course of treatment, together with the intensity of the beams and the direction from which they are delivered. IMRT permits the delivery of high radiation dose to the target while minimizing it to other sensitive organs by focusing multiple beams on the tumor. Each of these beams has a number of small

sub-beams or segments whose intensities are varied according to the treatment plan [3-5]. IMRT treatments can be delivered with the MLC operating in one of three basic modes:

- segmented MLC (static IMRT) in which the fields are delivered with a sequence of small segments or subfields, each subfield with a uniform intensity. The techniques is also referred to as step and shoot, implying that the beam is only turned on when the MLC leaves are stationary in each of the prescribed subfield positions;
- dynamic MLC mode in which the intensity modulated fields are delivered in a dynamic fashion with the leaves of the MLC moving during the irradiation of the patient. For a fixed gantry position the opening formed by each pair of opposing MLC leaves is swept across the target volume under computer control with the radiation beam turned on to produce the desired fluence map;
- intensity modulated arc therapy (IMAT) in which the sliding window approach is used as the gantry rotates around a patient.

Intraoperative radiotherapy (IORT): this technique delivers in a single session a radiation dose of the order of 10 - 20 Gy to a surgically exposed internal organ, tumor or tumor bed. Thus IORT combines two conventional modalities of cancer treatment, surgery and radiotherapy. Typically, when surgical resection of a tumor mass is finally attempted, not all the tumor can be removed without significant morbidity. To improve local regional control, a large dose of radiation is delivered during the surgical procedure, helping kill microscopic disease and preserving more healthy tissue.

Stereotactic external beam irradiation (SEBI): is a technique that uses small, highly-collimated photon beams to irradiate tumor target with high geometric precision and dosimetric accuracy. This technique is most commonly used for tumors in the brain or spinal column, in the lung, liver, pancreas and kidney.
It is divided into two categories:

- stereotactic radiosurgery: the total dose is delivered in a single session;
- stereotactic radiotherapy: like in standard radiotherapy, the total dose is delivered in multiple fractions, typically in a maximum of five sessions using higher doses of radiation with each session. Instead, a focused high-intensity beam of radiation is used to target the tumor.

1.3 Dosimetry of small photon field

The photon fields used in the conventional RT are commonly referred to as *standard* or *large* fields. Their sizes are larger than 5 x 5 cm^2. In modern radiotherapy narrow high-energy photon beams are increasingly used. There is no clear consensus definition as to what constitutes a *small field*. At present a small field is generally defined as having dimensions smaller than the lateral range of the charged particles that contribute to the deposited dose at a point along the central axis. According to these criteria, field sizes of less than 3 x 3 cm^2 are considered to be small for a 6 MV photon beam.

In order to apply these modern RT techniques with high precision and in a trusted manner, accurate measurements of the dose characteristics of such beams (percentage depth dose, beam profiles, output factors) are required as input to the treatment planning system. Small photon beam measurements are problematic mainly due to the presence of high dose gradients and nonexistence of lateral electronic equilibrium in narrow photon beams. It has been proposed that good practice is to use and compare several types of dosimeters. To that end, a large number of investigators have used air and liquid ionization chambers, radiographic and Gafchromic films, diamond detectors, plastic scintillators, TLDs (ThermoLuminescent Dosimeters), MOSFETs (Metal Oxide Semiconductor Field Effect Transistors), radiophotoluminescence glass plates, polymer gels, and silicon diodes for measuring small field profiles analyzing the advantages and disadvantages of each dosimeter. In addition, Monte Carlo simulations have often used for theoretical verification of experimental results. The available dosimetry equipment along with their typical uses and response characteristics are listed in Appendix A, Table A1 [6].

To our knowledge, no single detector, fulfils all the requirements. Moreover, the dosimeters used for dose measurements in small filed, should ideally exhibit certain characteristics such as (i) being tissue-equivalent and not perturbing the radiation beam, (ii) exhibiting energy, dose rate, and directional independence of response, (iii) having small sensitive volume and ability for high spatial resolution measurements, and (iv) overcoming the positioning problems that are usually present in small field dosimetry.

Usually, the dose profiles for fields smaller than 5 mm in diameter change drastically over off-axis distance as small as 1 mm. Thus, the resolution of the

detector used will have a great impact on both the central axis and off-axis dose measurements.

There are two different approaches to solving this problem: (i) we either need a detector with a well-known geometry or (ii) we need a detector with a very small size, at least 6 to 7 times smaller than the field size. Evidently, it is difficult to manufacture a detector small enough and accurate at the same time when, for example, the field size is as small as 2 mm in diameter. However, if the exact geometry of the detector sensitive volume is known, it is possible to perform a deconvolution procedure that is very suitable for off-axis measurements. Several extensive studies on dose profile deconvolution have been conducted [7, 8].

The property of water-equivalence of the measuring material is related to the radiation properties, since water is the most commonly used phantom material, similar to the human body tissue. Having a water-equivalent detector is important, because the concept of the charged particle equilibrium (CPE) does not apply to small photon fields in a lateral direction. In order to illustrate the importance of this concept, let us take a closer look at how the radiation dose gets deposited in the phantom when small photon beams are used.

When a high-energy photon enters a medium, there are four main types of interactions with a certain probability: *photoelectric effect, coherent scatter, incoherent (Compton) scatter, and pair production*. The radiation dose deposited is as a result of two-step process: after the interactions, a significant part of the incident photon energy might be transferred to an electron that thereafter will be set in motion. This electron will then ionize the medium over its track by electron-electron Coulomb interactions.

The radiation dose deposited is expressed as follow:

$$D = \phi \left(\frac{\bar{L}}{\rho}\right) \tag{1.1}$$

where ϕ is the electron fluence at the point-of-interest and $\left(\frac{\bar{L}}{\rho}\right)$ is the restricted mass stopping power averaged over the electron energy spectrum.

The restricted mass stopping power is defined as:

$$\left(\frac{\bar{L}}{\rho}\right) = \frac{1}{\rho}\frac{\Delta E}{\Delta x} \tag{1.2}$$

where ρ is the density of the medium and ΔE is the energy transferred to low-energy electrons that deposit this energy locally, over a small distance Δx.

For large photon fields, the assumption is made that the number of electrons that stop inside a small volume ΔV is equal to the number of electrons set in motion by photons inside the same volume (Figure 1.1). Thus, the electrons can be considered as continuously moving through the medium, instead of stopping and being set in motion. This assumption actually underlines the concept of CPE. The electron fluence is constant when this concept applies.

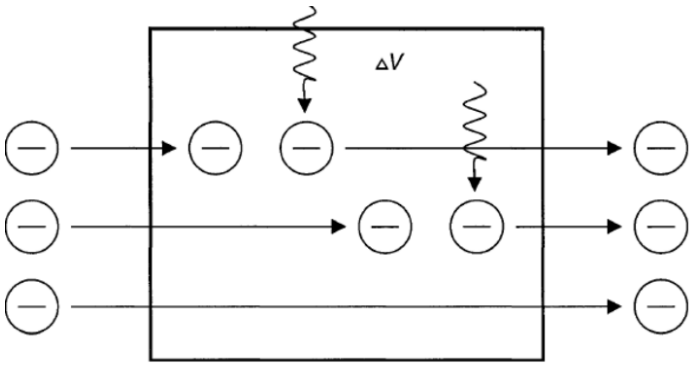

Figure 1.1. Charged particle equilibrium: number of electrons stopped in a small volume is equal to the number of electrons set in motion by photons in the same volume.

Generally, the detectors and the phantoms are made of different materials. According to Eq. (1.1) the relationship between the dose delivered to the detector, D_d, and the dose delivered to the medium, D_{med}, is:

$$D_{med} = D_d \left(\frac{\bar{L}}{\rho}\right)_d^{med} (\phi)_d^{med} \tag{1.3}$$

where

$$\left(\frac{\bar{L}}{\rho}\right)_d^{med} = \frac{\left(\frac{\bar{L}}{\rho}\right)_{med}}{\left(\frac{\bar{L}}{\rho}\right)_d}$$

$$(\phi)_d^{med} = \frac{\phi_{med}}{\phi_d}$$

The dose to the phantom (medium) is calculated by multiplying the dose to the detector by two correction factors: restricted stopping power ratio and the electron fluence perturbation factor for the two materials: medium and detector. The

restricted stopping power ratio accounts for the difference in the energy deposited by an electron per unity track length in the two difference materials. The electron fluence perturbation factor corrects for the difference in the electron fluence.

Under condition of CPE, the two factors are constant as given photon energy, so that, even if they are not established, relative measurements may be carried out without adversely affecting the reliability of measurements results. For very small fields, the field size is usually smaller than the electron range in the phantom material. In this situation a very important difference appears when comparing an electron moving in a lateral direction in a very small field to an electron moving in the same fashion in a large field (Figure 1.2). When an electron moving laterally in a large photon field approaches the point where it will stop, another electron will be set in motion by a photon in the vicinity of this point. In a very small field, many electrons will be able to reach points outside the photon beam where no photon-electron interaction occurs, and the electron fluence will change with the increase in the off-axis distance. Thus there will be no CPE in a lateral direction, leading to the conclusion that the correction factors defined in Eq. (1.3) will vary causing difficulties not only for absolute measurements, but even for relative dosimetric measurements. In order to overcome this obstacle and to obtain reliable results one would therefore need either a phantom-equivalent detector with both correction factors to one or else a detector whose correction factors are precisely known.

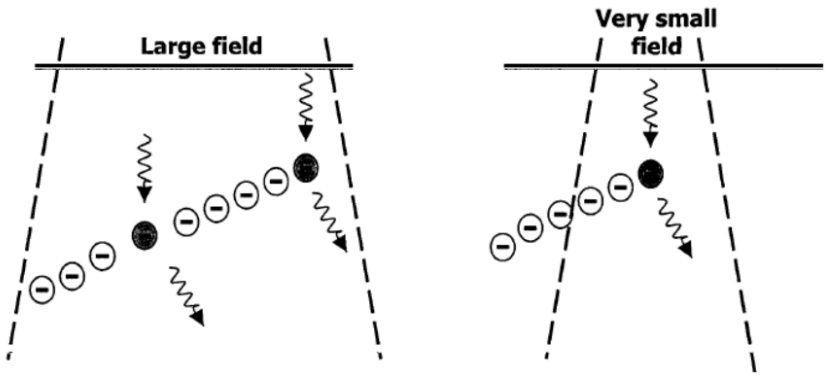

Figure 1.2. Electrons moving in lateral direction in large and very small photon fields.

At the frontier of Ionizing Radiation (IRs) monitoring optical fiber sensors have emerged in the recent years. Immunity to electromagnetic interference, intrinsic safety, mechanical simplicity and small size as well as multiplexing and embedding capability make optical fiber sensors, in principle, ideal dosimeters. The majority

of existing optical fiber detectors are extrinsic sensors, where fibers mainly serve to transmit light from the sensor's head, whether it be a thermoluminescent solid, diode, or scintillating medium.

In this thesis a different approach for detection of IRs down to clinical dose levels was exploited: the optical fibers sensors are totally passive, based on special Bragg-grating cavity reflectors which are particularly sensitive to radiation-induced effects in the silica material. Because the interaction properties play a fundamental role in the radiation effect as well as in the performance of a dosimeter, prior to perform experimental dose measurements the sensors have been characterized with respect the peculiarities of interaction of ionizing radiation with the material.

1.4 *In vivo* dosimetry

In vivo dosimetry is a suitable tool to detect errors in radiotherapy, to assess clinically relevant differences between the prescribed and delivered doses and to document doses received by individual patients. The primary goal of *in vivo* dosimetry, however, is Quality Assurance (QA) of the radiotherapy process.

There is no general consensus among radiotherapy centers on the cost effectiveness of *in vivo* dosimetry, and until recently its routine implementation was not widespread. Arguments are made that most treatments are carried out in a correct manner and that only a small fraction of patients actually benefit from rectifying errors, because very few are detected. However, a recent series of major accidents in radiotherapy, which would have been prevented if *in vivo* dosimetry systems had been in place, has strengthened the reasoning in favor of *in vivo* dosimetry. It is now more broadly considered that preventing the severe consequences of serious errors justifies the effort and costs of *in vivo* dosimetry programs. This has generated an increasing interest among radiotherapy centers in the methodology for *in vivo* dosimetry.

The IAEA (International Atomic Energy Agency) initiated a coordinated research project (CRP) entitled "Development of Procedures for In vivo Dosimetry in Radiotherapy" in 2005 [9]. The emphasis of the CRP was on patient dose studies, both evaluating the clinical value of *in vivo* dosimetry and comparing different techniques for *in vivo* dosimetry in a clinical setting.

Many different types of dosimeters have been investigated for in-phantom or *in vivo* dose measurements in diagnostic radiology, including ionization chambers,

metal-oxide semiconductor field-effect transistor dosimeters, thermoluminescent dosimeters, optically stimulated luminescence dosimeters, films and diodes. With the exception of the ionization chamber, each of the before mentioned dosimeters suffers from a critical limitation, either the need to interrogate, or read, the dosimeter to retrieve dose information or large size to achieve adequate sensitivity. During this interrogation, no dose information is collected, and so accurate real-time monitoring of accumulated radiation dose is not possible.

While the ionization chamber is not subject to the same limitation, the size of chamber necessary for rapid, reproducible and accurate dose measurement prohibits its use for in-phantom or *in vivo* dose measurements in diagnostic radiology. Thus, new forms of dosimetry are required to accurately measure accumulated dose in clinically relevant settings.

Actually MOSFET, diodes and TLDs are the well-established methods used for *in vivo* dosimetry.

MOSFET it is relatively new in radiotherapy being introduced into radiation therapy dosimetry in the early 1990s [10, 11]. MOSFETs are particularly useful in high dose gradient radiation fields because of their small size. This feature provides a good spatial resolution of measurements, especially important in IMRT, radiosurgery and brachytherapy. MOSFETs offer some other advantages for clinical dosimetry such as the possibility of real time readout, simple instrumentation and robustness. In addition, dual MOSFET dual voltage dosimeters are temperature independent, which is an advantage in clinical dosimetry. MOSFETs also allow for permanent dose storage, since there is little fading of the signal with time. However, MOSFETs have a limited lifetime, which depends on the thickness of the silicon oxide layer and the mode they are used in.

TL detectors have the advantage of being highly sensitive under a very small volume and not to have to be connected to an electrometer with an unwieldy cable. Their major disadvantage which is the time required for readout can be considerably decreased by a good choice of the equipment and a good methodology. Thanks to the modern automated readers TLD results may now be obtained within some 15 minutes after irradiation. Even with the multichannel electrometers presently available for diode dosimetry, the number of sites to be explored may sometimes become too large (e.g. for dose evaluation at different places in large fields as applied in TBI or total skin irradiation). Thanks to the very high number of detectors available and to the absence of cables TLD offers attractive possibilities.

Due to the limited size of the detectors and therefore their excellent spatial resolution, another typical application of TLD is the exploration of zones of possibly high dose gradient. It is then possible to study e.g. field junction zones by juxtaposing on the patient's skin a number of TLD chips, or a number of small containers to be filled with TLD powder. Dose distributions at the entrance or exit surfaces of the 2 adjacent fields may then be derived with a high spatial resolution.

Thanks to their tissue-equivalence TLD are also of interest for measurements outside the field, because, despite the spectral variations with in-field positions, the calibration factor derived at the beam axis may still be used with a reasonable accuracy.

Although, TLDs are a well-established technique for *in vivo* dose verification, very few works have been published about the dose evaluation during electron irradiation [12-14].

Diode dosimeters, which belong to the category of semiconductor detectors, are comparable to ionization chambers but are generally used without external bias voltage and are more sensitive for the same detection volume. Diodes score better than TL dosimeters with respect to immediate response, share the advantage of absence of high voltage, but are inferior with respect to presence of a cable, response variation as a function of accumulated dose, dose-rate, temperature and energy.

1.5 Treatment planning dose calculation

In order to elucidate the relationship between radiation dosimetry and radiation therapy, the basic principles on which treatment planning algorithms are based are briefly described. The radiation dose delivered to an arbitrary point (a point-of-interest) in a phantom or a patient is calculated by multiplying the dose to a certain point, called a reference point, with a coefficient, which related the dose at a reference point to the dose at the point-of-interest. We need to know both the absolute dose delivered to the reference point and the relationship between this dose and the dose to the point-of-interest to perform this calculation.

Conventional reference dosimetry is usually based on the absorbed dose to water calibration at 10 x 10 cm^2 fields as described in the protocols AAPM TG-51 defined by the American Association of Physicists in Medicine and IAEA TRS-398 defined by the Atomic Energy Agency [15, 16].

Dose measurements with ionization chambers rely on the assumptions of cavity theory [17]. When the size of the cavity is smaller than the range of charged particles originated in the medium, the cavity is treated as non-perturbing. In such a situation, the dose to the medium is related to the dose to the air in the cavity by the stopping power ratios of medium to air. Under electronic equilibrium, cavity theory describes a method to calculate the dose (D) in a medium based on measured charge in the cavity:

$$D_t = \left(\frac{Q}{m}\right)\left(\frac{\overline{W}}{e}\right)\left(\frac{S}{\rho}\right)_a^t \tag{1.4}$$

$$\frac{D_t(r)}{D_t(ref)} = \left(\frac{D_t(E,r)}{D_t(ref)}\right)\left(\frac{\overline{W}}{e}\right)_{ref}^{r}\left(\left(\left(\frac{S}{\rho}\right)_a^t\right)\right)_{ref}^{r} \tag{1.5}$$

where Q is the detector reading of charge, m is mass of the air in an ion chamber, $\frac{W}{e}$ is ionization potential of air, r is the field dimension, *ref* is reference field size and $\left(\frac{S}{\rho}\right)_a^t$ is the mass collision stopping power ratio of tissue (r) to air (a). All the parameters in Eq. (1.5) are energy dependent; hence, the dose in small field compared to the reference or calibrated field (10 x 10 cm^2) is uncertain due to spectral variations.

The measured ionization readings $Q(E,r)$ are influenced by many factors as shown below:

$$Q(E,r) = Q_m\, P_{ion}\, P_{repl}\, P_{wall}\, P_{cec}\, P_{pcf} \tag{1.6}$$

where Q_m is the measured reading, P_{ion} is the ion recombination, P_{repl} is the replacement correction factor, P_{wall} is wall correction factor, P_{cec} is the central electrode correction factor, and P_{pcf} is the perturbation correction factor as described in TG-21 [15]. Usually the ratio of these correction factors as shown in Eq. (1.5) is ignored in routine clinical practices where CPE exists, but they cannot generally be ignored for small fields, as noted by Seuntjens and Verhaegen and Sauer and Wilbert [18, 19].

Linac is adjusted in such way that the maximum dose rate delivered over the central axis of the radiation beam for field size of 10 x 10 cm² and a source-surface distance (SSD) of 100 cm is 1 cGy/1 Monitor Unit (MU). One monitor unit corresponds to a given amount of electrical charge collected by the monitor ionization chamber embedded in the linac treatment head.

Central axis dose distributions inside the patient or phantom are usually normalized to $D_{max} = 100$ % at the depth of dose maximum d_{max} and then referred to as the percentage depth dose (PDD) distributions. The PDD depends on four parameters: depth in phantom d, field size A, source-surface distance $SSD = f$, and photon beam energy hv. The PDD is thus defined as follow:

$$PDD(d, A, f, hv) = 100\ x\ \frac{D_Q}{D_P} \tag{1.7}$$

Point Q is an arbitrary point at depth d on the beam central axis; point P represents the specific dose reference point at $d = d_{max}$ on the beam central axis.

In modern radiotherapy, the treatments are mostly done using isocentric setups, which means that the center of the Planning Target Volume (PTV) is placed at the linac isocenter. Another approach is the so called source-axis-distance (SAD) setups. The function used for this purpose is the Tissue Maximum Ratio (TMR), defined as

$$TMR\left(d, A_Q, hv\right) = \frac{D_Q}{D_{Q_{max}}} \tag{1.8}$$

where D_Q is the dose in phantom at arbitrary point Q on the beam central axis and $D_{Q_{max}}$ is the dose in phantom at depth d_{max} on the beam central axis.

A typical algorithm for calculating the dose to a certain point-of-interest is given in the block diagram in Figure 1.3. It is necessary to obtain very precise data in order to calculate a dose distribution with very low uncertainties.

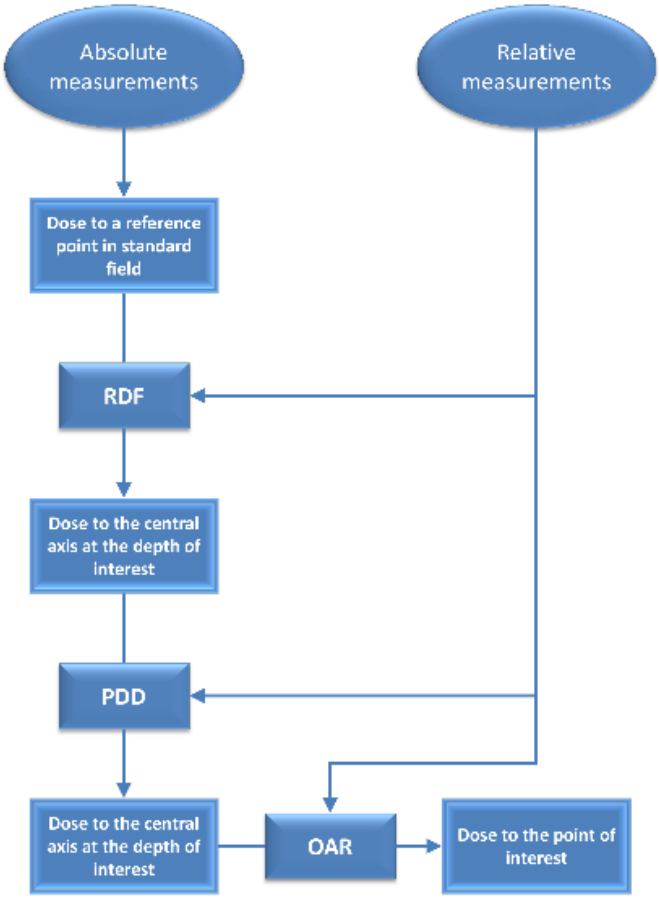

Figure 1.3. Basic treatment planning algorithm. The RDF (Relative Dose Factor) is defined as the ratio of the dose at P in phantom for field size A to the dose at P in phantom for a 10 x 10 cm² field. The Off-Axis Ratio (OAR) function shows how the dose changes in lateral direction with respect to the dose delivered to the point on the central axis at the same depth.

1.6 Treatment planning evaluation and optimization

In radiotherapy, a large dose of radiation is released to a tumor and the effectiveness of the treatment depends on delivering the dose with an accuracy of 3% or better in some situations [20]. The dose-response curve in radiation therapy is quite steep in certain cases, and there is evidence that a 7 - 10% change in the dose to the target volume may result in a significant change in tumor control probability [21].

As shown in Figure 1.4, the tumor control probability (TCP) (curve A) and the normal tissue complication probability (NTCP) (curve B) are sigmoid curves.

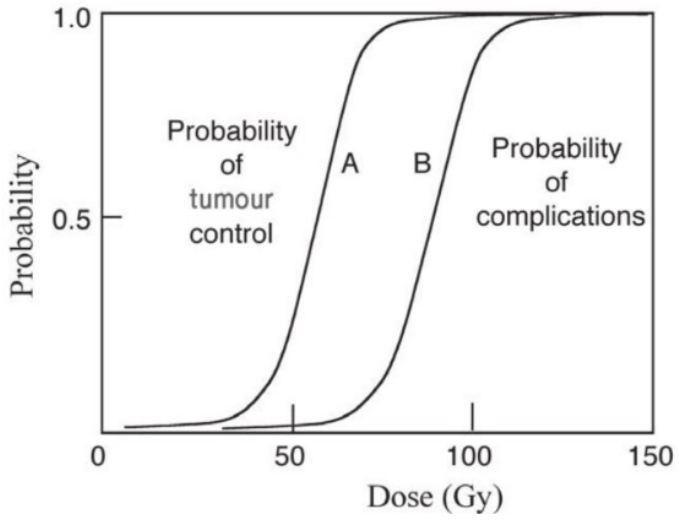

Figure 1.4. The principle of therapeutic ratio. Curve A represents the TCP, curve B the probability of complications.

Today the treatment planning is not based upon optimization of TCPs and NTCPs, but rather upon meeting physical dose and volume constraints. The QUANTEC (QUantitative ANalysis of normal Tissue Effects in the Clinic) summarizes the available 3D dose–volume/outcome data [22, 23] to update and refine the normal tissue dose/volume tolerance guidelines provided by the classic "Emami" paper [24]. A summary of organ-specific dose/volume/outcome data, based on the QUANTEC reviews, is included in Appendix B, Table B.1.

The scientific community agrees on the point that the treatment planning evaluation and optimization would be more effective if they were biologically and not dose/volume based [25]. Furthermore, to properly use NTCP and TCP models, new protocols need to be written and established which allow for greater treatment customization based on the anatomical details of each patient's case. On the other hand the era of modern radiotherapy has opened the way for patient-specific, individualized treatment planning decision, improving the predictive capability of NTCP models.

Early NTCP models, like the Lyman-Kutcher-Burman (LKB) [1, 26-28] and the Relative Seriality (RS) model [29], involve only dose-volume parameters of a single organ at risk (OAR). However, the risk of complications may depend on more factors than only dose to a single organ, both dosimetric and clinical (e.g. organ volume, hormonal therapy, age, gender, diabetes, smoking, chemotherapy, clinical stage). For example, radiation-induced lung toxicity may be related to radiation dose to both the lung and the heart [30-33]. In the recent years multivariable

logistic modelling of radiotherapy outcomes, including dose-volume and clinical factors, have been developed demonstrating the improved predicted power respect to the traditional models [34-38].

The LKB model is probably the most well know method for predicting NTCP for a radiotherapy treatment plan. The model was developed by Lyman for heavy charged particle beams where partial volumes of homogenous dose could be achieved and adapted for conventional radiotherapy through the histogram reduction work of Kutcher et al. [27, 28], and parameter values of Emami et al. [24] and Burman et al. [27].

In the LKB model the interrelation of the variables can be described by the following equation:

$$NTCP_{LKB} = \int_{-\infty}^{t} exp\left(\frac{-u^2}{2}\right) du \tag{1.9}$$

$$t = \frac{gEUD - D_{50}}{mD_{50}} \tag{1.10}$$

$$gEUD = \left(\sum_i v_i \, d_i^{\frac{1}{n}}\right)^n \tag{1.11}$$

where D_{50} is the value of the dose corresponding to the 50% probability to induce normal tissue complication, the parameter m is inversely proportional to the slope of dose-response curve, the parameter n can assume values in the range 0 - 1 and accounts for volume effect of the organ, v_i is the relative volume that receives the dose d_i, the sum is over all the bins of DVH. $gEUD$ stands for '*generalized equivalent uniform dose*', a concept introduced by Nimierko [39] to take into account the heterogeneous dose distributions: the gEUD is the dose that, if given uniformly to the entire organ, is believed to yield the same complication rate as the true dose distribution.

The RS model is based on Poisson model of cell survival to evaluate non-uniform irradiation of OARs from fractionated radiotherapy. A new parameter called the "relative seriality" or "s" parameter is used to take into account the complex structural and functional organization of OARs as well as of tumor tissues. In the RS model the probability of a complication after irradiation of a relative volume v_i at a dose D_i is given by:

$$NTCP_{RS} = \left\{1 - \prod_i [1 - P(D_i)^s]^{v_i}\right\}^{1/s} \tag{1.12}$$

$$P(D_i) = 2^{-exp\left[e\gamma s\left(1-\frac{D_i}{D_{50}}\right)\right]} \tag{1.13}$$

where $P(D_i)$ is the probability of complication due to the irradiation of the relative volume v_i at the dose D_i described by an approximation of Poisson statistics.
The model contains three parameters (D_{50}, v, s), D_{50} has the same meaning as for the LKB model, γ is a slope parameter which affects the steepness of the sigmoid shape dose-response curve, and s assumes values in the range 0 - 1, large values of s indicate a serial structure while small values indicate a parallel structure.

The typical sigmoidal relationship between dose and response endpoint supports use of a logistic regression model:

$$NTCP_{logistic} = \frac{1}{1 + e^{-g(x)}} \tag{1.14}$$

with

$$g(x) = \beta_0 + \beta_1 x_1 + \beta_2 x_2 + \cdots + \beta_n x_n \tag{1.15}$$

where $x_1, x_2 \ldots x_n$ represent different input variables and $\beta_0, \beta_1, \ldots \beta_n$ are the corresponding regression coefficients determined by maximizing the probability that the data gave rise to the observations.

The power of the NTCP logistic model is the possibility of including clinical patient-specific factors along with dosimetric parameters of the OARs involved in a radiation treatment. Multivariable approach potentially can points out physiological interaction of several organs and their contributions in affecting specific organ's functions.

CHAPTER 2

Radiation effects on optical fiber

This chapter focuses on the interaction of ionizing radiation with optical fiber which leads to a variety of physical processes that principally can be used for radiation detection and measurement of the radiation dose. We describe the model of energy deposition that, thought radiation damage processes, gives rise to defect points.

In this framework the most widely investigated models of explanation of the fiber photosensitivity are presented. In addition the fiber Bragg grating principle for temperature, strain and dose sensing is illustrated.

2.1 Photosensitivity of optical fiber

When optical fibers are subjected to radiation, whether it consists of high energy light, X-rays, γ-rays, neutrons or high energy cosmic particles, their optical properties change due to the interaction of the radiation in the fiber core and in the cladding material. The main effects result from electronic processes: electrons are excited to leave their normal (bound) position, changing the physical and chemical properties of silica glass. The property of a medium to have its refractive index permanently changed by a modification of its physical or chemical properties through UV light exposure is known as photosensitivity.

Photosensitivity was first observed in germanium-doped silica fiber by Hill and co-workers in 1978 at the communication Research Centre in Canada [10, 40]. They described a permanent grating written in the core of the fibers by the argon ion laser line at 488 nm launched into the fiber. This particular grating had a very weak index modulation, which was estimated to be of the order of 1026 resulting in a narrow-band reflection filter at the writing wavelength. Photosensitivity in optical fibers remained dormant for several years after its discovery by Hill et al.

[41] mainly due to limitations of the writing technique. However, a renewed interest has risen with the demonstration of the side writing technique by Meltz et al. almost ten years later [42].

Progress in optical fiber photosensitivity research developed rapidly after the discovery of the possibility to write a periodic variation of the optical refractive index into the core of the optical, named Fiber Bragg Grating (FBG), illuminating the core from the fiber's side with the interference pattern of two beams of coherent UV radiation. At now optical fiber sensors have been successfully used for temperature, strain, pressure and acceleration monitoring.

The reflection wavelength of the FBG (Bragg wavelength) depends on the grating characteristics (period, modulation) and is influenced by the ambient conditions such as strain and temperature. The parameters influencing the optical fiber's response to ionizing radiation include:

- fiber composition and fabrication method;
- type of radiation, dose-rate, total dose;
- optical wavelength and power;
- temperature;
- thermal treatment and irradiation history;
- time elapsed between exposure and measurement

2.2 Point defects in optical fiber

Amorphous silica is the principal building material for glassy fiber waveguides. The SiO_2 network is built with SiO_4 tetrahedra joined at the corners so that each Si-atom is bound to four O - atoms and each O atom is the bridge between two Si-atoms. The angles defining the relative spatial orientation of each pair of connected tetrahedra are statistically distributed between 120° and 180°, according to Continuous Random Network (CRN) models , the first of which was introduced by Zachariasen in 1932 [43].

An illustrative picture of an amorphous silicon dioxide network is shown in Figure 2.1. Due to the high Si-O bond energy (4.5 eV), the crystalline quartz is resistant to chemical weathering and to corrosion.

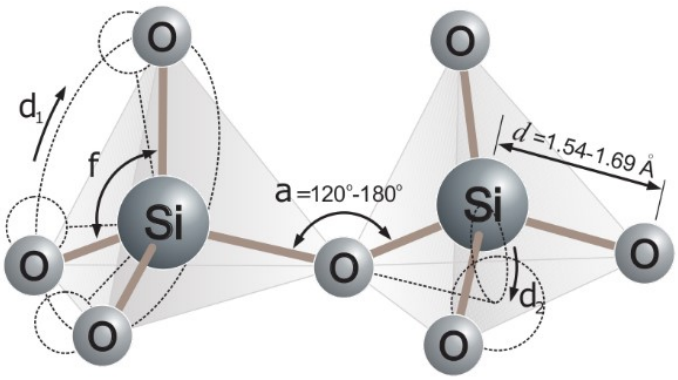

Figure 2.1. Three-dimensional schematic of a pure fragment of the regular silica structure. The structure is defined by several parameters; the Si-O bond length (d), the tetrahedral angle (φ), the inter-tetrahedral bond angle (α), and the bond torsion angles (δ_1, δ_2) [44].

The interaction of the radiation with the fiber material is a complex process with quite a number of dependencies on parameters related to the fiber fabrication process, operating environment and radiation type. Irradiation, mechanical stress, change of temperature, and the presence of impurities may cause the formation of defects and/or lead to the transformation of the existing defects to other types of defect.

The presence of defects in the silica matrix can dramatically change its structural, electrical, and optical properties. Defects can be distinguished in intrinsic, when they are due to a variation of the basic silica elements (silicon or oxygen) and extrinsic, if they are related to presence of impurities in the silica matrix (H, Ge, P, etc.). Extrinsic defects due to the presence of impurities (Cl, H and so on) are always present in variable concentration in the material. Many aspects regarding the nature of the defects and their correlated properties are still controversial and not yet completely understood. Quite a lot of defect types have been discussed in the literature and many reproduction models have been proposed for each one according to extensive experimental and theoretical studies [45, 46].

To provide a background for the experimental study, the following section of the chapter is devoted to review the current understanding of the main defects in the silica network.

2.2.1 Intrinsic point-defects

The *silicon dangling bond*, or *E' center*, is the most widely investigated oxygen deficient defect. It consists of a silicon atom with six electron in three pairs and one unpaired electron, generally denoted by the symbol ≡ Si•: the symbol (≡) represents three bonds to oxygen atoms, (•) represents one unpaired electron (Figure 2.2). E' defect was observed for the first time in the 1956 by R. A. Weeks using electron paramagnetic resonance (EPR) spectroscopy [47, 48]. The formation efficiency of E' defects strongly depends both on the content of the hydroxyl radicals (OH) in the glass and on the irradiation energy. It was shown by Hanafusa [49] and Hibino [50] that E' defects also exist in non-irradiated optical fibers.

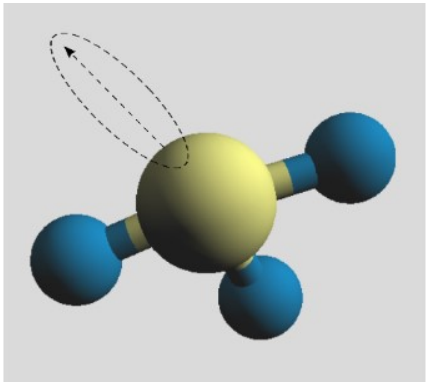

Figure 2.2. Generic E' center. The yellow atom is silicon, the blue ones are oxygens.

The *oxygen deficient centers* (ODC) are formed when an oxygen is missing or removed from its Si-bonding position. The literature describes two models for the ODCs: neutral oxygen vacancy ODC(I) indicated as ≡ Si-Si ≡ and the twofold coordinated silicon ODC(II) denotes as = Si••. The ODC(I) gives rise to strong optical absorption bands around 7.6 eV while ODC(II) shows a relatively weak absorption band with peak at 5.03 eV. The ODC (I) represents one of the essential defects in all silicon dioxide modifications in a form of simple oxygen vacancies; here two Si atoms could relax and make a silicon bonding (relaxed oxygen vacancy ≡ Si-Si ≡) or stay in unstable interaction condition and form an unrelaxed oxygen vacancy (≡ Si···Si ≡) which each one of them could be a precursor for the other, (see Figure 2.3, and both are considered as a key role in many defect-type generations and transformations in the silica matrix.

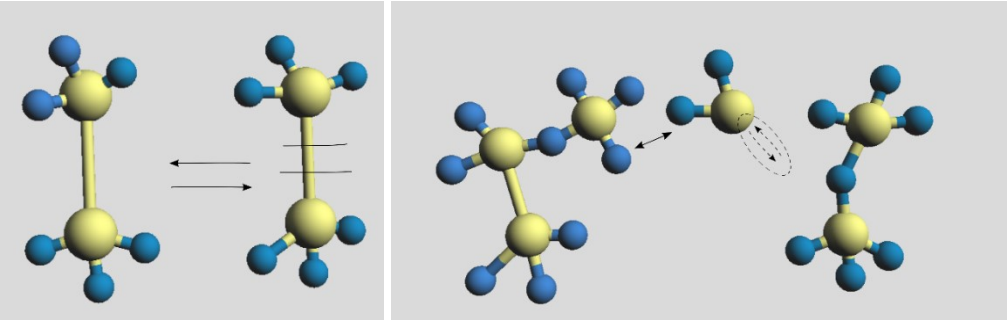

Figure 2.3. Schematic illustration of the transformation between ODC(I) and ODC(II) visualizing two possible models for the ODC(II), the unrelaxed oxygen vacancy and the twofold coordinated silicon. The yellow atom is silicon, the blue ones are oxygens.

The *oxygen dangling bond* or *Non Bridging Oxygen Hole Center* (NBOHC) can be visualized as the oxygen part of a broken bond and it is denotes as ≡ Si-O• (Figure 2.4). The intense absorption bands at 4.8 and 6.8 eV, make NBOHC the defect that more influences the transmission of silica in the ultraviolet and vacuum-ultraviolet spectral ranges. It has been postulated that the NBOHC arises when hydrogen atoms are liberated radiolytically from one member of a pair of OH groups in wet silica (high OH group) [51].

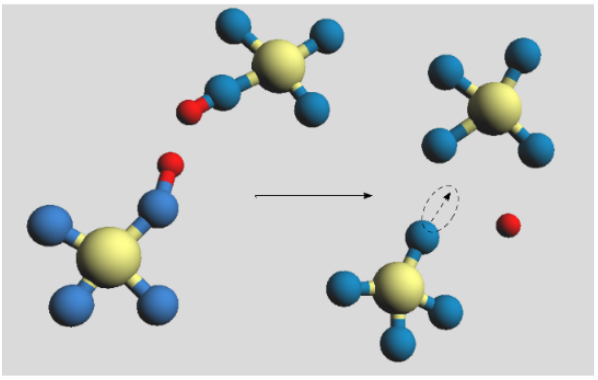

Figure 2.4. A model of atomic structure of the non-bridging oxygen hole center (NBOHC) showing the possible generating processes of NBOHC in wet silica. The yellow atom is silicon, the blue ones are oxygens, and the red ones are hydrogens.

Peroxy bridge (POL) is a "wrong" oxygen-oxygen bonds denoted as ≡ Si-O-O ≡ Si. The experimental evidence of this defect is only indirect but calculation put the energy absorption band at around 6.4 - 6.8 eV. POL was initially suggested to be the main precursor of the *Peroxy radical* (POR) defects, a silicon atom linked to an oxygen molecule denoted as ≡ Si-O-O• (see Figure 2.5) [52].

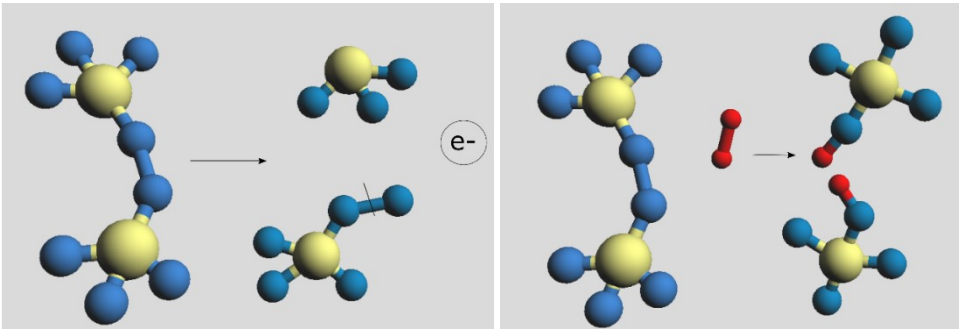

Figure 2.5. Models presenting the suggested atomic structure of a peroxy bridge (POL) and its role in producing peroxy radical (POR) structure in silica matrix. The yellow atom is silicon, the blue ones are oxygens, and the red ones are hydrogens.

Other oxygen excess related defects are the *interstitial oxygen molecule* and the *interstitial ozone molecules* (Figure 2.6).

Finally, the self-trapped hole (STH) may be the first defect to form under the influence of ionizing radiations. Its principal characteristic is the capture of a hole on a 2p orbital from a doubly linked oxygen atom [53].

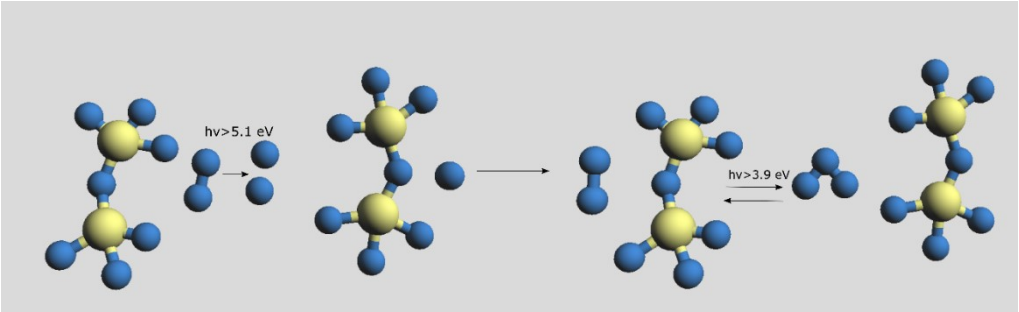

Figure 2.6. Main interstitial atomic and molecular oxygen as well as ozone model in SiO_2. The yellow atom is silicon, the blue ones are oxygens.

2.2.2 Extrinsic point-defects

Among the impurities present in silica fibers, hydrogen, germanium (Ge), phoshore (P) and fluorine (F) are the most diffuse. Ge, P and F are very important dopants in fiber technologies. Since Ge and Si are isoelectronic elements, it is qualitatively expected that many Ge-related point defects are structurally identical to Si-related centers apart from the substitution of Si with Ge [54].

Starting from the comparison between a Ge-doped silica glass and a pure silica glass, it possible to show that defects related to germanium are predominant on the intrinsic ones [55]. This property implies an UV absorption from two to three

order of magnitude more intense in germanosilicate glasses, even before irradiation exposure [56], as compared to pure silica. The scientific interest for germanosilicate glass increased even more after experimental discovery of the property of photosensitivity of this material.

The most common extrinsic defects in Ge-doped silica are the GeE' center and the Germanium Electron Centers (GECs) in the structural model of Ge(1) or Ge(2). The microscopic structure of GeE' defect is denoted as ≡ Ge•. It's structurally identical to the E' center apart from substitution of Si with Ge and show an absorption band at 6.2 eV - 6.4 eV. Germanium Electron Center Ge(1), denoted as ≡ GeO_4•, and Ge(2) denoted as = Ge•, are electron traps, constituted by an electron trapped on a tetracoordinated Ge atom with a Si or Ge atom in the adjacent tetrahedron, respectively. An absorption band at 4.4 eV - 4.6 eV has been attributed to Ge(1) center and an absorption band at 5.8 eV was assigned to Ge(2) center [55, 57, 58].

Finally there are the Oxygen-Deficiency Center (GeODC(II)) in the structural model of the two fold coordinated Ge or Germanium Lone Pair Center (GLPC), that is a dicoordinate germanium atom with a lone pairs denoted as = Ge•• and in the structural model of the neutral oxygen vacancy (NOV) denoted as ≡ Ge···Si. Several studies have shown that a contribution to the photosensitivity is due to the variation of the UV optical absorption spectra associated with the GLPC [59-61]. This defect is characterized by an absorption band at 5.1 eV [60]. The reader is referred to [44, 62, 63] for a more comprehensive review of both the nature and the molecular structure of radiation-induced point defects in pure and doped glassy silica.

2.3 Interaction of the radiation with matter

The energy of photon considered in medical application is in the range of nominal energy 6 - 20 MeV. Compton scattering is the main interactions process for low - and medium - Z elements in a certain energy range, typically between 0.05 and 5 MeV. Therefore considering the nature of the optical materials involved for optical fibers and FBG (typically low atomic numbers such as Si, O, Ge) the main interaction for these photons occurs thought Compton scattering: the incoming photon ejects an electron from an atom and a photon of lower energy is scattered from the atom. Since electrons are charged they can also yield immediate ionization through elastic or inelastic scattering processes. A material exposed to

energetic radiation thus experiences a cascade of effects leading to modifications of the electronic and atomic structure. The photon interaction with the matter depends on the incoming photon energy and the atomic number Z of the shielding material.

In radiotherapy, the quantity of interest is the dose to water (or to tissue). As no dosimeter is water or exactly tissue equivalent for all radiation beam qualities, the energy dependence is an important characteristic of a dosimetry system, so it requires energy correction within the quality range of therapeutic beams in use.

The beam penetration range in a material is often characterized by the water equivalent thickness, which measures the thickness of liquid water needed to stop the ion beam in the same manner that a certain thickness of the given material. A proper evaluation of the water equivalent properties of materials has to take into account the main effects in the energy deposition of the beam. Therefore, for a precise comparison of the materials and liquid water measurements, the water equivalent thickness of the materials must be accurately determined.

The intensity I(x) of a narrow monoenergetic photon beam, attenuated by a target material of thickness (x) is given as:

$$I(x) = I_0 \exp[-\mu_m(h\nu, Z)\, \rho x] \tag{2.1}$$

where I_0 is the original intensity of the unattenuated beam and ρ is the density of the target material of thickness (x). Similarly $\mu_m(h\nu, Z)$ is the mass attenuation coefficient, which depends on the photon energy $h\nu$ and atomic number (Z) of the target material. More precisely the probability for a photon to undergo any type of interaction with an attenuator depends the Z_{eff} of the attenuating material.

In general, the photoelectric effect predominates at low photon energies, the Compton effect at intermediate energies, and the pair production at high photon energies.

The total mass attenuation coefficient μ_m is given as a sum of mass attenuation coefficients for the individual photon interactions:

$$\frac{\mu}{\rho} = \frac{\mu_{PE}}{\rho} + \frac{\mu_R}{\rho} + \frac{\mu_C}{\rho} + \frac{\mu_{PP}}{\rho} \tag{2.2}$$

Figure 2.7 and Figure 2.8 show the regions of relative predominance of the three most important individual effects with $h\nu$ and Z_{eff} as parameters [64].

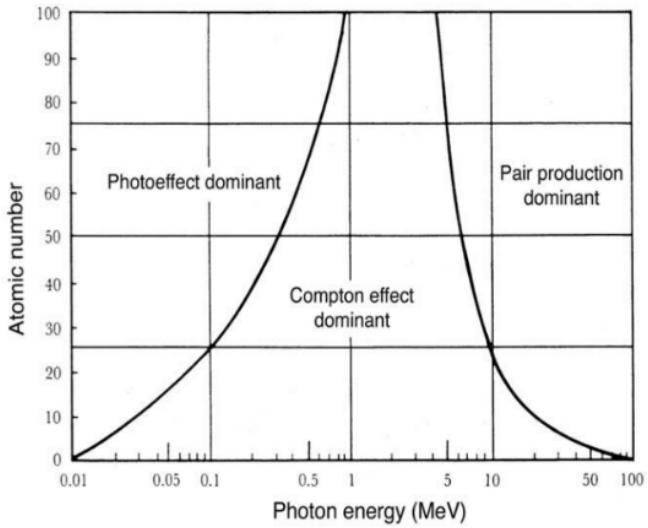

Figure 2.7. The diagram presents the regions of relative predominance of the three main forms of the photon interaction with matters. Border lines indicate the transition of absorption coefficients of the material at different energy regions [64].

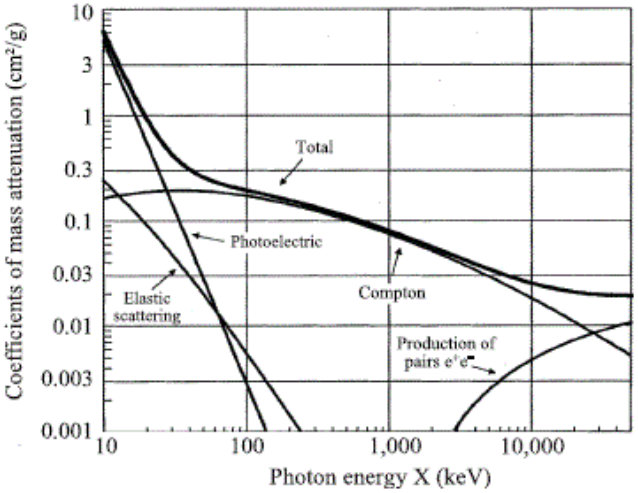

Figure 2.8. Dependence of the mass attenuation coefficients, $\mu_m(h\nu, Z)$ of the water equivalent soft tissue ($Z_{eff} = 7$) on the energy of the incident photons [64].

Several works have been carried out on the mass attenuation coefficients, effective atomic number and effective electron density for different types of material of dosimetric interest [65-67].

2.4 Radiation damage process: dose calculation as function of interaction parameters

It is possible to distinguish two classes of radiation damage processes, the knock-on and the radiolysis [68, 69].

In the knock-on processes the projectile particles of the incident beam interact directly with the atoms of the material causing displacements (for example, vacancy-interstitial Frenkel pair) or site distortions. Two kinds of knock-on processes are generally considered: the elastic, that conserves the total kinetic energy, and the inelastic, in which some of the projectile kinetic energy is lost in electronic transitions (excitation, ionization) or nuclear reactions [69]. In order to create defects by displacements, it is necessary that the projectile gives sufficient energy to the target atom to break its bonds and to prevent that the knocked-on atom is recaptured from its neighboring atoms. The value of this energy for a given atom in the matrix is called displacement energy T_d, and it has been estimated that, in SiO_2, $T_d^O \sim 10$ eV and $T_d^{Si} \sim 20$ eV, for O and Si displacements, respectively, assuming a Si-O bond energy of ~ 5 eV [70, 71].

In radiolytic processes the irradiation primarily changes the state of an electron but no stable ionic or atomic defects are initially formed [68, 69]. The energy absorbed appears in the form of electrons in a normally empty conduction band and holes in the normally occupied valence bands, or in the form of excitons (electron-hole pairs bound to each other) at some site of the material. These excitations could be considered as a first step and are followed by other processes that lead to stable electronic states. A significant fraction of these electron-hole pairs recombine radiatively or are separately trapped on impurities, on pre-existing defects or on radiation-induced defects, or are absorbed in non-radiative processes involving phonons. Finally, if the electron-hole pair recombines non-radiatively and its energy is focused on an atom it may be converted into kinetic energy of the latter (as for example an ion repelled by electrostatic forces), resulting in bond ruptures or in the creation of vacancy-interstitial pairs.

The effects of the irradiation are quantified by the energy deposited in the material. To determine this energy it is useful to start introducing the scattering differential cross section $\sigma_E(\theta, T)$. Independently from the collision event (knock-on, radiolisys), $\sigma_E(\theta, T)$ is the probability density that a projectile particle, with incident energy E, transfers an energy from T to $T + dT$ to the target and is deflected of an angle in the range from $\theta + d\theta$, with respect to its incident direction

[68]. From the differential cross section it is possible to derive the energy transferred to the target per unit length $\left(-\frac{dE}{dx}\right)$. Considering that during a collision a projectile can transfer energy T, the average energy transfer over a range δ_r in the target material is

$$\langle T \rangle = N\,\delta_r \int_0^{\pi} \int_{T_{min}}^{T_{max}} T\,\sigma_E(\theta, T) d\theta\, dT \tag{2.3}$$

where N is the number of scattering centers per unit volume, T_{max} and T_{min} are the maximum and the minimum energy transferred, respectively, and δ_r is small enough to account for a single collision.

Therefore the average energy loss $\langle \Delta E_1 \rangle$ of a projectile over a range δ_r equals - $\langle T \rangle$, and the energy transferred to the target per unit length (*stopping power*) is:

$$\left(-\frac{dE}{dx}\right) = \frac{\langle \Delta E_1 \rangle}{\delta_r} = N \int_0^{\pi} \int_{T_{min}}^{T_{max}} T\,\sigma_E(\theta, T) d\theta\, dT \tag{2.4}$$

The deposited energy, that is the absorbed dose, in a target of thickness x, is given by

$$D = \frac{\phi\,\Delta t}{x} \int_0^x \left|\frac{dE}{dx}\right| dx \tag{2.5}$$

where $\phi\,\Delta t$ is the fluence of projectile particles (particles per unit area).

In the presence of composite targets, like SiO_2, the energy loss is determined, in first approximation, as the sum of the energy losses of each constituent (Si and O) weighted by their mass fractions (0.47 and 0.53 for Si and O, respectively). In general it is worth to note that not all the deposited energy gives rise to point defects as a great quantity is loosed in radiative and non-radiative processes.

2.5 Fiber Bragg gratings

Since the discovery of photosensitivity in optical fibers there has been great interest in the fabrication of Bragg gratings within the core of a fiber. A FBG is a

periodic modulation of the refractive index along the fiber length which is formed by the exposure of the core to an intense optical interference pattern. The ability to inscribe intracore Bragg gratings in these photosensitive fibers has revolutionized the field of telecommunications and optical fiber based sensor technology. Over the last few years, the number of researchers investigating fundamental, as well as application aspects of these gratings has increased dramatically [72]. The core region has a higher refractive index than the surrounding cladding material, which is usually made of silica. Light is therefore trapped in the core by total internal reflection at the core-cladding boundaries and is able to travel tens of kilometers with little attenuation in the 1550 nm wavelength region. The Ge doping of silica is widely used to realize different optical devices [73-76] and one of the most important consequences of Ge doping is the variation of the refractive index of the material [77], a property used to realize optical fiber for telecommunication. The doping of the core with Ge increases the refractive index of this part with respect to that of the cladding allowing the light to be banded inside the core region [78].

However the most important effects of the Ge doping, which have attracted the researcher attention on the GeO_2-SiO_2 are its photosensitivity. Changing the elemental composition of the glass can significantly alter the radiation sensitivity of an optical fiber. Pure SiO_2-core fiber have the lowest radiation sensitivity and represent the best choice of fiber for transmitting optical information in high-radiation environments. Several authors have investigated the possibility to use doped optical fiber sensors in nuclear environments for high dose levels measurements and for dose verification in clinical radiotherapy with the photon [79-83] as well as with the electron and the proton beams [82, 84, 85]. Much of these works presented the potential use of fiber optic as plastic scintillation dosimeters and very few as FBG based dosimeters [83, 85, 86]. FBG sensors are largely employed in civil engineering as strain and/or temperature sensors, for remote structural monitoring [87-90]. The physical principle of FBG sensor is based on the property to reflect a specific frequency of light while transmitting all others according to the following equation:

$$\lambda_B = 2\, n\, \Lambda \tag{2.6}$$

λ_B is the Bragg wavelength, n is the effective refractive index of the fiber core, and Λ is the spacing between the gratings, known as the grating period.

In Figure 2.9 is illustrated the principle of the fiber Bragg grating sensor: when a broad-spectrum light beam is sent to an FBG, reflections from each segment of alternating refractive index interfere constructively only for the Bragg wavelength.

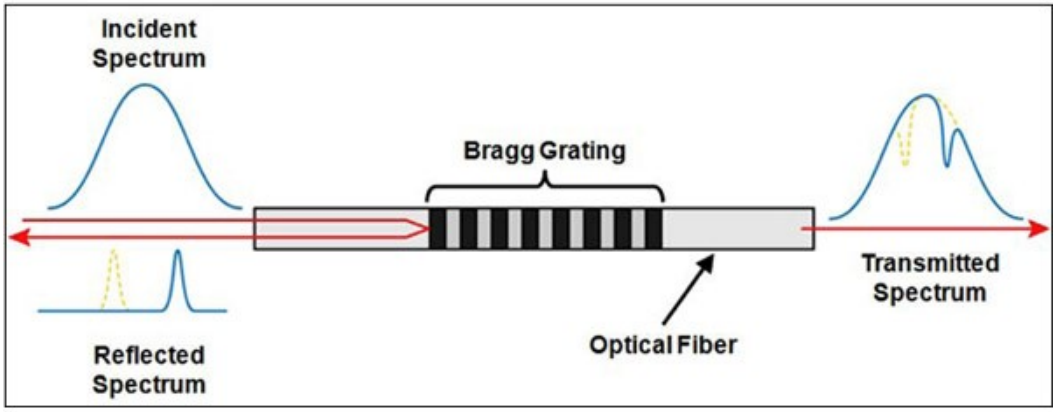

Figure 2.9. Illustration of the physical principle of a uniform Bragg grating.

2.5.1 Fiber Bragg grating strain- and temperature-sensor

Fiber optical sensor technology for strain and temperature measurements has increasingly come into focus over the past decade. FBG sensors can measure very high strain (> 1000 μm/m) and are therefore very well suited to highly stressed composite constructions. On the other hand FBG temperature sensors offers a high sensitivity, as well as other important advantages, such as real-time processing, long term stability, electromagnetic interference immunity, and multiplexing capability.

The Bragg grating resonance, which is the center wavelength of light back reflected from a Bragg grating depends on the effective index of refraction of the core and the periodicity of the grating (Eq. (2.6)).

By partially differentiating the two variables that are independent of each other we obtain, for small variations, according to the total differential:

$$\Delta\lambda_B = 2\left[\Lambda\frac{n}{\partial l} + n\frac{\partial\Lambda}{\partial l}\right]\Delta l + 2\left[\Lambda\frac{\partial n}{\partial T} + n\frac{\partial\Lambda}{\partial T}\right]\Delta T \qquad (2.7)$$

The first term in Eq. (2.7) represents the strain effect on an optical fiber. This corresponds to a change in the grating spacing and the strain-optic induced change in the refractive index.

The above strain effect term may be expressed as:

$$\frac{\Delta\lambda_B}{\lambda_B} = (1 - p_e)\epsilon_z \tag{2.8}$$

where p_e is an effective strain-optic constant defined as:

$$p_e = \frac{n^2}{2}\left[p_{12} - \nu(p_{11} - p_{12})\right] \tag{2.9}$$

where p_{11} and p_{12} are components of the strain-optic tensor, n is the index of the core, and ν is the Poisson's ratio. For a typical optical fiber $p_{11} = 0.113$, $p_{12} = 0.252$, $\nu = 0.16$ and $n = 1.482$. Using these parameters and the above equations, the expected sensitivity at ~ 1550 nm is a 1.2 pm change as a result of applying 1 $\mu\epsilon$ to the Bragg grating.

The second term in Eq. (2.7) represents the temperature effect on an optical fiber. A shift in the Bragg wavelength due to thermal expansion changes the grating spacing and change the index of refraction. This fractional wavelength shift for a temperature change ΔT may be written as [72]:

$$\Delta\lambda_B = \lambda_B\,(\alpha_\Lambda + \alpha_n)\,\Delta T \tag{2.10}$$

where $\alpha_\Lambda = \left(\frac{1}{\Lambda}\right)\left(\frac{\partial\Lambda}{\partial T}\right)$ is the thermal expansion coefficient for the fiber (approximately, 0.55 x 10^{-6} for silica). The quantity $\alpha_{\mathrm{n}} = \left(\frac{1}{\mathrm{n}}\right)\left(\frac{\partial \mathrm{n}}{\partial T}\right)$ represents the thermo-optic coefficient and it is approximately equal to 8.6 x 10^{-6} for the germanium-doped silica-core fiber. Clearly, the index change is by far the dominant effect. From Eq. (2.10), the expected sensitivity at a ~ 1550 nm Bragg grating is approximately 13.7 pm/°C.

2.5.2 Fiber Bragg grating dose-sensor

Radiation-induced Bragg wavelength shift due to refractive index change. Several authors have investigated the effects of radiation on an optical fiber sensor to exploit the possible use as temperature and/or radiation sensors [86, 91]. Analogously to changes of the grating pitch by mechanical action, energy transfer

from the ionizing radiation to the fiber modifies the index value and thus translates into a Bragg wavelength shift.

The immunity to electromagnetic interference, intrinsic safety, mechanical simplicity and small size as well as the possibly high sensitivity and multiplexing capabilities make FBG sensors a real alternative for standard nuclear instrumentation. Quite recently, a first evidence of optical-wavelength-shift sensing of gamma rays by fiber Bragg-grating has been reported in the literature only for *non-clinical* dose levels (100 kGy) [86]. Krebber et al. observed a continuous increase of $\Delta\lambda_B$ with the radiation dose at high dose levels without saturation up to 100 KGy for all FBGs investigated [86]. In this thesis the response of dosimeters based on FBG technology in the energy and dose levels of clinical interest was investigated.

The radiation dose (D) dependence of λ_B can be derived from Eq. (2.6) as follows:

$$\frac{1}{\lambda_B}\frac{d\lambda_B}{dD} = \frac{1}{n}\frac{\partial n}{\partial D} + \frac{1}{\Lambda}\frac{\partial \Lambda}{\partial \mathrm{D}} \tag{2.11}$$

The first term gives the radiation-induced refractive index change, Δn, the second term denotes the change of the grating period with the dose, i.e. the coefficient of the radiation-induced linear expansion of the fiber. This coefficient is quite small for SiO_2 (1×10^{-7} Gy^{-1}) [92] and could be neglected.

Therefore the Eq. (2.11) can be approximatively transformed into

$$\frac{\Delta\lambda_B}{\lambda_B} = \frac{\Delta n}{n} \tag{2.12}$$

Using this relation and the refractive index values for the respective wavelengths, one can calculate the radiation-induced change of the refractive index.

2.6 Mechanism of photoinduced refractive index change

Bragg gratings have been written in many types of optical fibers using various methods, however, the mechanism of index change is not fully understood. Several models have been proposed for the photoinduced refractive-index change. The

only common elements in these theories is that the germanium-oxygen vacancy defects, Ge-Si or Ge-Ge (the so-called "*wrong bonds*") are responsible for the photo-induced index changes.

In 1989, Meltz *et al.* [42] showed that a strong index of refraction change occurred when a germanium-doped fiber as exposed to UV light close to the absorption peak of a Germania-related defect at a wavelength range of 240 - 250 nm. The fact that the change of the index of refraction in a germanosilicate optical fiber is triggered by a single photon at ~ 240 nm, which is well below the band gap at 146 nm, implies that the point defects in the ideal glass tetrahedral network are responsible for this process. Defects in optical fibers first attracted attention because of the unwanted absorption band associated with them, which caused transmission losses. Normally the defects are caused by the fiber drawing process, and ionizing radiation as described in the previous paragraphs.

The radiation induced defect centers were identified and characterized by electron spin resonance spectroscopy. The creation of defect bands are centered at 195, 213, and 281 nm. The photosensitivity phenomenon, which is a basis for the fabrication of fiber gratings, is commonly ascribed to two essential physical mechanisms: creation of *color centers* and *structural transformations*. Both effects are well established. However, there is no general agreement about which mechanism dominates in the case of Ge-doped silica fibers.

The analysis of the color-center contribution assumes a rather straightforward application of the Kramers–Kronig relations. The model, known as "*color center model"*, proposed the breaking of the GeO defect resulting in a GeE' center with the release of an electron, which is free to move within the glass matrix until it is retrapped.

The Kramers-kronig relationship is given as:

$$\epsilon_r(\lambda) = 1 + \int \frac{\epsilon_i(\lambda)}{\lambda' - \lambda}\, d\lambda' \tag{2.13}$$

Relates the real and imaginary parts of the dielectric constant $\epsilon = \epsilon_p + i\epsilon_1 = (n + ik)^2$ where n is the refractive index and k is the absorption index.

The relationship arises from the causality condition for the dielectric response and demonstrates that the index change produced in the infrared/visible region of

the spectrum by the photoinduced processing results from a change in the absorption spectrum of the glass in the UV/far-UV spectral region.
The Eq. (2.13) can be explicated as follow:

$$\Delta n(\lambda) = \frac{1}{2\pi^2} + \int_0^{\infty} \frac{\Delta\alpha\ (\lambda)}{1 - (\lambda/\lambda')^2}\ d\lambda \tag{2.14}$$

$\Delta\alpha$ is an increase of attenuation, Δn is the change of the refractive index, λ is the wavelength for which the refractive index is calculated and λ' is the centre wavelength of an absorption band.

Since the radiation-induced attenuation strongly depends on the wavelength of the transmitted light, with a minimum at about 1100 nm, a moderate increase towards the far infrared and a strong increase towards shorter wavelengths [93], the choice of the FBG with a specific sensitivity is recommended according to the application. In this model, UV exposure changes the material properties of the glass and introduces new electronic transitions of defects (*color centers*). The underlying premise of the color center model is that the photosensitive effect arises from localized electronic excitations of defects. The wrong-bond defects, which initially absorb the light, are transformed to defects that are more polarized by virtue of the fact that their electronic transitions occur at longer wavelengths or have stronger transitions. According to the color center model, the refractive index at a point is related only to the number density and orientation of defects in that region and is determined by their electronic absorption spectra.

A structural rearrangement of the atoms of the silica matrix is the base of the predicting model known as "*compaction effects*" [91, 94, 95]. It is well known that radiation exposure of vitreous silica can cause changes in the physical properties such as density [93]. The detailed origin of this density change has never been quite clear, but the compaction effect has been so universally observed in vitreous silica that it appears to be an inherent property of the material.

The theoretical basis of the relationship between reflective index and mass density is embedded in the Lorentz–Lorenz, which relates macroscopic optical/electrical properties (dielectric constant and refractive index) to the corresponding microscopic molecular properties (e.g., molecular polarizability).

Lorentz–Lorenz relation for the refractive index (n) is the following [96]:

$$\frac{(n^2-1)}{(n^2+2)} = \frac{\alpha\rho}{3} \tag{2.15}$$

where ρ is the number density of the material molecules, α is the mean molecular polarizability.

In terms of the mass density ρ_m, which is related to the number density by $\rho_m = (M/N_A)\,\rho$, the Lorentz–Lorenz relation becomes

$$\frac{(n^2-1)}{(n^2+2)\,\rho_m} = \frac{N_A\,\alpha}{3\,M} \tag{2.16}$$

where N_A is the universal Avogadro's number and M is the molecular weight of the chemical element of the material.

In general, the dose dependence of compaction in vitreous silica obeys a power law [94]:

$$\frac{\Delta\rho_m}{\rho_m} = A' D^c \tag{2.17}$$

where D is the absorbed radiation dose, A' and c are constants. The dose exponent c is found to be dependent on the nature of the radiation source and the effect of radiation on silica. For example, c is close to 1 for knock-on (atomic displacement) radiation (neutron, He^+, or D^+, etc.) [97] and is about 272 for ionizing radiation (γ-ray [97-99]), e-beam [97, 100] and ultraviolet (UV) radiation [101-103].

The phenomenon of compaction of silica after irradiation suggest a bond rearrangement leading to a decrease in the volume of the system and a refractive index variation accordingly, results both from trivial organizational events and from bond rupture followed by re-formation of bonds. To explain the photoinduced changes in glass network structure further interesting theories have been proposed, but none of them provide a structural interpretation that is consistent across glass families and explains the wide range of photoinduced property variations because of the complex dynamic of the phenomenon. The models are discussed in depth in the review article [72].

CHAPTER 3

Materials and methods

The purpose of the present chapter is to give a detailed description of the instruments and methods for the experiments and the data processes performed.

For a better readability, the chapter has been divided into two sections: the first dedicated to the TLDs and optical fiber sensors, the second devoted to the statistical method to perform optimization of NTCP models.

Part I

TLDs and FBGs characterization

3.1 Linear accelerators

The irradiation experiments were performed using the linear accelerators installed at the University of Naples Federico II.

The Siemens Primus accelerator provides a 6 MV photon beam and the NOVAC7 accelerator provides four levels of nominal energy: 3, 5, 7 and 9 MeV[1] electron beams. Below are presented an overview of the equipment of the accelerators and a description of the dosimetric aspects.

[1] Conventionally, the energy of diagnostic and therapeutic gamma-and X-rays is expressed in kilovolts or megavolts (kV or MV), whilst the energy of therapeutic electrons is expressed in terms of megaelectronvolts (MeV). In the first case the energy value is numerically equal to the voltage used by a linear accelerator to produce the photon beam.

3.1.1 Primus Siemens accelerator

The *Primus Mid Energy* (Siemens, Germany) accelerator is installed at the Radiation Oncology Department (Figure 3.1). This accelerator can delivered photon beams with nominal energy of 6MV, operating with a dose rate of 2 Gy/minute for a field size of 10 x 10 cm[2] and a dose-per-pulse rate in the range of 0.15 mGy/pulse.

Two ionization chambers are installed in the beam axis to monitor the radiation. The unit of their signal is the monitor unit (MU). The usual definition is that 100 MU comply to the dose of 1 Gy in the dose maximum in water with a source-surface-distance (SSD) of 100 cm.

The accelerator is equipped with a magnetron which provides the high power radiofrequency wave, necessary to accelerate the electrons in the waveguide. The photon beam is collimated by focusing so-called Y-jaws and a focusing multileaf collimator (MLC) made of tungsten to create an individual field geometry. The MLC is constituted of two block of tungsten each of 29 leaves. The dimension of the projection of each leaf of the 27 central leaves is of 1 cm at the isocenter, while the dimension of the two external leaves is 6.5 cm.

Figure 3.1. Primus Mid Energy; Siemens.

The energy spectrum (Figure 3.2) of the photons emitted by the accelerator presents an average energy of 1.6 MeV[2].

[2] In medical linear accelerators, electrons, boiled out of a cathode, strikes a target of a high Z material such as tungsten. The electron energy is converted into a spectrum of X-ray energies with maximum energy equal to the incident electron energy. The average photon energy of the beam is approximately one-third of the maximum energy.

It's interesting to note that the knowledge of the spectra is useful for accurate three-dimensional treatment planning but also in other applications, including the design of filters and beam modifying devices and determination of factors to convert ionization chamber measurements to dose.

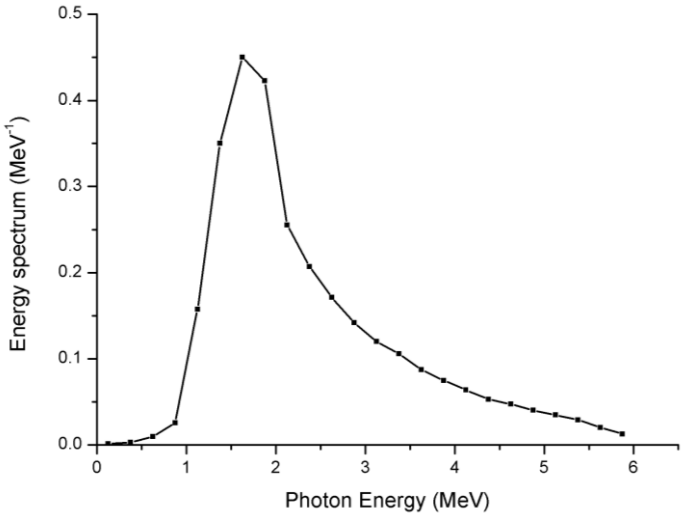

Figure 3.2. Energetic spectrum of Siemens PRIMUS linear accelerator. The values on vertical axis are the number of photons per unit of energy. The maximum energy is 6 MeV, the average energy with which photons are emitted is 1.6 MeV.

An important dosimetric characteristic of clinical photon beams is the *Percentage Depth Dose profile* (PDD) that represents volumetric and planar variations in absorbed dose. It relates the 'absorbed dose' deposited by a radiation beam into a medium as it varies with depth along the axis of the beam. The dose values are divided by the maximum dose, yielding a plot in terms of percentage of the maximum dose. In Table 3.1 are reported the depth dose values measured on central beam axis.

The PDD curve in Figure 3.3 shows the maximum at the depth of 2 cm and it is characterized by an entrance dose value of about the 40% of the maximum while at the depth of 16 cm dose value reached the 50% of the maximum value.

Table 3.1. Dose level depth of Primus Mid Energy photon beam.

Energy	Depth 100% isodose (cm)	Depth 90% isodose (cm)	Depth 80% isodose (cm)	Depth 10% isodose (cm)
6 MV	2	5	8	30

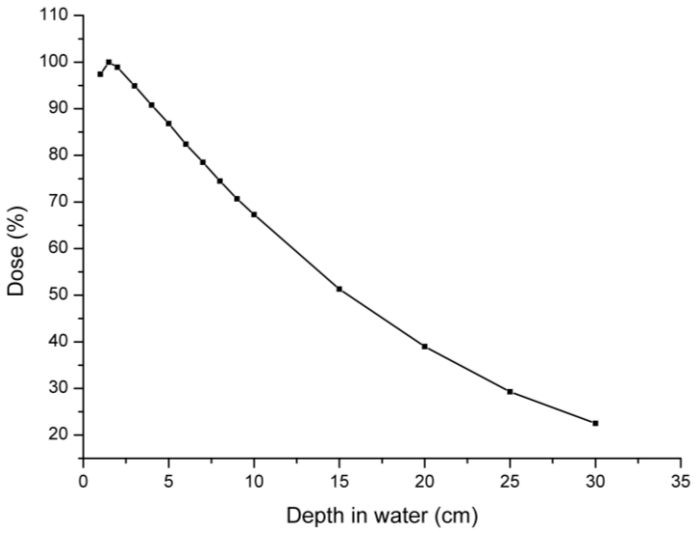

Figure 3.3. PDD curve in water for a 10 × 10 cm² field size and SSD = 100 cm for the Primus Mid Energy photon beam.

3.1.2 NOVAC7 accelerator

Novac7 (ENEA-Hitesys, Italy) is a robotic mobile intraoperative electron beam unit installed at the General Surgery Department. It has been designed as a very agile, movable making it possible to perform the Intraoperative electron radiation therapy (IEORT) treatment without any transport of the patient from the operating room to the radiotherapy bunker and without moving the patient from his position on the surgical bed. The accelerator is moved by a six axis robotic arm.

The dose is delivered to the patient's surgical breach, through a scattered electron beam collimated by plexiglas applicators (the diameter varies from 40 to 120 mm) attached to the radiating head (Figure 3.4). The applicators length is 80 cm, excluding the 100 mm applicator that is 100 cm long.

The most important Novac7 dosimetric characteristic is the very high dose-per-pulse ranging from 2.5 to 12 cGy/pulse, up to 100 times greater than the doses per pulse produced by a conventional accelerator (0.1 – 0.6 mGy/pulse). Dose-per-pulse rates can be obtained by varying the applicator's diameter and energy [104]. The duration of the pulse is of 4 μs and the pulse repetition rate is of 5 Hz. The high dose-per-pulse reduces the irradiation time during the surgery (typically 10 Gy are delivered in less than 1 minute). The energy choose depends on the depth of the tumor to treat.

Figure 3.4. Novac7 (ENEA-Hitesys) accelerator.

In Figure 3.5 are represented the percentage depth dose curves for each energy and 100 mm diameter applicator.

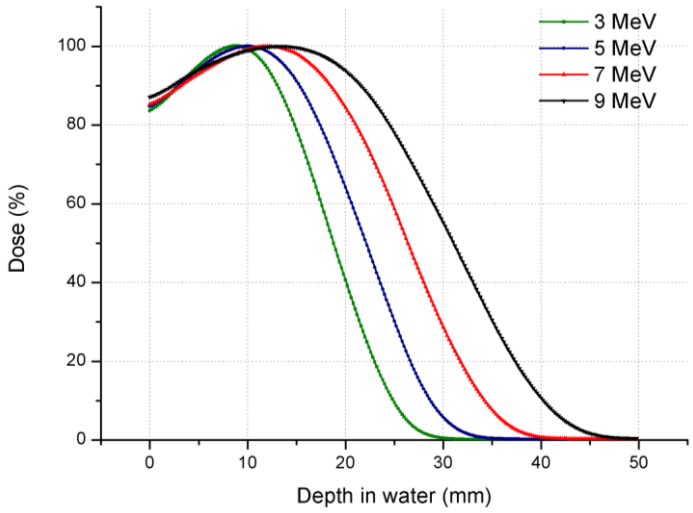

Figure 3.5. PDD curves for each energy and 100 mm diameter applicator.

In Table 3.2 are reported the depth dose values for each couple energy-applicator, measured on central beam axis with SSD of 100 cm.

Table 3.2. Depth dose values at each energy and applicator. Conventionally the energies are denoted as A (3 MeV), B (5 MeV), C (7 MeV), D (9 MeV). The R_x denotes the value of the water depth corresponding to a dose reduction of x% respect to the maximum dose value released at the depth R_{100}.

Energy		Applicator (mm)					
		40	50	60	70	80	100
A (3MeV)	R_{100} (mm)	8.8	8.8	8.6	8.8	8.8	8.8
	R_{50} (mm)	18.9	19	18.6	18.8	18.7	18.7
	R_{90} (mm)	13	13.1	12.8	13	13	13
	R_{80} (mm)	14.7	14.9	14.6	14.8	14.8	14.8
	R_{30} (mm)	21.5	21.6	21.2	21.5	21.4	21.4
		40	50	60	70	80	100
B (5 MeV)	R_{100} (mm)	9.8	10.2	10	10	10.4	10
	R_{50} (mm)	22.3	22.3	22	22	22	22.1
	R_{90} (mm)	15.2	15.5	15.3	15.3	15.4	15.3
	R_{80} (mm)	17.3	17.6	17.4	17.4	17.5	17.4
	R_{30} (mm)	25.1	25.3	24.9	24.9	24.9	25
		40	50	60	70	80	100
C (7 MeV)	R_{100} (mm)	11.6	11.8	12.4	11.9	12.2	12.2
	R_{50} (mm)	26.5	26.6	26.5	26.2	26.2	26.2
	R_{90} (mm)	18.3	18.5	18.6	18.6	18.6	18.4
	R_{80} (mm)	21	21.2	21.2	21.1	21.1	20.9
	R_{30} (mm)	29.9	30	29.9	29.5	29.5	29.6
		40	50	60	70	80	100
D (9 MeV)	R_{100} (mm)	13.2	13.4	12.4	13	13.8	13
	R_{50} (mm)	31.3	31.6	31.2	31	30.7	30.6
	R_{90} (mm)	21.5	21.9	21.6	21.6	21.5	21.4
	R_{80} (mm)	24.6	24.9	24.6	24.6	24.3	24.2
	R_{30} (mm)	35.4	35.7	35.2	35	34.7	34.6

It can be observed that the release of the maximum dose occurs at depths very similar for both electrons and photons. However, while the dose of electrons is released in a few cm from the entry point, the dose of photons is released at greater depths. These data confirms that the electrons are the most suitable particles to give the required dose of radiation directly to the tissues displayed during surgery, thus protecting the underlying healthy tissues.

3.2 Experimental setup for the use of TLDs

During this thesis a batch of 40 TL dosimeters has been calibrated and tested under photon and electron beam accelerators.

There are different types of TLD to lithium fluoride doped with magnesium and titanium, denominated TLD 100, TLD 600 and TLD 700; they differ in the percentage isotope of lithium, respectively:

- ^{6}Li 7.5% and ^{7}Li 92.5% for the TLD 100;
- ^{6}Li 95.6% ^{6}Li and ^{7}Li 4.4% for the TLD 600;
- ^{6}Li 0:01 ^{6}Li and ^{7}Li 99.99% for 700 TLD 700.

The thermoluminescence dosimeters used in this work are the LiF:Mg,Ti (TLD-100) (Harshaw Chemical Company) chips with nominal dimensions of $3.2 \times 3.2 \times 0.89$ mm^3.

TLD-100 is the most widely used TLD in routine personal dosimetry, environmental monitoring, space dosimetry and clinical dosimetry. This popularity is due to its approximate tissue equivalence (effective atomic number of 8.2, similar to 7.4 for tissue); low signal fading (5 - 10% per year), wide linear response range (10 μGy – 10 Gy); and high sensitivity for very low dose measurements [105, 106].

The main physical and dosimetric characteristic of TLD 100 are reported in Table 3.3.

Table 3.3. Physical and dosimetric characteristics of TLD 100.

Characteristic	LiF (TLD 100)
Size (mm^3)	3.1 x 3.1 x 0.89
Weight (mg)	24
Density (g/cm^3)	2.64
Effective atomic number	8.2
Emission spectrum (nm)	Range 350 - 600 Peak 400
Number of dosimetric peaks	3
Temperature of the main peak of the glow curve (°C)	195
Maximum temperature for reading (°C)	300
Doping elements	Mg, Ti
Thermal fading	5 to 10% per year
Linear response range	10 μGy – 10 Gy

Thermoluminescence dosimetry is based upon the ability of imperfect crystals to absorb and store the energy of ionizing radiation, which upon heating is re-emitted in the form of electromagnetic radiation, mainly in the visible wavelength. A basic TLD reader system consists of a planchet for placing and heating the TLD, a photomultipler (PMT) to detect the thermoluminescence light emission and convert it into an electrical signal linearly proportional to the detected photon fluence and an electrometer for recording the PMT signal as a charge or current. The charge is correlated to the absorbed dose received by the TL material. Heating and light collection are performed in the readout system Harshaw model 3500 manual TLD reader, installed at the Department of Physics of the University Federico II (Figure 3.6). TLDs have been read at 300 °C using a heating rate of 10 °C/s, to optimize the TL signal-to-background ratio in the high-temperature region. A continuous nitrogen flow was used to reduce chemoluminescence and spurious signals not related to the irradiation [107].

Figure 3.6. TLD Reader, 3500 model (Harshaw Company).

The TL signal as a function of temperature (or of time if this parameter is correlated with temperature) is of a complex nature and is called *glow curve*. It consists of different TL peaks, each peak corresponding to a different energy state in the crystal. The *software WinREMS* (Windows Radiation Evaluation and Management System) allows to visualize the value of the charge (nC) as a function of the temperature, that is the glow curve, for the current TLD.
After readout, the TL material is either entirely in its original state, and in this case it is just ready for re-use, or it requires a special heating treatment called annealing in order to restore it to its original state.

In Figure 3.7 is reported an example of glow curve of a TLD 100 of our batch.

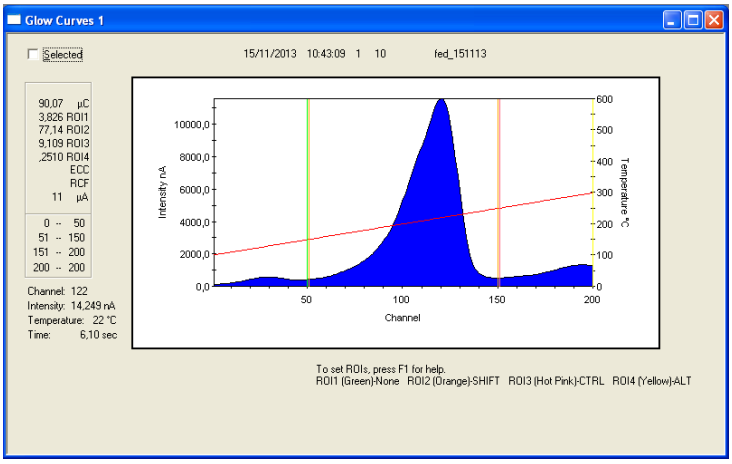

Figure 3.7. Glow curve of a TLD 100, the x-axis indicates the channel number, the y-axis indicates the current intensity (nA) of the signal detected by the PMT. The blue area is the TL response.

In the present work prior to each irradiation, TLDs were annealed in air at 400 °C for 1 hour, followed by a 2 hours annealing at 100 °C and by rapid cooling to room temperature [108] in a dedicated oven (Figure 3.8).

Figure 3.8. Oven used to the TLD annealing.

The irradiation experiments of the TLD were performed using 5, 7 and 9 MeV electron beams. An additional reference irradiation experiment was performed by a 6 MV photon beam to obtaining a TLD dose-response curve to be used as a benchmark for the performed method of analysis.

3.2.1 Sensitivity and calibration factor

Some variations in sensitivity within a batch of TL dosimeters is unavoidable. Several methods can be used to limit the effect of these variations when the dosimeters are in common use. The best method consists of irradiating all the dosimeters in the same geometrical conditions, to read them out and to attribute to each of them a sensitivity factor:

$$S_i = \frac{R_i}{\bar{R}} \tag{3.1}$$

where R_i is the TL readout from dosimeter number i and $\bar{R}$ the mean of all values of R_i.

This sensitivity factor expresses the response variation of each individual dosimeter around the mean. Although this mean may vary from irradiation to irradiation, S_i should remain constant because all dosimeters are subject to the same variations. Sensitivity factors should be checked periodically to take into account a possible loss of material occurring when TL dosimeters are not handled carefully.

A proper calibration with a secondary dosimeter provides the conversion factor of electric charge to dose units according to:

$$F_c = \frac{\bar{R}}{D_{ref}} \tag{3.2}$$

where $\bar{R}$ is the average response of the TLD irradiated at the reference dose value D_{ref}.

3.3 Fiber Bragg Grating

In this thesis Corning® SMF-28™ Single-Mode 6 mol% Ge-doped silica-core optical fibers have been investigated. Below some optical and geometry specifications have been reported:

Core Diameter = 8.2 μm
Numerical Aperture = 0.14
Refractive index difference = 0.36%

Effective Group Index of Refraction = 1.4677 at 1310 nm, 1.4682 at 1550 nm

Coating Diameter = 245 ± 5 µm

Cladding Diameter = 125.0 ± 0.7 µm

Coating-Cladding Concentricity < 12 µm

Operating Wavelength = 1200 nm ≤ λ ≤ 1600 nm

The refractive index profile and spectral attenuation of a typical fiber are illustrated in Fig. 3.9.

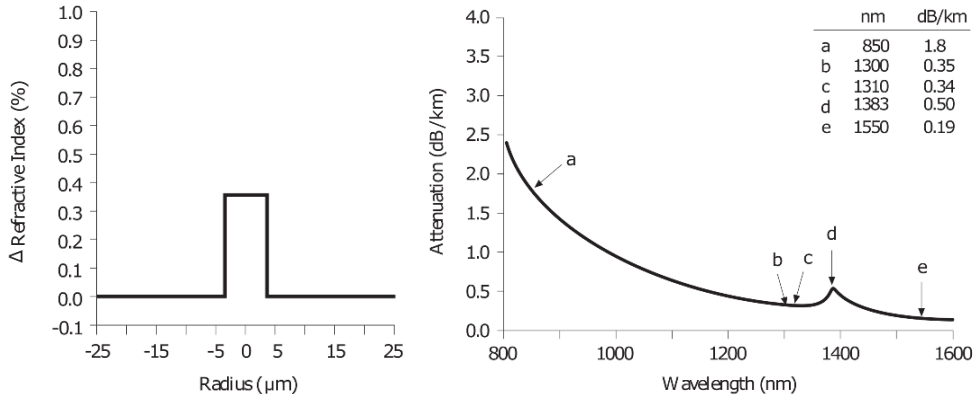

Figure 3.9. Refractive index profile (left panel) and a spectral attenuation (right panel) of a typical fiber.

The PS-FBG is written in a single mode optical fiber over a length of about 1 cm and it behaves as a localized high-quality optical resonator with a sensitive volume of only 6 x 10^{-4} mm^3 (the effective volume interacting with the radiation).

3.4 Physical characterization of optical fiber material

The photon interaction with the matter depends on the incoming photon energy [109] and the atomic number Z of the material. This interaction can be represented by physical quantities such as mass attenuation $\left(\frac{\mu}{\rho}\right)$ and energy-absorption $\left(\frac{\mu_{en}}{\rho}\right)$ coefficients, effective atomic number Z_{eff} and effective electron density (N_e).

The mass attenuation coefficient is a measure of the average number of interactions between incident photons and matter, that occur in a given mass-per-unit area thickness of the substance encountered [109]. Present-day interest in the mass energy-absorption coefficient $\left(\frac{\mu_{en}}{\rho}\right)$ is reflected in its use in the

recommendations and protocols of numerous organizations concerned with the standardization and traceability of radiation dosimetry.

The other important quantity - called “the effective electron number or electron density” - is defined as the electrons per unit mass of the absorber [110]. Several works have been carried out on the mass attenuation coefficients, effective atomic number and effective electron density for different types of materials [111-114]. In 1982 Hubbell published tables of mass attenuation coefficients and the mass energy-absorption coefficients for 40 elements and 45 mixtures and compounds over energy range from 1 keV to 20 MeV. These tables, although widely used, should now be replaced by the Hubbell and Seltzer tabulation for all elements (Z = 1 - 92) and 48 additional substances for dosimetric interest [115].

Berger and Hubbell developed the theoretical tables and computer program (XCOM)[3] for calculating attenuation coefficients for elements, compounds and mixtures for photon energies from 1 keV to 100 GeV [116-118]. This well known and much used program was transformed to the Windows platform by Gerward *et al.* [119] and the Windows version is being called WinXCom.

In this work the total and partial mass attenuation $\left(\frac{\mu}{\rho}\right)$ and mass energy-absorption coefficients $\left(\frac{\mu_{en}}{\rho}\right)$ were derived for all the constituent elements of the fiber material using the computer code “XCOM” at photon energies in the range between 1 keV and 20 MeV. The mentioned physical quantities were calculated in relation to the water, for the compound “fiber” according to the Bragg’s rule. The effective atomic number was derived and compared to that of the water presented in the literature reference.

The mass attenuation coefficients is given by

$$\left(\frac{\mu}{\rho}\right)_{compound} = \sum_i w_i \left(\frac{\mu}{\rho}\right)_i \tag{3.3}$$

where:

[3] Tables and graphs of the photon mass attenuation coefficient μ/ρ and the mass energy-absorption coefficient μ_{en}/ρ are presented for all of the elements Z = 1 to 92, and for 48 compounds and mixtures of radiological interest. The tables cover energies of the photon from 1 keV to 20 MeV. The μ/ρ values are taken from the current photon interaction database at the National Institute of Standards and Technology, and the μ_{en}/ρ values are based on the new calculations by Seltzer [69]. These tables of μ/ρ and μ_{en}/ρ replace and extend the tables given by Hubbell in the International Journal of Applied Radiation and Isotopes **33**, 1269 (1982).
http://www.nist.gov/pml/data/xraycoef/

w_i = Weight fraction of element in the compound

$\left(\frac{\mu}{\rho}\right)_i$ = Mass attenuation coefficient for individual element in the compound

The effective atomic number Z_{eff} of a material consisting of different elements can be obtained by the relation [120]:

$$Z_{eff} = \frac{\sigma_a}{\sigma_{el}} \tag{3.4}$$

where $\sigma_a$and σ_{el} represent the total atomic cross section and total electric cross section, respectively.

They can be obtained via the total mass attenuation coefficients [115, 120]:

$$\sigma_a = \frac{\left(\frac{\mu}{\rho}\right)_{compound}}{N_A \sum_i \frac{w_i}{A_i}} \tag{3.5}$$

$$\sigma_{el} = \frac{1}{N_A} \sum_i^n \frac{f_i A_i}{Z_i} \left(\frac{\mu}{\rho}\right)_i \tag{3.6}$$

where:

N_A = Avogradro's number

A_i = Atomic weight of constituent element of the compound

f_i = The number of atoms of element i relative to the total number of atoms of all elements in the compound

Z_i = The atomic number of the ith element in the compound

The effective atomic number is closely related to the electron density N_e, which is expressed in number of electrons per unit mass. For a chemical element, the electron density is given by $N_e = N_A\ Z/A$. This expression can be generalized to a compound, and one has

$$N_e = N_A \frac{n\ Z_{eff}}{\sum_i n_i\ A_i} = N_A \frac{Z_{eff}}{\langle A \rangle} \tag{3.7}$$

where $\langle A \rangle$ is the average atomic mass of the compound.

It can be shown that the electron density is given by

$$N_e = \frac{\mu/\rho}{\sigma_e} \tag{3.8}$$

where μ/ρ is the total mass attenuation coefficient of the compound, and σ_e is the electronic cross section given by Eq. (3.6).

3.5 Methods and apparatus for interrogating optical fiber sensors

The interrogation approach of FBG is based on laser-frequency stabilization and heterodyne detection techniques that lead to high signal-to-noise ratio and enable fast and active reading. The laser is frequency locked to a cavity mode using a Pound-Drever-Hall scheme [121]. By scanning the fiber temperature and monitoring the laser wavelength, the thermo-optic response is retrieved. A picture of the experimental apparatus is shown in Figure 3.10a and the relative sketch in Figure 3.10(b).

A 10 mW DFB Er-fiber laser emitting around 1560 nm (Koheras Adjustik™, Birkerød, Denmark) is phase modulated at 72 MHz by an all-fiber electro-optic modulator. After modulation two sidebands are generated and overlapped to the laser carrier. This triplet enters the first port of a fiber circulator and then injects the FBG-cavity. When the cavity is on resonance, the sidebands are reflected back by the first FBG and interfere with the carrier resonating into the cavity. The whole reflected field beam exits the second port of the circulator and is detected by a fast (2 GHz) InGaAs photodetector whose output beats with the RF signal in a mixer yielding a dispersive error signal (Figure 3.12(b)).

The detector signal is demodulated with the 72 MHz modulation signal in a radiofrequency mixer, yielding an error signal, centered around the cavity mode, which is filtered and amplified by a servo system. The servo signal is finally fed back to the laser current, in order to lock its frequency to a cavity mode. The FBG cavity is inserted into a thermally controlled chamber and its temperature is carefully monitored by a high sensitivity (1 mK) negative temperature coefficient (NTC) resistor placed in contact with the fiber (Figure 3.11). Once the laser is locked to the cavity, the chamber temperature is slightly varied (by less than 1 °C) around the ambient temperature (25 °C). The cavity transmitted light is collected by a high

resolution (minimum $\delta\lambda = 4x10^{-4}\ nm$) lambda-meter (Burleigh, WA-1500) that measures the center wavelength of the resonating cavity mode in real-time.

The center resonance of one PS-FBG cavity is shown in Figure 3.12(a) (in transmission) along with part of the power modulation due to the FBG envelope curve during a wide sweep of the laser current. A zoom of the same resonance in reflection is plotted with the corresponding Pound-Drever-Hall (PDH) error signal (Figure 3.12(b)).

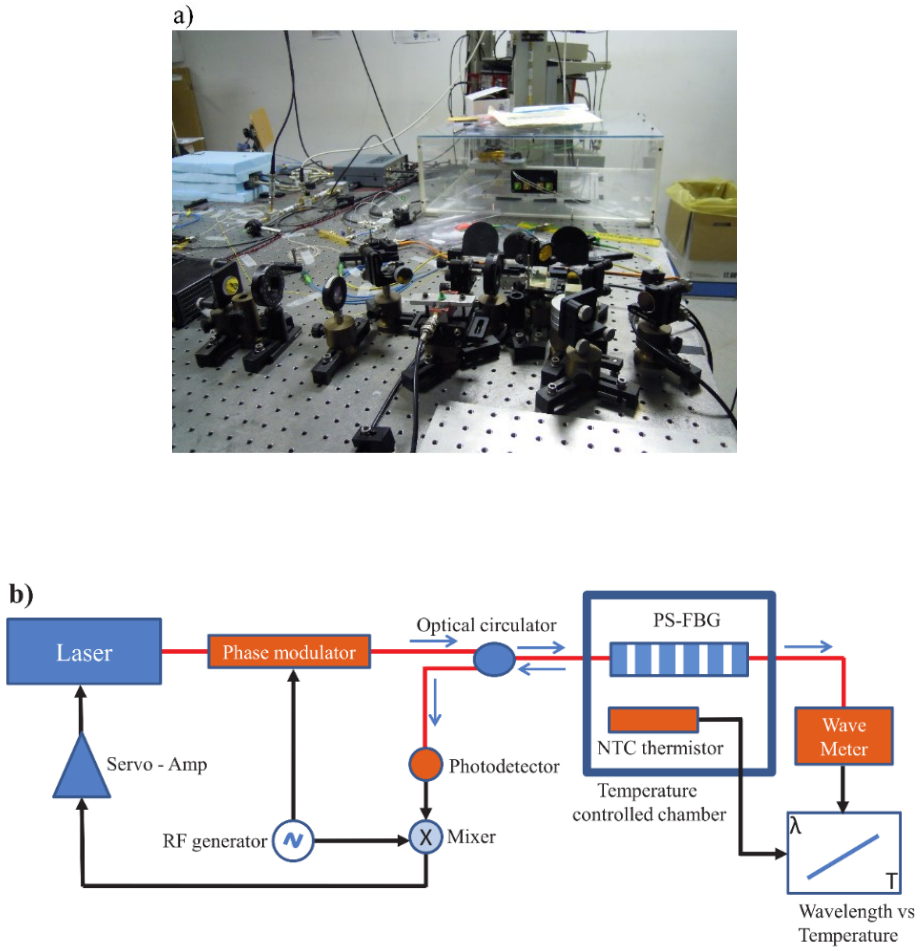

Figure 3.10. Picture (a) and the sketch (b) of the experimental apparatus. The sketch describes the interrogation unit where a laser is used to actively track the PS-FBG resonator by a frequency locking technique. At the same time, a wavelength meter provides a measurement of the wavelength shift due to IRs delivered to the fiber that is temperature controlled in an insulated chamber.

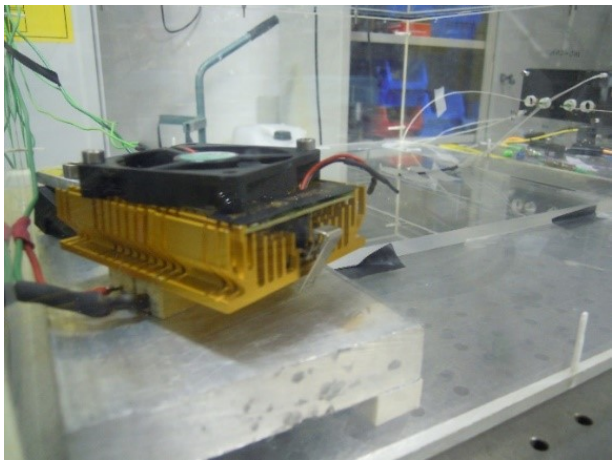

Figure 3.11. Picture of the negative temperature coefficient (NTC) resistor placed in contact with the fiber.

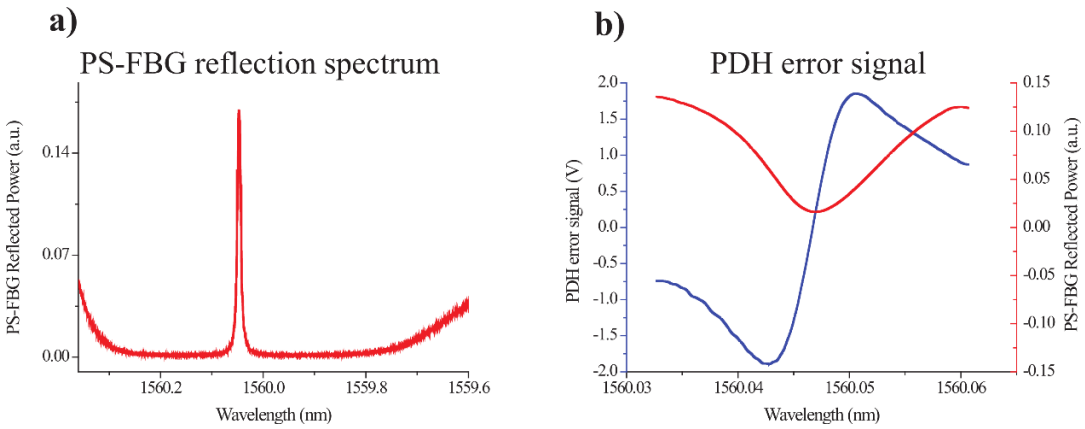

Figure 3.12. Center resonance of one PS-FBG cavity (a) (in transmission) along with part of the power modulation due to the FBG envelope curve during a wide sweep of the laser current. (b) A zoom of the same resonance in reflection (red line) is plotted with the corresponding Pound-Drever-Hall (PDH) error signal (blue line).

Part II

Tools and procedures for NTCP optimization

3.6 Planning in the radiation therapy treatment

For NTCP modeling different patient cohorts were evaluated. For all patients, the RT treatment plans were planned in XIO Treatment Planning System (XiO 4.64, Elekta CMS).

The radiotherapy treatments were guided by Radiation Therapy Oncology Group (RTOG) and International Commission on Radiation Units and Measurements (ICRU) protocols for the dose-homogeneity and conformality conditions in the tumor targets, and the dose-volume constraints in the critical organs. RT was administered with 6 - to 20 - MV photon beams from a linear accelerator in daily fractions (range 1.5 - 2 Gy) for a total number that depends by the prescription dose to specific targets Treatment planning was based on computed tomography (CT). The delineation of PTV and OARs was performed according to the RTOG guidelines [122-124] and reviewed by the same radiation oncologist. The prescription dose was specified at the center of the PTV and the field weightings were adjusted to achieve 95% of prescription dose to 95% of the PTV. The radiotherapy plans have been evaluated thought the visualization of dose-volume histograms (DVHs).

3.7 Computational environment for data extraction and analysis

For each patient the treatment plan was recovered from tapes archives. After de-archiving, 3D treatment plans were imported into a custom treatment plan analysis system CERR (A Computational Environment for Radiotherapy Research), an open source, freely available general treatment plan analysis package

based on Matlab developed and maintained by the School of Medicine and Siteman Cancer Center, Washington University, St. Louis. In combination with CERR the tool DRESS (Dose REsponse Explorer System)/Matlab, provides an environment for analyzing treatment outcomes.

CERR capabilities for radiotherapy treatment response modelling include the following:

1. the ability to convert the widely available AAPM/RTOG treatment planning format into a MATLAB cell-array data object, facilitating manipulation;
2. a treatment plan data architecture which is self-describing, compact, easily manipulable, and extendable;
3. the ability to manipulate treatment plans within a powerful data analysis and programming environment, for example for dose-volume-outcomes analyses;
4. visual plan review tools (axial, sagittal, and coronal viewers);
5. the source code is supplied, allowing users to modify it and use it as a template for their own projects;
6. the ability to link external programs in other languages;
7. CERR can be used for sharing and reproducing radiation therapy treatment planning research results. CERR is highly useful for defining and generating new candidate variables. New structure field names can be added dynamically or permanently. New components of arbitrary data type can be stored and accessed without disturbing system operation.

In this thesis we used CERR to provide the input data format to DREES, based on Matlab's human-readable data structures. The internal database structure is called *ddbS (*for DREES database structure*)*. There are currently two reserved key words in this structure; ddbS.dvh (reserved to automate processing of different dose–volume histograms), and ddbS.outcomes (reserved to identify endpoints). The dvh field can take on any extension, which will be treated by the software as a different dose–volume histogram type (e.g., dvh lung and dvh heart). The outcomes field is reserved for the observed complication in NTCP (e.g., discrete grades 0 – 5 post-radiation pneumonitis in lung cancer) or tumor control in TCP (e.g., 0: failure or 1: local control in tumor). Dose–volume metrics are internally derived from the dvh of interest by the software (or directly imported dose data), which include mean dose, maximum dose, minimum dose, V_x (percentage volume receiving at least x Gy), D_x (minimum dose to x% highest dose volume) and GEUD

(generalized equivalent uniform dose). The increment parameter 'x' in D_x/V_x and exponent *a* in GEUD are assigned interactively by the user. Clinical factors such as age, gender, ethnicity, stage, chemo administration are extracted from the fields of the 'ddbS' structure and populated directly into the software menu's list of variables.

DREES provides many radiotherapy outcome modelling features, including:

1. combined modelling of multiple dose–volume variables (e.g., mean dose, max dose, etc) and clinical factors (age, gender, stage, etc) using multi-term regression modelling. Multi-metric models are phenomenological and depend on the parameters available from the collected clinical and dosimetric data (i.e., data driven) [125];
2. manual or automated selection of logistic or actuarial model variables using bootstrap statistical resampling;
3. estimation of uncertainty in model parameters;
4. performance assessment of univariate and multivariate analyses;
5. graphical capabilities to visualize NTCP or TCP prediction versus selected variable models using various plots.

In this work DREES tool was used for multi-metric modelling while in house-written Matlab scripts were run to perform LKB and RS models. In the following sections we'll focus on the methods for data-driven modelling which requires a pre-processing and manipulation of clinical and dosimetric data. The algorithm to fit the analytic NTCP model parameters is reported in Appendix C.

3.7.1 Maximum likelihood method

Multi-metric technique can be used to model NTCP or TCP depending on the nature of the observed output and endpoint selection [34].

The currently implemented multivariate method is based on logistic regression (see Eqs. (1.4)-(1.5)). Mathematically, the relationship between the predictive variables (e.g., dose–volume metrics and clinical factors) and the observed data is represented with an additive sigmoidal model, where the model coefficients are determined by *Maximum Likelihood* (ML) method that is, maximizing the probability that the data give rise to the observations [126-128].

In order to apply this method first a function is constructed, called the log-likelihood function (LLH), defined as:

$$LLH(\beta) = \sum_{y(i)=1} \ln(NTCP(x_i)) + \sum_{y(i)=0} \ln(1 - NTCP(x_i)) \quad (3.9)$$

x_i is the vector of the input variable values used to predict the probability $NTCP(x_i)$, β is the vector of the set of model coefficients, $y(i)$ is the binary outcome.

Numerically, the set of nonlinear likelihood equations are solved using an iterative weighted least-squares method [129]. The parameters' uncertainties are estimated by using Wald's statistic [126, 127].

Analytic models are based on dose-volume variables (see Eqs. (1.9)-(1.12)). The LLH function was numerically maximized by the Nelder-Mead Simplex Method (Matlab implementation: FMINSEARCH function) using an in-house developed library for Matlab. Ninety five percent confidence intervals for parameters estimates were obtained using the profile likelihood method [130]. Following this method, each parameter belonging to the set $(D_{50},\ m,\ n)_{LKB}$ or equivalently to the set $(D_{50},\ \gamma,\ s)_{RS}$ was varied around its Maximum Likelihood Estimation (MLE) [131-133] (optimum LLH) while the other 2 parameters were fixed at their ML estimate. The 95% confidence bounds were determined reducing the maximum LLH by one half of the x2 inverse cumulative distribution function associated with a 95% confidence level, so as to obtain the iso-likelihood contours in each Cartesian plane of the parameters space $(D_{50},\ m,\ n)$, or equivalently, of the $(D_{50},\ \gamma,\ s)$ space. In correspondence to the parameters values belonging to the iso-likelihood contours, a bundle of NTCP curves was calculated and the 95% confidence region for the model fit was thus estimated. In terms of the LKB model parameters the expression of LLH (see Eq. (3.9)) becomes:

$$LLH\left(D_{50,}\, m, n\right) = \sum_{y(i)=1} \ln(NTCP(D_{50,}\, m, n)) + \sum_{y(i)=0} \ln(1 - NTCP(D_{50,}\, m, n)) \quad (3.10)$$

3.7.2 Variable candidates and best model selection

The model building methodology has several steps. First it is desirable to test any variable, simple or derived, that may potentially add to the prognostic value of the model. Clinical factors include, for example, diabetes, surgery, chemotherapy, age, patient performance status, etc. Dosimetric factors may include V_x values (the percentage volume that received a dose greater or equal to x Gy, e.g. V_{20}), D_x values

(minimum dose given to the hottest *x*% volume) mean dose. To facilitate initial data exploration, was used a graphical display that refer to as the "self-correlation" display. The Figure 3.13 shows an example of the self-correlation matrix for the prostate data sets. Each color matrix element represents the magnitude of the Spearman's rank correlation coefficient between two variables.

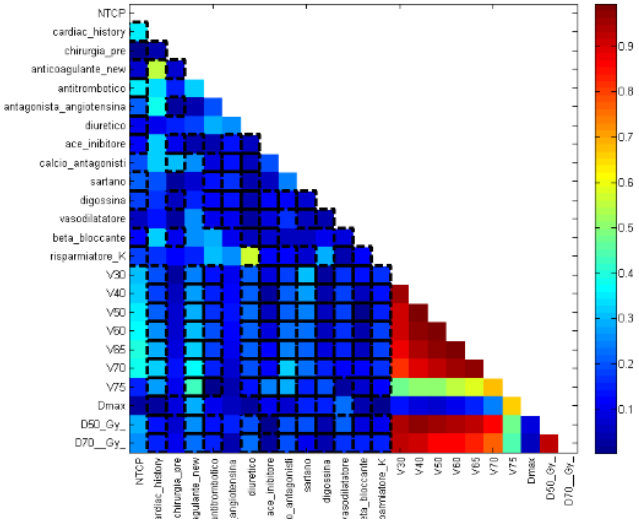

Figure 3.13. The self-correlation matrix for dosimetric and clinical factors that may affect gastrointestinal disorders. Note the significant intercorrelations between many V_x values (volume area receiving greater than x Gy) below 65 Gy.

Constructing the logistic model requires selection of the best combination of variables, without trying all possible combinations of relevant variables (which is too computationally expensive). First, starting from the self-correlation matrix the number of D_x, V_x and clinical variables under consideration was pruned to leave only variables between which inter-variable Spearman correlations were less than a 0.85 to avoid overfitting. Within the framework of a given set of candidate variables and sequential forward selection, we need a reliable method of determining when the model has reached maximum predictive power. An optimal model order was defined by automating forward step regression and computing average prediction performance on cross-validation. There are several empiric methods for selecting model order, including several approaches derived from the bootstrap principle. In brief, the bootstrap assumes that a good approximation for a new data set drawn from the same population can be constructed by randomly sampling original data points and adding them to a "replicate" bootstrap data set. Any data point may be selected multiple times. The sampling process continues

until the replicate set has as many data points as the original data set. By repeating the model fitting process on the replicate set, parameter estimate variance and model stability can be assessed. An apparent weakness of the bootstrap is that each replicate, on average, contains only 63% of the original data points (Many of the included points are duplicated once or more). A bootstrap replicate is therefore not as descriptively powerful as the original data set. Many bootstrap replicates (multiple times the data's sample size) should be generated to achieve convergence to the right model order, which would make it computationally too expensive in this case.

Another attractive empiric alternative is the cross-validation leave-one-out method (LOO-CV) (also known as the "jackknife"). In this technique, the model is refit to modified data sets a number of times equal to the number of data points. For each refit, a different data point is left out. We use this by then tabulating the model prediction for the data point left out These predictions are ranked, and Spearman's coefficient is computed as usual. The main advantage of this over the bootstrap-based methods is that nearly all the original data are used to build the model. LOO-CV therefore minimizes the bootstrap problem of weakening the validity of the fitted parameters as a result of using a smaller, less powerful data set. If the model varies significantly between runs (say, because two different variables have a significant likelihood of being chosen), the LOO-CV method may not lead to a reliable Spearman's value. In practice, nearly optimal model order implies relatively stable models between runs. In our tests, model instability between leave-one-out runs was not an important issue. However, the results tend to be noisier than the bootstrap case. This would lead one to think of the bootstrap approach as a smoothed LOO-CV.

The robustness of the variable sets selected was tested by cataloging the frequency of variable sets selected based on model refitting of bootstrap datasets [34]. Further details for this data-mining method to select variables and define models are described in [34, 134]. In summary the modeling process consists of a 2-step process. In the first step, the model size (number of variables significantly predictive) is estimated by bootstrapping, and in the second step regression coefficients are estimated by using forward selection on multiple bootstrap samples, the most frequent model being the optimal one. An example for automated data modelling is given in Figure 3.14.

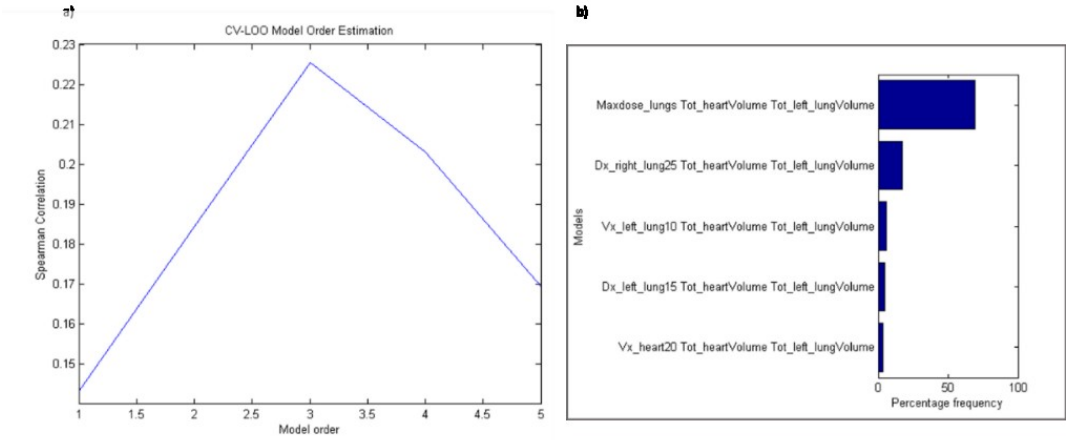

Figure 3.14. Automated multi-metric model determination for heart valve dysfunction generated by DREES. (a) Model order selection using leave-one-out cross-validation. The model order is determined to be 3. (b) The parameters for the order 3 model are determined by forward selection and bootstrapping. Similar models are coalesced and the model frequencies for the top five models are shown.

3.7.3 Model comparison

Model predictive power was quantified by use of Spearman's rank correlation coefficient, and the area under the curve (AUC) of receiver operating characteristic (ROC) curve was used to evaluate the discriminating ability of model fits. A ROC graph is a plot of the true positive fraction (sensitivity) versus the false positive fraction (1-specificity) for a continuum of threshold values. An example of ROC curve is reported in Figure 3.15. The ROC curve was created by plotting the fraction of true positives out of the total actual positives (TPR = true positive rate or sensitivity) vs. the fraction of false positives out of the total actual negatives (FPR = false positive rate or 1-specificity), at various probability threshold settings. The discrimination value on the ROC curve was determined by Youden's J statistic that is the difference between the TPR and the FPR. Maximizing this indicates an optimal cut-off point. ROC curve results of different NTCP models were compared using a Z test. Statistics was performed using SPSS Statistics 18 and MedCalc (MedCalc, Mariakerke, Belgium).

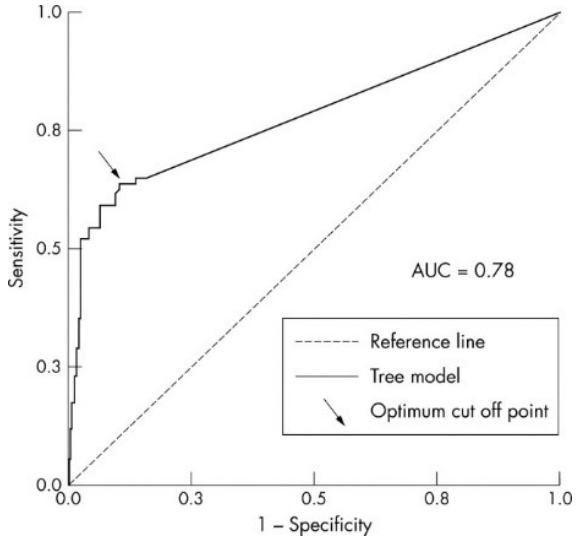

Figure 3.15. A ROC curve: the true positive rate (Sensitivity) is plotted in function of the false positive rate (100 - Specificity) for different cut-off points. Each point on the ROC curve represents a sensitivity/specificity pair corresponding to a particular decision threshold. A test with perfect discrimination (no overlap in the two distributions) has a ROC curve that passes through the upper left corner (100% sensitivity, 100% specificity). Therefore the closer the ROC curve is to the upper left corner, the higher the overall accuracy of the test.

CHAPTER 4

Results and Discussions

The purpose of the present chapter is to give a detailed description of the results and discussions of the two topics of the research activity. The study concerning the water equivalency investigation of the fiber sensor will be shown. Among the parameters representing radiation interaction with materials, we are particularly interested in the "effective atomic number", the most convenient parameter for representing X-ray and gamma ray interactions, since it allows many characteristics of material to be visualized with a number. The procedures of the photo-induction experiments with two FBGs sensors and with a resonant cavity will be describe, showing their capability to detect biomedical dose levels.

Furthermore in this chapter will be reported the dose response of well-established dosimeters, the TLDs, irradiated with non-conventional accelerator beam, such as high dose-per-pulse electron beam. Finally data-driven logistic Normal Tissue Complications Probability models compared with the classical models for different patient cohorts, organs at risk and end-points will be presented.

Part I

Dosimeter characterization and experiments

4.1 Water equivalency investigation of optical fiber sensor

The optical fiber sensors studied herein have been 6 mol% Ge-doped silica optical fibers. Elemental weight fractions of water, and both core and cladding of the fiber are showed in Table 4.1. The calculated radiological properties have included electron density N_e, effective atomic number Z_{eff}, mass attenuation and energy absorption coefficients.

Table 4.1. Elemental composition and fractional weight (w_k) for the core and cladding of the fiber and water.

Material	w_O	w_{Si}	w_{Ge}	w_H
Core	0.4944	0.4340	0.0716	-
Cladding	0.5326	0.4674	-	-
Water	0.8881	-	-	0.1119

The amount of oxygen in core and cladding is lower than that in water by approximately 44.3% and 44.0% respectively. In addition, both core and cladding contain silicon and no hydrogen and the core contains germanium too. The content of silicon in the core is 7.1% lower than in the cladding.

The electron density and the effective atomic number aren't constant for a material but a parameter varying with photon energy depending on the interaction processes involved.

Figure 4.1 shows the calculated fractional interaction probabilities for core, cladding and water over the energy range 1 KeV - 20 MeV.

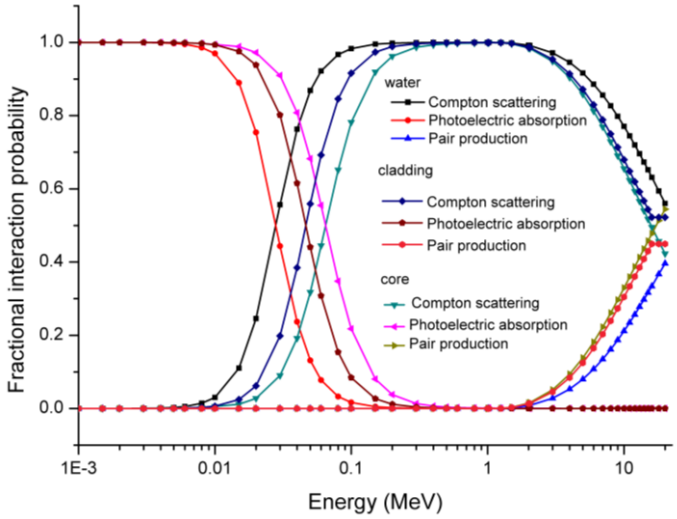

Figure 4.1. Fractional interaction probabilities for core, cladding and water.

As indicated in Figure 4.1, photoelectric absorption is the dominant interaction process for energies up to 30 KeV for water and up to 40 KeV and 50 keV for cladding and core respectively. Over the photon energy range 1 KeV - 30 KeV, the maximum relative difference in the photoelectric absorption fractional interaction probabilities of cladding is 44.6% and of core is 51.2% compared to water. These differences can be attributed to the strong dependence of photoelectric absorption on atomic number (approximately Z^3).

As energy increases, the difference in the photoelectric absorption fractional interaction probabilities of the core and cladding with water increases and reaches up to about 95% and 82% for core and cladding, respectively at 100 - 150 KeV.

However, Compton scattering dominates over photoelectric absorption in attenuating photons at these energies. As Figure 4.1 shows, Compton scattering becomes the dominant interaction process for the core, cladding and water above 50 KeV and it remains the dominant interaction up to 20 MeV.

The average ratio in the energy range 100 KeV - 20 MeV between the total interaction probabilities of core and cladding with water assessed at the values of 3.5 ± 0.3 and 3.2 ± 0.3 respectively as showed in Figure 4.2.

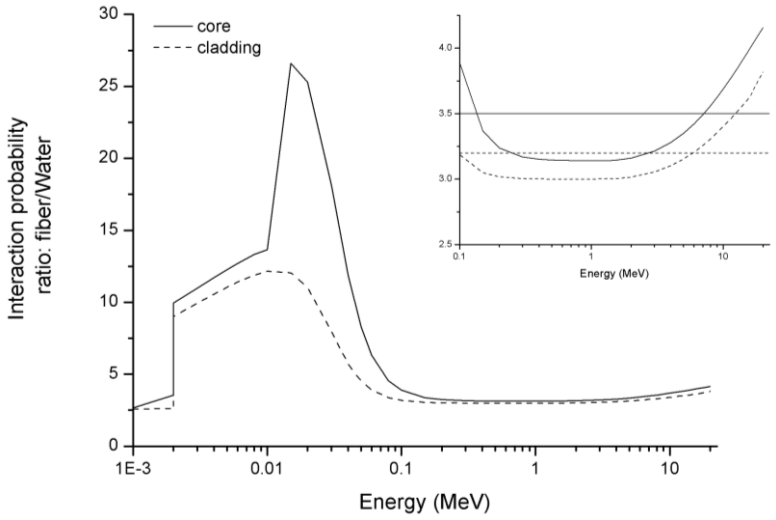

Figure 4.2. The interaction probability ratio between fiber materials and water. In the inset, the interaction probability ratio over the energy range 100 KeV - 20 MeV.

Figures 4.3a-b shows mass attenuation coefficients and the mass energy absorption coefficients ratio of the fiber materials relative to water for photon energies 1 KeV - 20 MeV.

For energies lower than 100 KeV, the mass attenuation coefficients of both the core and cladding reaches to 7.1 and 3.5 times that of water, respectively. Similarly the mass absorption coefficient reaches to 9 and 4 times that of water, for core and cladding respectively. Over this energy range photoabsorption dominates and due to the Z^3 dependence, despite the lower amount of oxygen, the presence of high atomic number elements in the core and cladding (germanium and silicon) may be responsible for this discrepancy compared to water.

As energy increases, Compton scattering becomes more important and for energies higher than 100 KeV the relative difference between the mass attenuation and absorption of fiber material and water falls to less than 10%. In the energy range 100 KeV - 20 MeV the ratios of the relative mass attenuation and energy absorption coefficients remains fairly constant.

In particular the average mass attenuation coefficient ratios in this energy range for core and cladding are 0.96 ± 0.09 and 0.9 ± 0.1, respectively.

The average mass energy absorption coefficient ratios in the energy range 100 KeV - 20 MeV for core and cladding are 1.0 ± 0.3 and 0.97 ± 0.11, respectively.

The very close agreement in mass attenuation coefficients over the energy range 1 KeV - 20 MeV can be explained by considering that for the low effective atomic number considered here, virtually all the energy transferred is deposited locally in

collisions, with only a negligible amount lost to bremsstrahlung radiation at the highest energies.

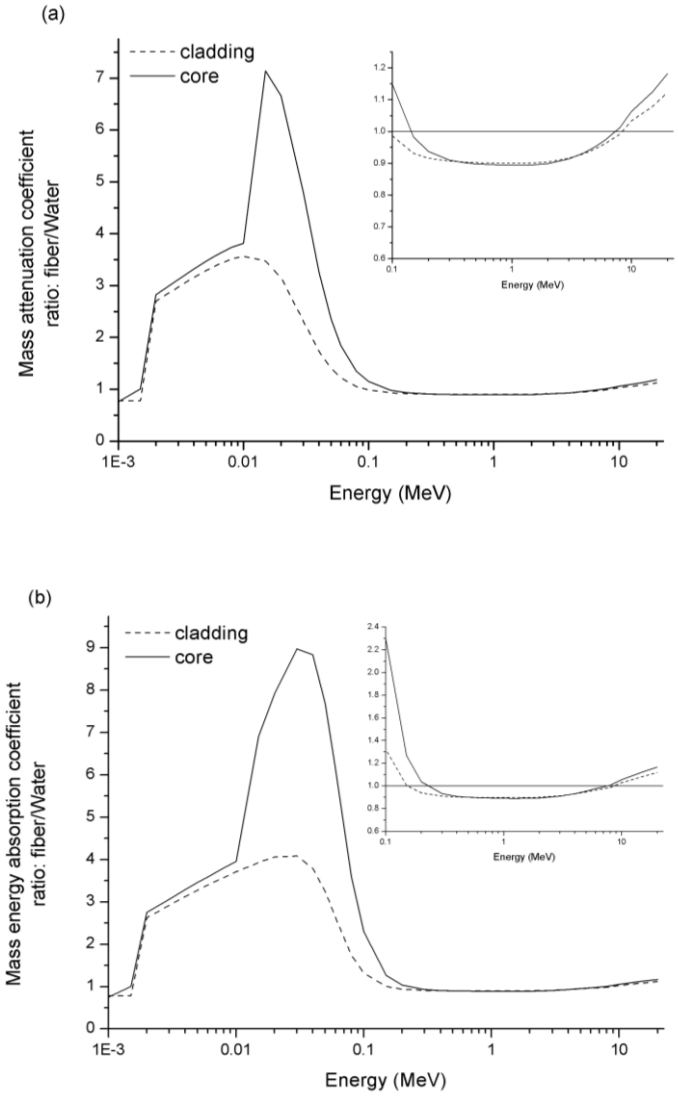

Figure 4.3. Mass attenuation coefficients (a) and the mass energy absorption coefficients (b) ratio of the fiber materials relative to water. In the inset, the mass attenuation coefficients and the mass energy absorption coefficients ratio over the energy range 100 KeV - 20 MeV.

The values of effective electron density N_e as a function of photon energy in the range between 1 keV to 20 MeV, has been calculated using Eq. (3.8) and showed in Figure 4.4. The behaviour of the electron density and of the effective atomic number as a function of the photon energy, reflects the interaction properties of the fiber material, descripted above.

The average values of electron density of core and cladding over the energy range 1 KeV - 20 MeV resulted to be 3.1 ± 0.1 and 3.03 ± 0.03, respectively.

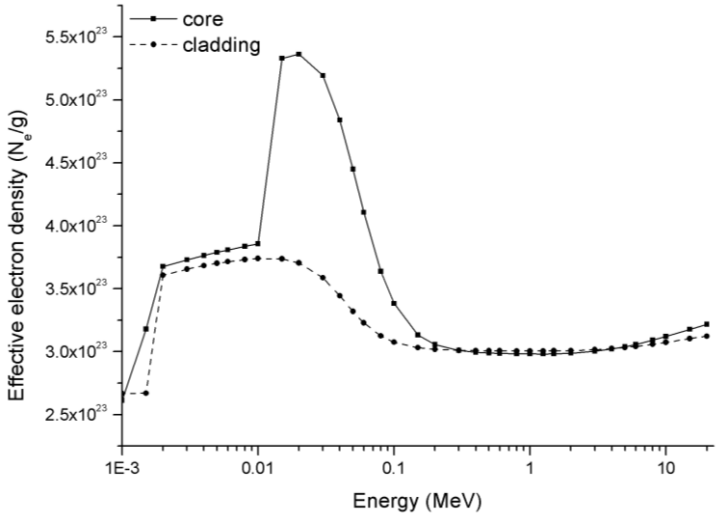

Figure 4.4. Effective electron density as a function of photon energy.

Using the mass attenuation coefficients by the Eqs. (3.4)-(3.6) the effective atomic number of Z_{eff} for the core and cladding at photon energies in the range between 1 keV to 20 MeV have been calculated and the results have been displayed in Figure 4.5.

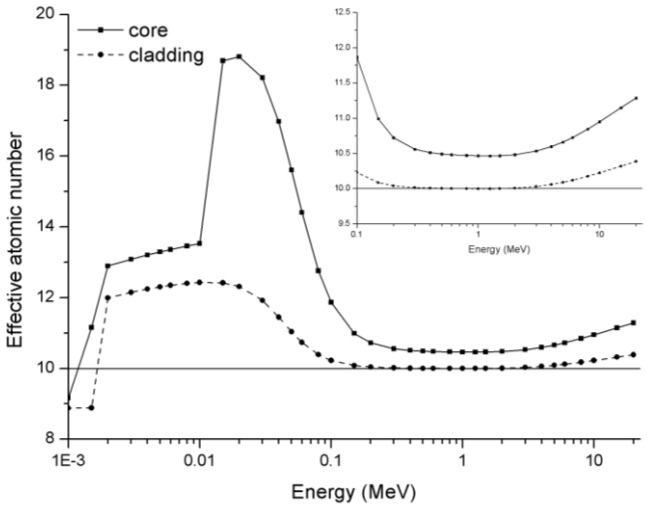

Figure 4.5. Effective atomic number as a function of photon energy. The straight line corresponds to the value of Z_{eff} =10.

The average values of the effective atomic number of core and cladding over the energy range of radiation therapy application 100 KeV - 6 MeV were 10.6 ± 0.3 and

100 KeV - 6 MeV were 10.6 ± 0.3 and 10.04 ± 0.06, respectively.

Finally we provided a single effective atomic number for the optical fiber sensor Z_{eff} as average value of core and cladding, weighed on the radius size.

The average value of the effective atomic number of the optical fiber sensor resulted to be:

$$Z_{eff} = 10.1 \pm 0.4$$

Since a large Z_{eff} generally corresponds to inorganic compounds and metals, a small $Z_{eff} \leq 10$ is an indicator of the organic substances. Considering that the Z_{eff} of water reported in literature is 7. 417 [135], we concluded that for a large range of energies of interest in radiation therapy, sensor can be considered water equivalent.

4.2 Detecting ionizing radiation with optical fiber sensors down to biomedical doses

The sensor was irradiated by the accelerator beam at different dose levels. Before the irradiation, the beam output (Gy/UM) of the linac was verified according to the recommendations of international protocol [16] using a Farmer chamber type (PTW type 30001, Freiburg, Germany). The chamber was connected to a PTW UNIDOS model E T10008–80361 electrometer. The set up was shown in Figure 4.6.

Figure 4.6. Picture of the set up for the measurement of the Primus Siemens accelerator output. PTW Farmer 3006 chamber was placed in a water equivalent slab phantom at 5 cm depth with a 1 cm backscatter slab. The photon beam was delivered setting 100 MU, 10 x 10 cm² square field, 100 cm of source to isocenter distance.

The fiber was placed in the water equivalent slab phantom at 5 cm depth with a 5 cm backscatter slab (Figure 4.7) and irradiated at different dose levels in controlled and reproducible conditions (10 x 10 cm^2 square field, source to isocenter distance 100 cm).

Figures 4.8a-b show the pictures of the fiber and the accelerator during an irradiation section.

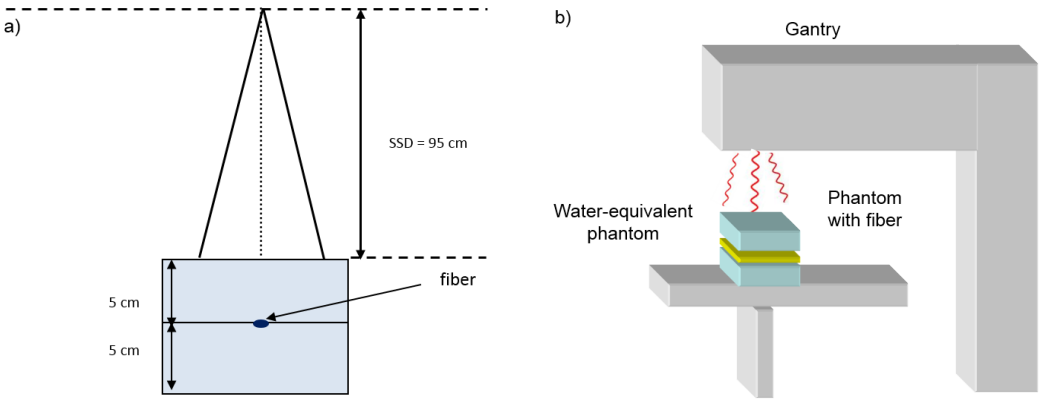

Figure 4.7. Frontal (a) and (b) lateral perspective of the experimental setup for the irradiation of the optical fiber: the fiber is placed in a water equivalent PMMA slab phantom at 5 cm depth with a 5 cm backscatter slab.

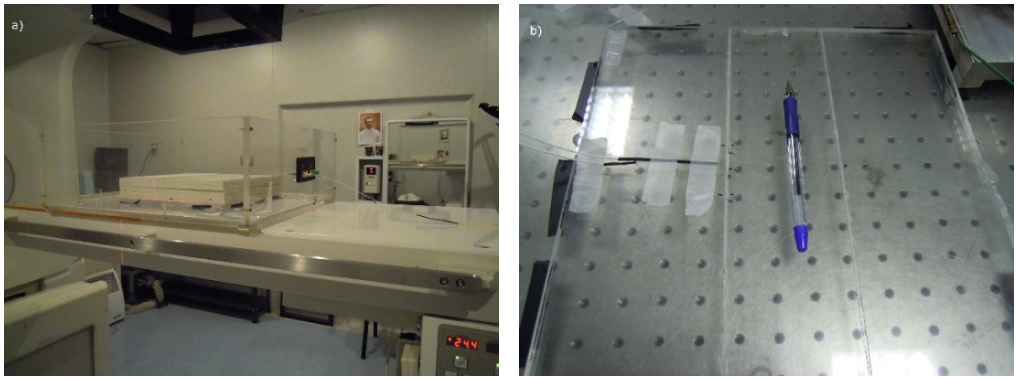

Figure 4.8. (a) Picture of the experimental set up for the irradiation with (b) a zoom on the phantom with the fixed fiber.

4.2.1 FBGs sensors response

A first sensor (PS-FBG-1) was irradiated with 10-Gy increments, up to 30 Gy. For this sensor, we initially used a closed box without active temperature control. After each irradiation step, the wavelength shift of the center resonance was

measured as described in the previous chapter. A net wavelength shift was measured when the laser was re-locked to the resonance, for a given temperature (Figure 4.9). The temperature of the whole fiber was then changed by a heat source in the box over a range of about 1 K, in order to check whether the wavelength shift was a false effect due to thermal drifts in the sensor between subsequent measurements.

The corresponding variation of the wavelength with the temperature showed a linear trend, although with relatively large experimental point dispersion along the fit lines, likely due to thermal instabilities. Nevertheless, by linear fitting of experimental data, we obtained an average measurement uncertainty on the thermos-optic response, i.e., the slope of the curves, of about 1.5 pm/K (4% relative error).

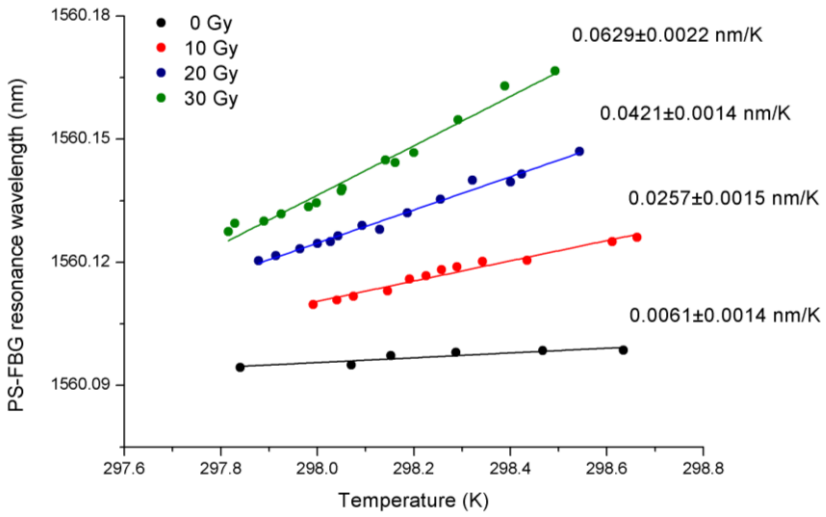

Figure 4.9. Experimental evidence of the radiation effect on the fiber sensor PSFBG-1. Besides a wavelength shift, the irradiation steps cause a large change of the thermo-optic response (the thermo-optic response is indicated for each fit line). As a result, the slope of the wavelength vs temperature fit line is amplified by about a factor 10 after 30 Gy [136].

A second sensor (PS-FBG-2) was irradiated at smaller doses with steps of 1 Gy. The sensor was fabricated with a higher envelope reflectivity and thus slightly different spectral features with respect to the previous one. In this way, the center mode linewidth was made much narrower (~ 10 times) in order to maximize the laser frequency stability while it was locked to the PS-FBG peak, thus improving the resolution when measuring the temperature response. In this case, a fine temperature control was devised relying on a highly insulated oven-controlled chamber.

In order to check the system reproducibility, three repeated measurements of the wavelength shifts vs temperature were made before irradiation (Figure 4.10). We noted that the thermo-optic response of PS-FBG-2 was significantly larger than that of the previous sensor. This behavior originates from the higher reflectivity of this grating.

The thermo-optic response values obtained from the three measurements were consistent within two standard deviations (reproducibility ~ 2%). A reduction of the wavelength fluctuations along the curves can also be appreciated, owing to the improved temperature control.

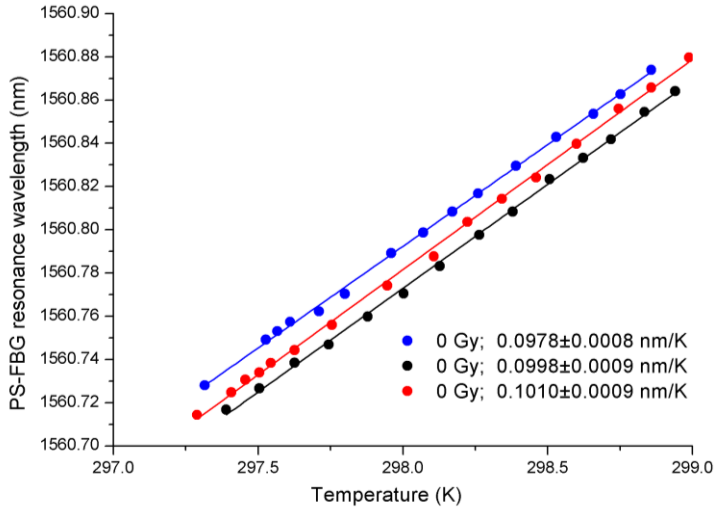

Figure 4.10. Reproducibility test of the thermo-optic response curve for the higher-reflectivity PS-FBG-2 resonator. It is worth noting that its narrower cavity mode exhibits a temperature response about 16 times larger than for PS-FBG-1 [136].

Thermo-optic response of PS-FBG-2 after irradiation is shown in Figure 4.11.

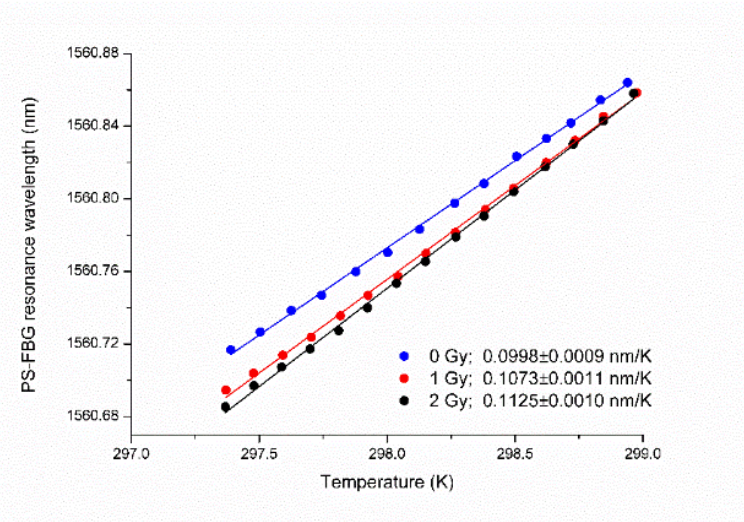

Figure 4.11. Wavelength shift for the irradiation steps and thermo-optic response for subsequent irradiations with low doses (PS-FBG-2) [136].

However, the curve offsets of the thermo-optic responses are not consistent with the incremental dose delivered. On the contrary, the thermo-optic response as a function of the accumulated dose shows clear evidence of the effect of the radiation on the fiber.

It's important point out the linear dependence as shown in Figures 4.12a-b. The figures show a linear trend of the radiation-induced thermo-optic response change *versus* the dose, with a coefficient of 0.00185 ± 0.00006 nm/K/Gy for the first sensor and 0.0063 ± 0.0006 nm/K/Gy for the second one.

Dividing the dose response coefficient by the average value of the uncertainty on the single measurement of the thermo-optic response (1 pm/K), we obtained a final resolution of 160 mGy for the second sensor.

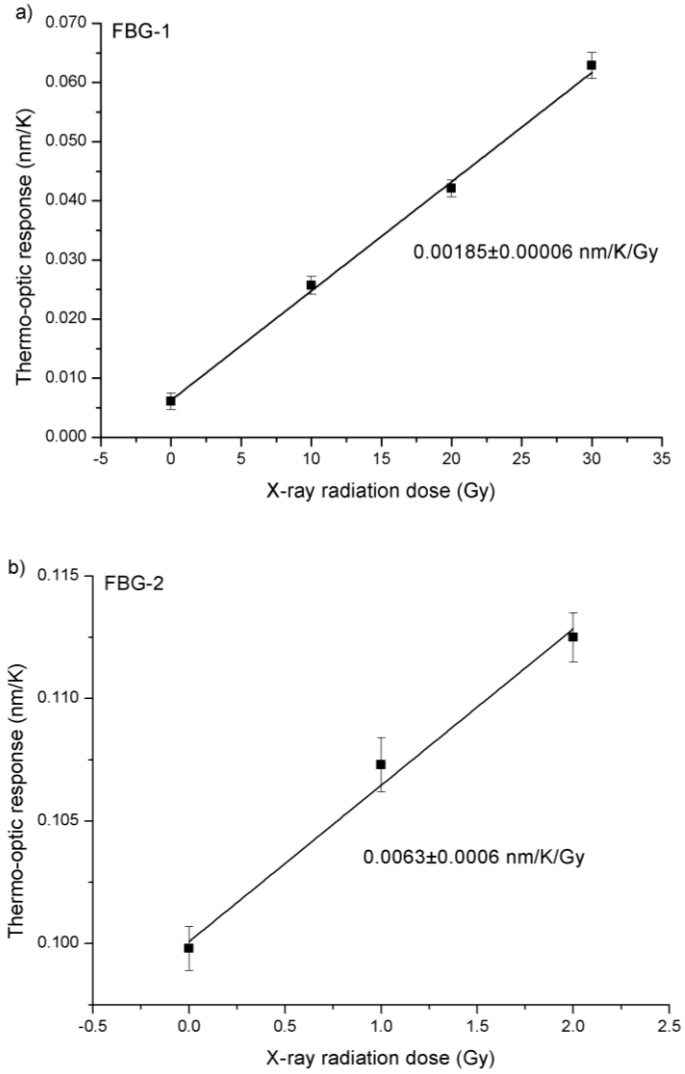

Figure 4.12. Thermo-optic responses as a function of the radiation dose for FBG-1 (a) and FBG-2 (b).

4.2.2 Ge-doped optical fibers inserted in resonant cavities

We investigate the effect of IR on germanosilicate optical fibers, that is, on a piece of Ge-doped fiber enclosed between two fiber Bragg gratings (FBGs). With respect to the previous FBG-based IR dosimeters, here the sensor is only the bare fiber without any special internal structure as shown in Figure 4.13.

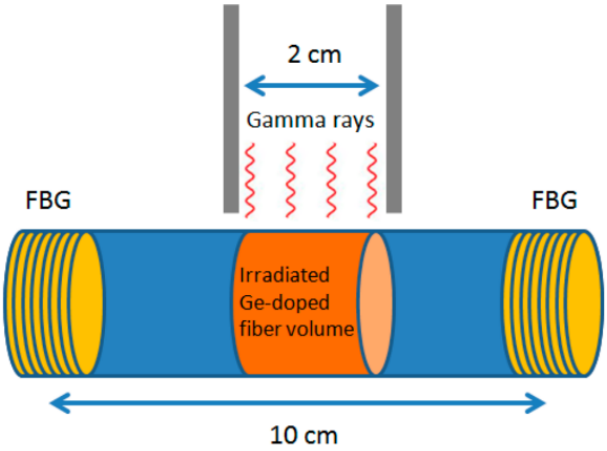

Figure 4.13. Irradiation of a Ge-doped optical fiber enclosed between two FBGs with gamma rays from a 6 MV clinical linear accelerator.

The fiber thermo-optic response was measured before irradiation and after exposure to gamma rays with consecutive doses of 5 Gy, 10 Gy and 20 Gy.

Figure 4.13a shows a graph of the cavity mode wavelength as function of the fiber temperature before irradiation. The data points are well approximated by a line whose angular coefficient m is the cavity thermo-optic coefficient. From a linear fit of the curve we obtained:

$$m = 0.0183 \pm 2 \times 10^{-4}\ \text{nm/K}$$

Figures 4.14b–d show the thermo-optic response measured after each dose, where a dependence of the slope of the curves on the dose is evident.

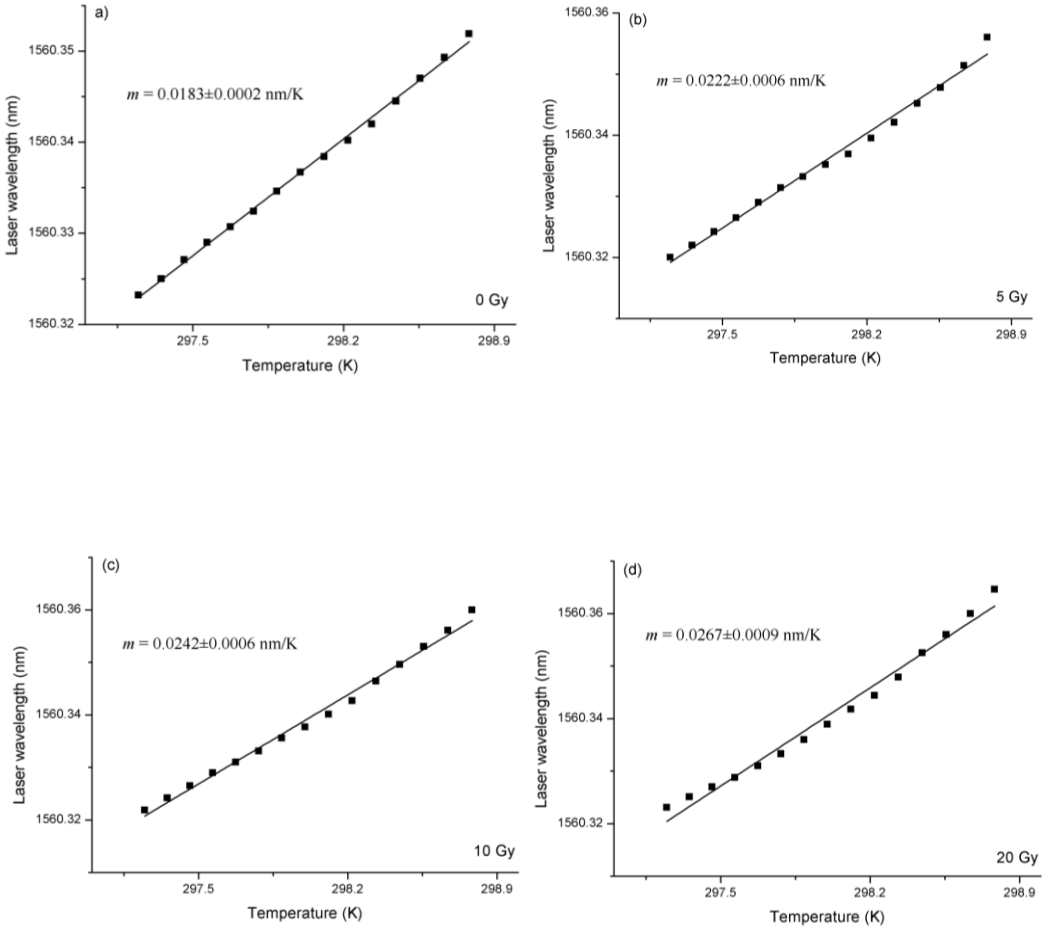

Figure 4.14. Wavelength of the laser locked to a cavity mode as function of the fiber temperature before irradiation (a) and after exposure to consecutive doses of 5 Gy, 10 Gy and 20 Gy (b–d). By a linear fit of the curves, we obtain the thermo-optic coefficient for each dose[137].

The thermo-optic response for doses of 5 Gy, 10 Gy and 20 Gy were presented in Table 4.2.

Table 4.2. Thermo-optic response for 5, 10 and 20 Gy dose irradiation and Standard Error (SE).

Dose (Gy)	Thermo-optic response ± SE (nm/K)
5	0.0222 ± 0.0006
10	0.0242 ± 0.0006
20	0.0267 ± 0.0009

In Figure 4.15, the value of the thermo-optic response *versus* the dose delivered to the fiber is plotted. The curve exhibits an exponential behavior, showing the beginning of sensor saturation for doses above 10 Gy. From a single exponential fit, we obtained a saturation constant of about 9.6 Gy. Approximating the start of

the exponential curve with a straight line, we obtained a linear trend with an angular coefficient of 0.0011 nm/K/Gy.

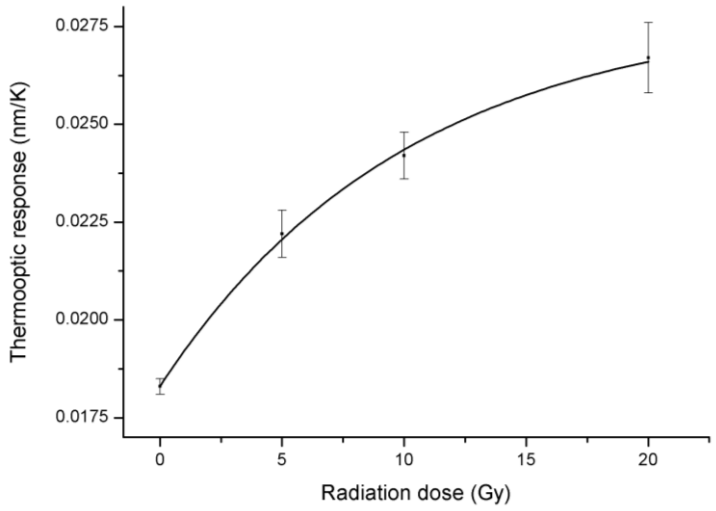

Figure 4.15. Thermo-optic response versus the dose delivered to the fiber. Saturation of the sensor response starts for doses higher than 10 Gy [137].

Dividing this coefficient by the average value of the uncertainty on the single measurement of the thermo-optic response (0.0004 nm/K) we obtained a final detection limit of 360 mGy.

4.3 The portable unit design

Before considering a new dosimeter technology, it is necessary to demonstrate that it provides reliable performance under clinical conditions. Indeed once the characterization of effects of ionizing radiation on FBGs and in-fiber resonators as a function of dose have been performed, the interrogation setup is developed selecting properly-doped fiber sensors.

The upgrade of the investigation consisted in developing a laser-based interrogation set up for active tracking of FBG and/or fiber resonator peaks in real-time dose measurements. Furthermore, the electronics and the optical equipment have been made as compact as possible via a deep optimization and engineering process. The interrogation setup was designed in a usable clinic dosimeter as shown in Figure 4.16.

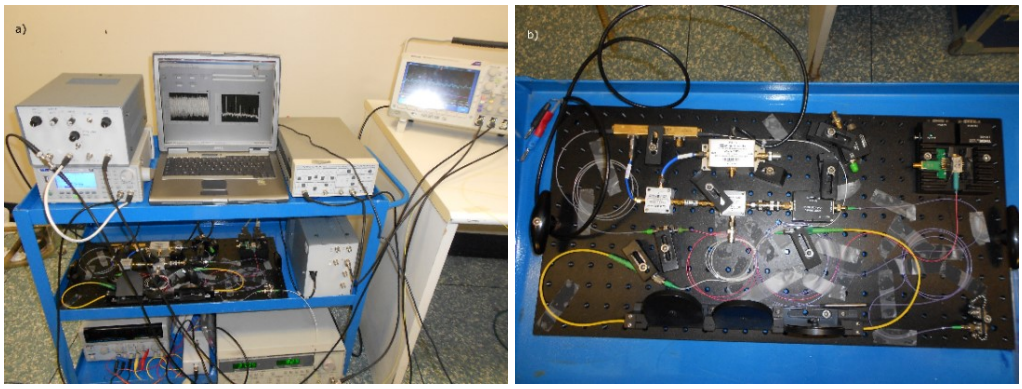

Figure 4.16. Pictures of the portable reading unit (a) with a zoom on the optic bank (b).

4.4 LiF:Mg,Ti (TLD-100) response to photon beam and high dose-per-pulse electron beam

Purpose of the experiment was to investigate thermoluminescent dosimeters (TLDs) response to intraoperative electron radiation therapy (IOERT) beams. In an IOERT treatment, a large single radiation dose is delivered with a high dose-per-pulse electron beam (2 – 12 cGy/pulse) during surgery.

LiF:Mg,Ti dosimeters (TLD-100) were irradiated with different IOERT electron beam energies (5, 7 and 9 MeV) and with a 6 MV conventional photon beam. For each energy, the TLDs were irradiated in the dose range of 0 – 10 Gy in step of 2Gy. Regression analysis was performed to establish the response variation of thermoluminescent signals with dose and energy.

4.4.1 Individual calibration of the thermoluminescent dosimeters

TLDs were individually identified by a code and as first step irradiated in the same geometrical conditions to obtain the individual sensitivity (see Eq. (3.1)). Any dosimeter with a relative sensitivity value greater that ± 10% of the mean value has been rejected. TLDs were placed at source source-to-axis distance (SAD) of 100 cm, at a depth of 5 cm in the equivalent water phantom and irradiated with a beam size of 10 x 10 cm^2 and a total dose of 2 Gy (Figure 4.17). As in the previous fiber's experiment before the irradiation, the beam output of the linac was verified, besides ionization chamber measurements were performed during any TLDs irradiation experiment to check the accuracy of the delivered dose (Figure 4.18).

The individual sensitivity correction factor for all forty TLDs are shown in Figure 4.19.

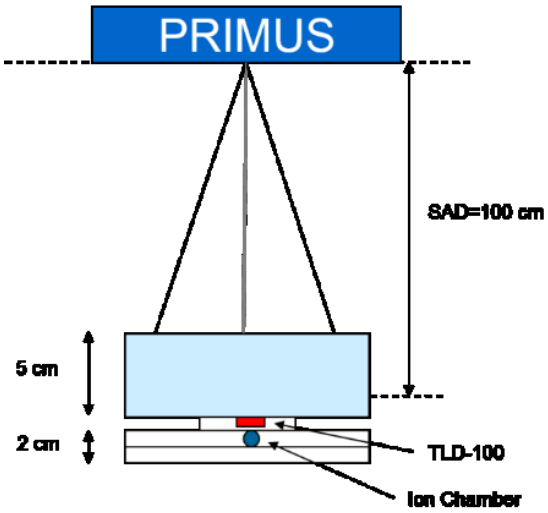

Figure 4.17. Experimental set up used to irradiate the TLDs with the 6 MV photon beam of clinic linear accelerator Primus Siemens.

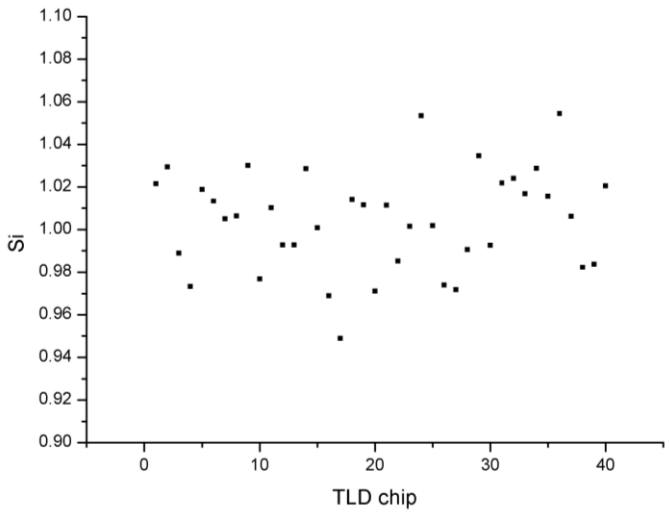

Figure 4.18. Individual sensitivity correction factor for all forty TLDs.

The S_i values range between 0.95 and 1.05. All values were included in the range of ± 10% of mean value, and none of TLDs was rejected.

To have a back-up measurements of the delivered dose, 2 MOSFETs were calibrated in the configuration set up illustrated in Figure 4.19 and the measures of the ionization chamber were recovered.

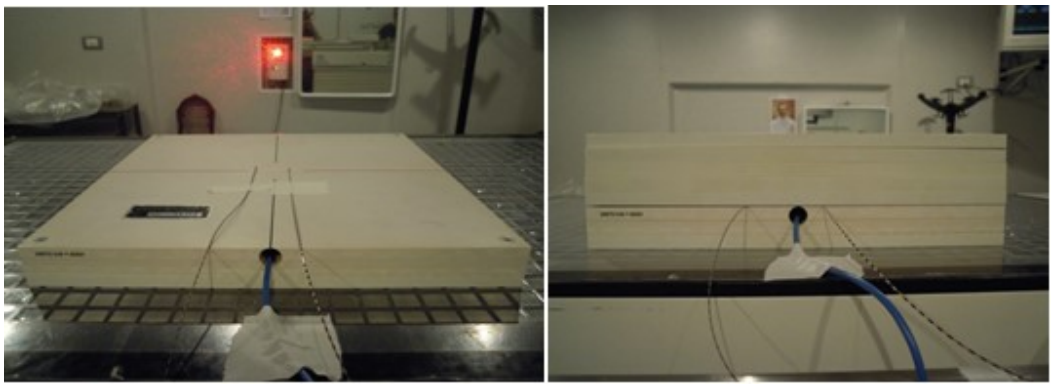

Figure 4.19. Configuration set up for the determination of MOSFETs calibration. The MOSFETs were fixed at 5 cm of depth in the PMMA phantom. The blue cable is the Farmer chamber, type 30001.

The absorbed dose calculated by the TPS at 5 cm of depth in the PMMA phantom was 94.8 cGy and so the calibration factors for the two MOSFETs resulted:

$$F_{C_1} = 3.0 \pm 0.9 \ \frac{mV}{cGy}$$

$$F_{C_2} = 3.0 \pm 1.3 \ \frac{mV}{cGy}$$

4.4.2 Irradiation of the TLDs

Groups of 9 TLDs were housed in a cavity on purpose shaped in a slab of plexiglass and inserted in the equivalent water phantom (Figure 4.20). As a first step, the TLDs were irradiated with 6 MV photon beam. The irradiation was performed with the same experimental setup and procedure described for TLDs calibration.

Each group was irradiated with a single dose value between 2 and 10 Gy in steps of 2Gy. In each measurement session, a group of 9 TLDs was not irradiated to measure the background signal. Measurements from single TLD were corrected for the corresponding Si value.

Before each set of irradiation with different electron beam energy, the beam output (Gy/UM) was verified using an Advanced Markus chamber type (PTW type 34045, Freiburg, Germany) according to the protocol previously described in [104].

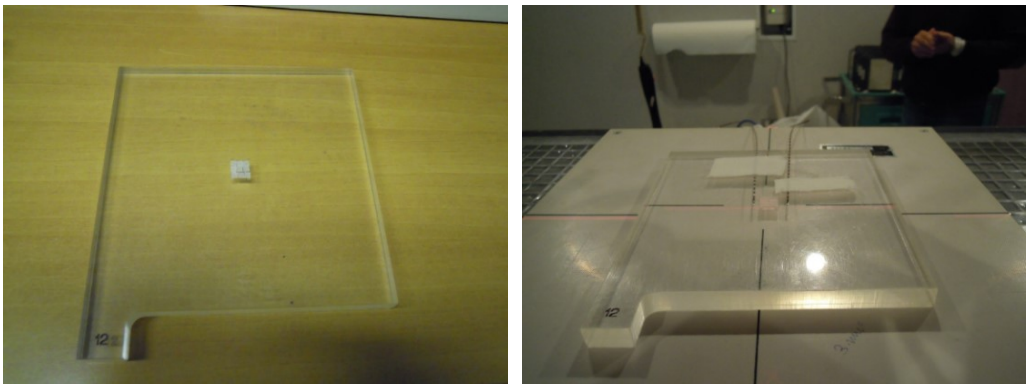

Figure 4.20: Cavity shaped in a slab of plexiglass (on the left) and configuration set up of irradiation of the TLDs with MOSFETs and ionization chamber before putting PMMA slab phantom above (on the right).

After the TLDs were irradiated with the electron beams (5 – 7 - 9 MeV) produced by Novac7. The TLDs were irradiated at the depth of maximum dose of each electron energy (Table 4.3).

Ionization chamber measurements were performed during any TLDs irradiation experiment to check the accuracy of the delivered dose (Figure 4.21).

Table 4.3. Electron beams characteristics.

Energy (MeV)	Applicator (mm)	Dose-per-pulse (cGy/pulse)	R_{max} (mm)
5	100	2.6	8
7	100	2.7	11
9	100	3.1	13

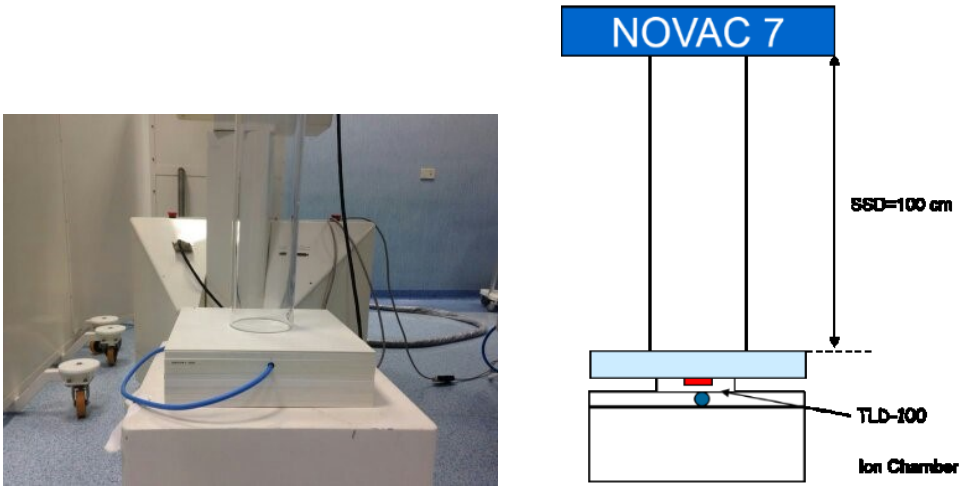

Figure 4.21. Experimental setup used to irradiate the TLDs with the 5, 7 and 9 MeV electron beams of intra-operative linear accelerator Novac7.

For each dose-energy measurements, the mean response and standard error for the TLD's group were calculated. For all beams, regression analysis was performed on TLD response as a function of delivered doses.

The goodness of the fit was evaluated by the R^2 coefficient. To identify the model that best fits the experimental data the F-test was applied. A *p* value less than 0.05 was considered statistically significant. Statistical analysis was performed with MedCalc (MedCalc Software bvba, Ostend, Belgium) and OriginLab (OriginLab Corporation, Northampton, Massachusetts).

The dose-response of TLDs for 6 MV photon beam was depicted in Figure 4.22. The results from regression analysis show very high R^2 values for both linear and the quadratic models (respectively, R^2 = 0.9995 and R^2 = 0.9997). The F-test approved the linear model has the best model (p = 0.169).

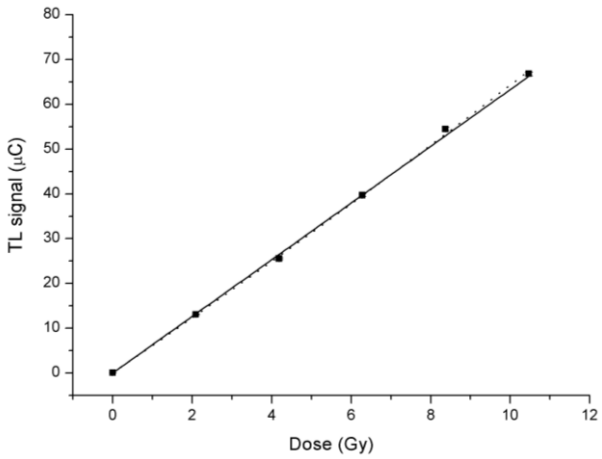

Figure 4.22. TLDs dose–response curve for doses between 0 Gy e 10 Gy at 6 MV photon beam. The solid line represents the linear fit, the dot line the polynomial fit [138].

The TLD dose-response at 5 MeV electrons was depicted in Figure 4.23a. The linear model has an R^2 = 0.974 while the quadratic model has an R^2 = 0.999. For the 7 MeV and 9 MeV electron beams (Figure 4.23b-c) the R^2 coefficients were 0.994 and 0.996 for the linear models and 1.0 and 0.999 for the quadratic models, respectively.

The quadratic fit for electron beams were illustrate on the same graph in Figure 4.23d for comparison.

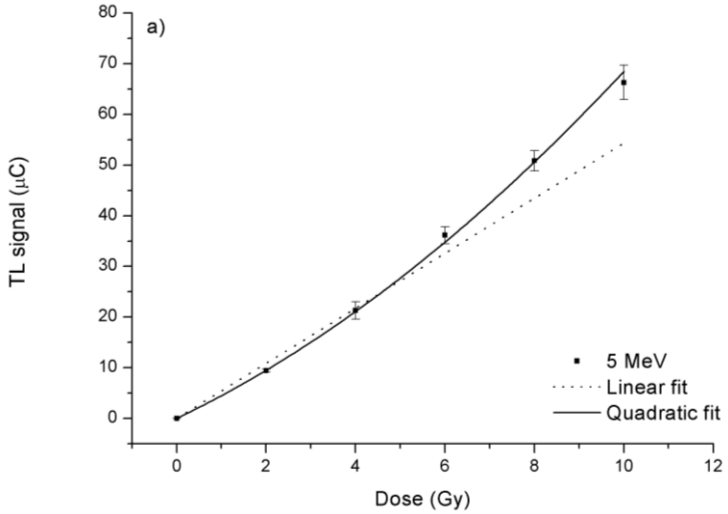
a)
TL signal (μC)
Dose (Gy)
5 MeV
Linear fit
Quadratic fit

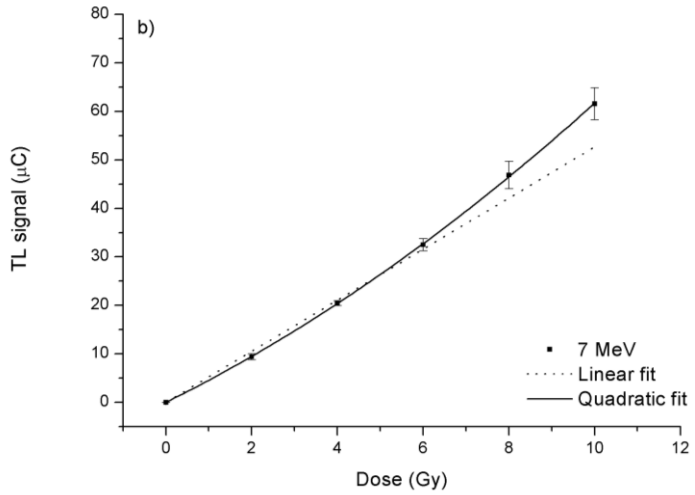
b)
TL signal (μC)
Dose (Gy)
7 MeV
Linear fit
Quadratic fit

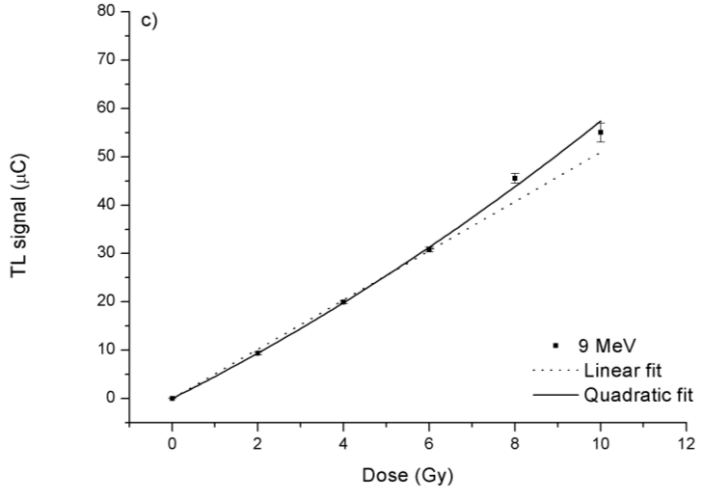
c)
TL signal (μC)
Dose (Gy)
9 MeV
Linear fit
Quadratic fit

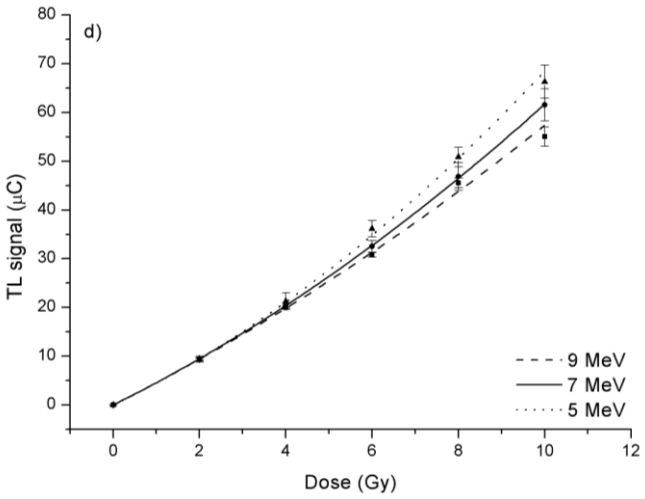

Figure 4.23. TLDs dose–response curve for doses between 0 Gy e 10 Gy at a) 5 MeV electron beam, b) 7 MeV electron beam, and c) 9 MeV electron beam. The dot lines represent the linear fit, the solid lines represent the quadratic fit. In d) the comparison between all curves is reported. The dot line represents the quadratic fit of 5 MeV, the solid line the quadratic fit of 7 MeV and the dash line the quadratic fit of 9 MeV [138].

The best-fit regression coefficients for photon and electron beams were reported in Table 4.4.

Table 4.4. Photon and electron beams best-fit regression coefficients for the dose-response models [138].

Model	Linear				Quadratic			
Equation	$y = A + B_1 D$				$y = A + B_1 D + B_2 D^2$			
Energy		Coefficient	SE	Adj. R^2		Coefficient	SE	Adj. R^2
6 MV	A	9.77E-4	9.93E-6	0.9995	A	9.77E-4	9.93E-6	0.9996
	B_1 (Gy^{-1})	6.33	0.02		B_1 (Gy^{-1})	6.09	0.05	
					B_2 (Gy^{-2})	0.03	0.01	
5 MeV	A	0.002	2.39E-04	0.9744	A	0.002	2.39E-4	0.9992
	B_1 (Gy^{-1})	5.43	0.11		B_1 (Gy^{-1})	4.23	0.19	
					B_2 (Gy^{-2})	0.26	0.03	
7 MeV	A	0.002	2.39E-04	0.9937	A	0.002	2.39E-4	0.9999
	B_1 (Gy^{-1})	5.27	0.09		B_1 (Gy^{-1})	4.38	0.24	
					B_2 (Gy^{-2})	0.18	0.05	
9 MeV	A	8.37E-4	1.33E-04	0.9962	A	8.37E-4	3.4E-06	0.9993
	B_1 (Gy^{-1})	5.09	0.04		B_1 (Gy^{-1})	4.44	0.11	
					B_2 (Gy^{-2})	0.13	0.02	

Part II

NTCP modelling

4.5 Multivariate and classical normal tissue complication probability modeling

The predictive models derived by an optimization process will be presented in the present section, for different patient cohorts and outcomes. Table 4.5 shows an overview on the multivariable NTCP models, described in detail below.

Table 4.5. Implemented multivariable (MV) NTCP models. N is the number of patient included in the patient cohort, n identifies the number of patients that developed complications.

Outcome	Patient cohort (n/N)	MV Model
GI toxicity (RTOG G1-2)	Prostate (21/84)	3-variable: V_{65}, Acute GI* tox, antihypertensive/anticoagulants
Severe Acute Skin toxicity (RTOG G3 vs. G0-2)	Breast (11/140)	2-variable: S_{30}†, psoriasis
Hypothyroidism	HL‡ (22/53)	3-variable: V_{30}(cc)¶, thyroid volume, gender
Valvular heart damage	HL (27/90)	3-variable heart + lung variables
Lung fibrosis	HL (18/115)	3-variable: 2 competing models: heart + lung variables

‡HL=Hodgkin Lymphoma.
*GI=gastrointestinal.
†S_{30}=relative skin surface receiving at least 30 Gy.
¶V_{30} (cc)=absolute thyroid volume receiving at least 30 Gy.

4.5.1 Radiation-induced hypothyroidism

Fifty-three patients treated with sequential chemo-radiotherapy for Hodgkin's lymphoma (HL) at the Radiation Oncology department of the University "Federico II" of Naples, were retrospectively reviewed for radiation-induced hypothyroidism (RHT) events. Clinical information along with thyroid gland dose distribution parameters were collected and their correlation to RHT was analyzed by Spearman's rank correlation coefficient (R_s).

A total median dose of 32 Gy (range 30 – 36 Gy) in 20 daily fractions of 1.5 – 1.8 Gy was planned.

The thyroid gland volume, the minimum (D_{min}), maximum (D_{max}) and mean doses (D_{mean}), the absolute volume of thyroid and the percentage of thyroid volume exceeding 10, 20 and 30 Gy (V_x (cc) and V_x (%), respectively) were calculated from the dose volume histograms. In addition, the "residual X Gy thyroid volume", defined as the difference between the thyroid gland volume and V_x (cc), was calculated.

We separately analyzed two sets of candidate predictors: set 1 includes the clinical variables, plus D_{min}, D_{max}, D_{mean} and V_x (%), and set 2 includes the same variables as set 1 but V_x was expressed as absolute volume, V_x (cc).

The cross-correlation matrixes for the variables belonging to set 1 and set 2, respectively, are shown in Figures 4.24a-b. For both set of variables, a strong multiple correlation (i.e. $R_s > 0.85$) between dosimetric parameters was found.

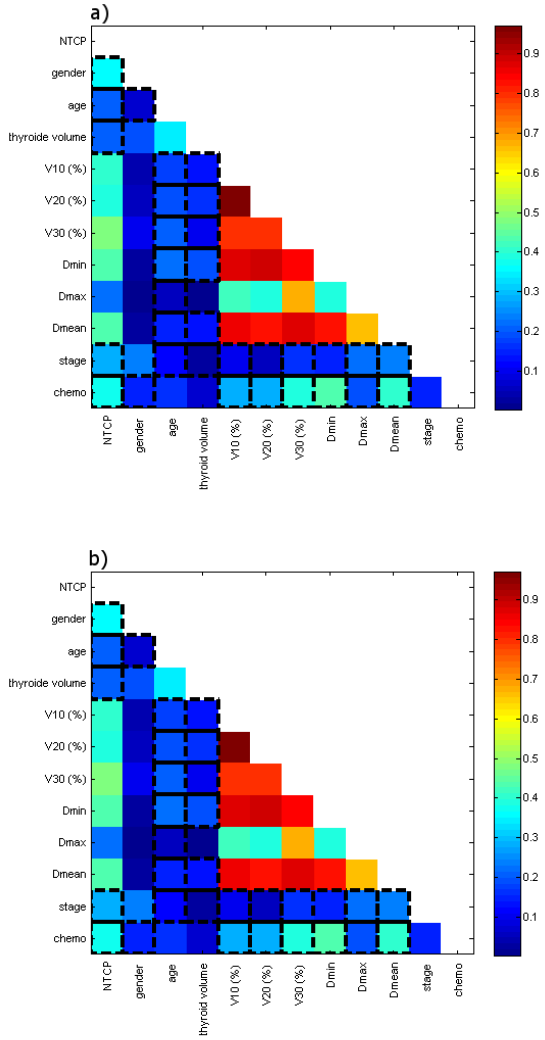

Figure 4.24. The cross-correlation matrixes for the variables belonging to set 1 (a) and to set 2 (b). The colorbar represents the Spearman's rank correlation coefficient value. NTCP: normal tissue complication probability, V_x (%): percentage of thyroid volume exceeding X Gy; V_x (cc): absolute thyroid volume exceeding X Gy [139].

After applying the selection criteria to avoid overfitting to set 1, V_{30} (%) and D_{max} resulted to be the dosimetric parameters that should be included in the multivariate analysis along with clinical variables. Similarly, for set 2, V_{30} (cc), D_{max} e D_{mean} were selected along with clinical variables.

In set 1, a two-variable model was suggested as the optimal order by bootstrap method. Figure 4.25a shows the five most frequently selected models within the bootstrapped subpopulations. The optimal model ($R_s = 0.615$, $p < 0.001$) includes gender (female = 0, male = 1) and V_{30} (%) (model 1). According to this model, the risk of RHT increases as V_{30} (%) increases, and it is higher for female patients. Conversely, in set 2, a three-variable model was suggested as the optimal order by

bootstrap method. Figure 4.25b shows the five most frequently selected models within the bootstrapped subpopulations.

The optimal model (R_s = 0.630, $p < 0.001$) includes gender, V_{30} (cc) and thyroid gland volume (model 2). The best-fitted regression coefficients for the two models are given in Table 4.6. As for model 1, the risk of RHT increases as V_{30} (cc) increases and it is higher for female patients; in addition the risk decreases with larger volume of thyroid gland. Model 2 NTCP surfaces for males and females are represented in Figure 4.26.

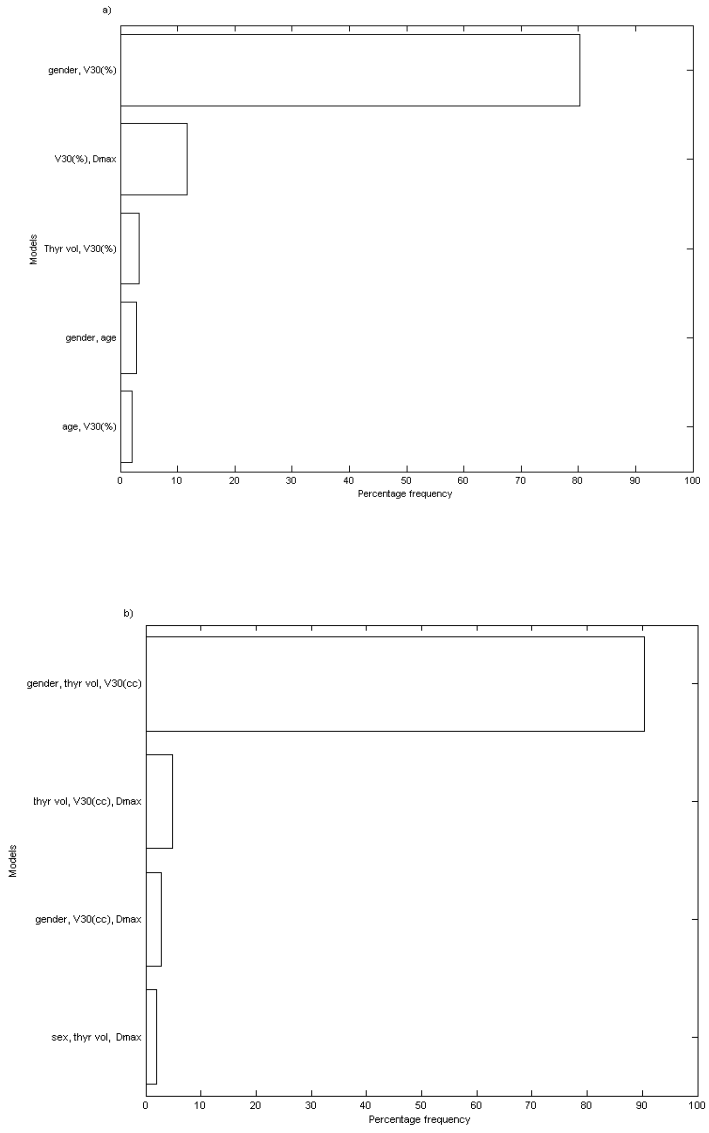

Figure 4.25. The five most frequently selected models by bootstrap sampling technique: (a) variable set 1; (b) variable set 2. NTCP: normal tissue complication probability, V_x(%): percentage of thyroid volume exceeding X Gy; V_x(cc): absolute thyroid volume exceeding X Gy [139].

Table 4.6. Best-fitted model parameters and 95% confidence intervals for model 1 and model 2.

	Parameter	Estimated coefficient	Std Error	p-value
Model 1				
	gender	-2.32	0.83	0.0062
	V_{30} (%)	0.0379	0.011	0.00093
	constant	-1.83		
Model 2				
	gender	-2.21	0.85	0.011
	V_{30} (cc)	0.265	0.09	0.0021
	thyroid volume (cc)	-0.268	0.11	0.011
	constant	1.94		

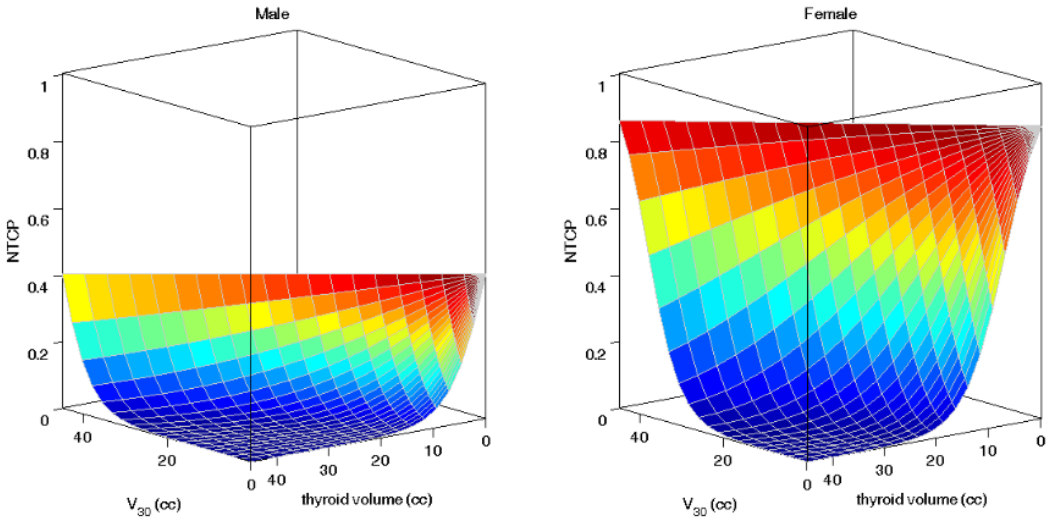

Figure 4.26. Model 2 NTCP surfaces for males and females as a function of V_{30} (cc) and thyroid volume (cc) [139].

The obtained models were then compared using the AUC (Table 4.10) of the ROC curves depicted in Figure 4.27a-b. As expected, no difference in performance was found between model 1 and model 2 ($p = 0.76$) for our cohort of patients (Figure 4.27a).

Applying model 1 and model 2 to the external case-control cohort of breast cancer patients [136], we obtained the ROC curves showed in Figure 4.27b. In this case, model 1 fails to predict RHT (AUC = 0.568. 95% CI 0.328 - 0.741) while model 2 has a high performance (AUC = 0.914. 95% CI 0.768 - 0.984). This result can be ascribed to the fact that, unlike our patients, the external cohort is characterized

by large inter-individuals and inter-groups variation in thyroid volumes. Therefore the model 2, where V_{30} is expressed as absolute volume coupled with the thyroid volume, results to be more effective in RHT prediction.

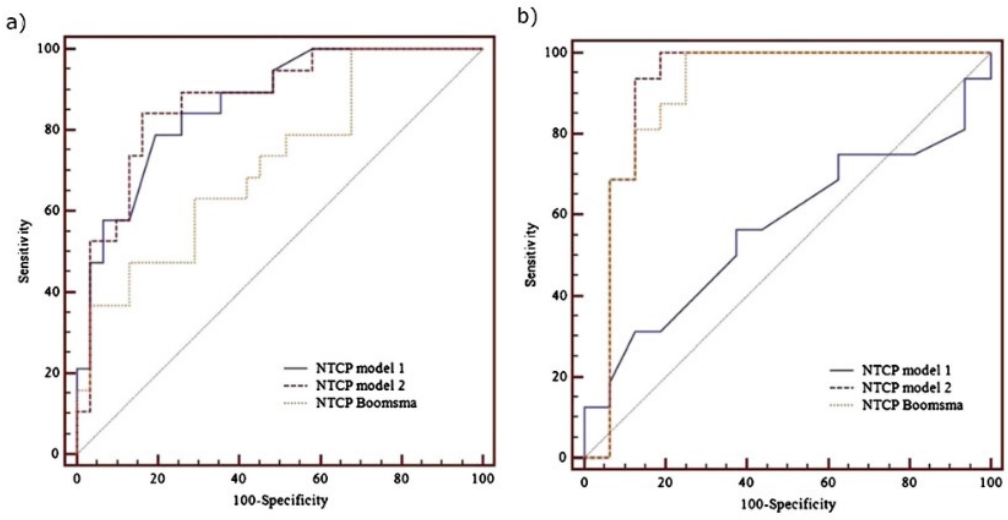

Figure 4.27. ROC curves for model 1, model 2, and Boomsma model [140]: (a) on Hodgkin's lymphoma dataset (b) on external breast cancer dataset.

4.5.2 Gastrointestinal toxicity after external beam radiotherapy for localized prostate cancer

Data on 57 consecutive patients with localized prostate adenocarcinoma treated with radiation therapy at the Radiation Oncology department of the University "Federico II" of Naples were retrospectively reviewed. All clinical information as cardiac comorbidities, diabetes, previous abdominal surgery, smoking history, hormonal therapy, and drugs prescription were retrieved from medical records.

A total dose of 66 Gy to seminal vesicles and 76 Gy to the prostate gland with daily fractions of 2 Gy (5 times per week) was planned.

Rectum dosimetric parameters were extracted from the dose-volume histograms (DVH) for modeling. Dosimetric parameters included: the maximum (D_{max}) and mean doses (D_{mean}), the percentage volume exceeding 20 - 75 Gy (V_x) in increment of 5 Gy.

Acute GI treatment toxicity (toxicity present during radiotherapy and in the first 3 months thereafter), and late GI toxicity (follow-up > 3 months) was evaluated by physicians according to Radiation Therapy Oncology Group/European

Organization for Research and Treatment of Cancer (RTOG/EORTC) criteria [139]. At a median follow-up of 30 months, 37% (21/57) patients developed acute grade ≤ 2 GI events while 33% (19/57) were diagnosed with grade ≤ 2 GI late events.

Figure 4.28a shows the cross-correlation matrix for clinical and dosimetric variables. A strong multiple correlation between dosimetric parameters was found. Accordingly, these highly correlated variables were not included in the multivariate analysis.

A three-variable model was suggested as the optimal order by bootstrap method. Figure 4.28b shows the five most frequently selected models within the bootstrapped subpopulations. The optimal model (*model 1*) includes V_{65}, antihypertensive and/or anticoagulant (AH/AC) drugs use and previous acute toxicity.

The Spearman's rank correlation coefficient of the model is 0.47 ($p < 0.001$) and the AUC of the corresponding ROC curve is 0.79. The best-fitted regression coefficients are given in Table 4.7. According to this model, the risk of late GI toxicity of grade G1 or G2 increases as V_{65} increases, it is higher for patients experiencing previous acute toxicity and it is lower for patients who take AH/AC drugs.

In Table 4.10 the regression coefficients for the logistic model based on V_{65} only (*model 2*) are also reported. The result of ROC analyses was a discrimination value for V_{65} of 29.3%.

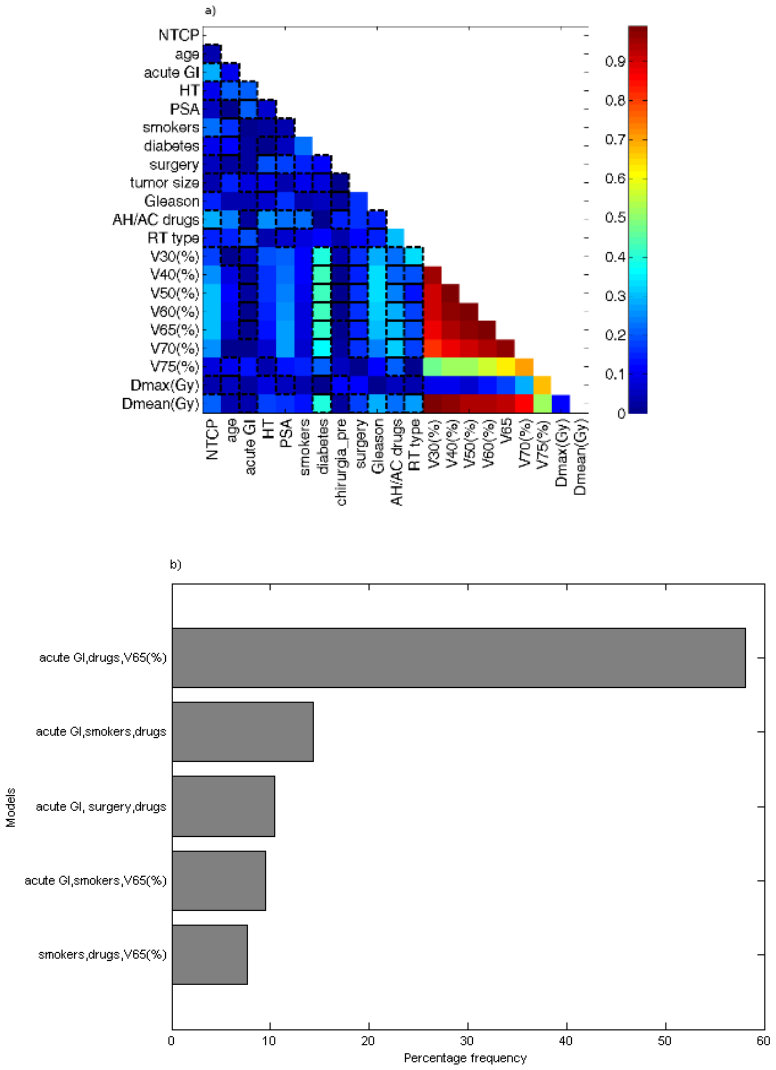

Figure 4.28. Cross-correlation matrix (a) and the five most frequently selected models by bootstrap sampling technique (b). The lateral bar represents the Spearman's rank correlation coefficient value. NTCP: normal tissue complication probability; HT: hormonal therapy; PSA: prostate specific antigen; AC/AH: antihypertensive/anticoagulants; RT: radiation therapy; V_x (%): percentage of rectum volume exceeding X Gy [141].

Table 4.7. Best-fitted regression coefficients for NTCP models and odds ratios[4] (OR).

Parameter	Estimated coefficient	SE	p-value	OR
Model 1				
V_{65} (%)	0.028	0.017	0.092	1.03
Antihypertensive/anticoagulants	-1.442	0.669	0.031	0.24
Acute GI toxicity	1.458	0.669	0.029	4.30
constant	-1.283			
Model 2				
V_{65} (%)	0.033	0.016	0.036	1.03
constant	-1.702			

In Figure 4.29 the comparison is reported among the ROC curves obtained applying *model 1*, *model 2* and LKB model. The AUC values were 0.79, 0.69 and 0.68, respectively. For the LKB model we used the parameters reported by Gulliford et al. [142] for GI toxicity of Grade 1 and Grade 2 for nonbleeding endpoints.

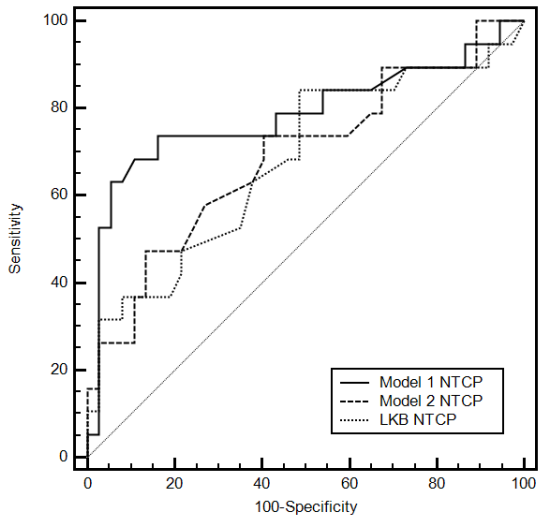

Figure 4.29. Comparison of receiver operator characteristic (ROC) curves obtained applying three-variable NTCP model (model 1), V_{65}-based NTCP model (model 2) and LKB NTCP model [37].

[4] Odds ratio: a measure of association between an exposure and an outcome. The OR represents the odds that an outcome will occur given a particular exposure, compared to the odds of the outcome occurring in the absence of that exposure.

Ninety-five percent confidence intervals for parameters estimates were obtained using the profile likelihood method [130]. Following this method, each parameter belonging to the set (D_{50}, m, n) was varied around its ML estimate (optimum LLH) while the other two parameters were fixed at their ML estimate.

The 95% confidence bounds were determined reducing the maximum LLH by one half of the χ^2 inverse cumulative distribution function associated to 95%, so as to obtain the iso-likelihood contours in each Cartesian plane of the parameters space (D_{50}, m, n).

In correspondence to the parameters values belonging to the iso-likelihood contours, a bundle of NTCP curves was calculated and the 95% confidence region for the model fit was thus estimated [21].

In order to perform an internal validation of the fitting results and to test the fit robustness, the bootstrap method was here employed to determine the spread in ML estimation of NTCP parameters. The bootstrap resampling method works by refitting the NTCP model using the ML estimation to many pseudo-datasets which are created by subsampling the input data set (20000 bootstrap resample runs with a number of folds of 80).

In the recent work [38] we extended the sample size with an additional dataset up to 84 patients in order to: 1) fit the LKB model deriving the parameters for specific rectal toxicity; 2) validate the multivariate model on an extended cohort of patients and compare its predictive power with the LKB model. Of 84 patients 25% (21/84) had developed acute GI toxicity while 36.9% (31/84) late GI toxicity. Among cases of late rectal morbidity, 31% (26/84) were G1 and 9.5% (8/84) were G2.

The optimal NTCP parameters values for LKB model resulted to be D_{50} = 87.3 Gy (95% CI 75.9 - 102.2 Gy), m = 0.37 (95% CI 0.26 - 0.64), n=0.10 (95% CI 0.02 - 0.26) and the corresponding value of log-likelihood is LLH=-46.3. Ninety-five percent confidence intervals for parameters estimates were obtained using the profile likelihood method: each parameter belonging to the set (D_{50}, m, n) was varied around its ML estimate (optimum LLH) while the other two parameters were fixed at their ML estimate.

The 95% confidence bounds were determined reducing the maximum LLH by one half of the χ^2 inverse cumulative distribution function associated to 95%, so as to obtain the iso-likelihood contours in each Cartesian plane of the parameters space (D_{50}, m, n).

In correspondence to the parameters values belonging to the iso-likelihood contours, a bundle of NTCP curves was calculated and the 95% confidence region for the model fit was thus estimated [143]. In order to perform an internal validation of the fitting results and to test the fit robustness, the bootstrap method was here employed to determine the spread in ML estimation of NTCP parameters. The bootstrap resampling method works by refitting the NTCP model using the ML estimation to many pseudo-datasets which are created by subsampling the input data set (20000 bootstrap resample runs with a number of folds of 80).

Figures 4.30a-c illustrate the iso-likelihood contours in each Cartesian plane of the parameters space (D_{50}, m, n). In Figure 4.30.d the bundle of NTCP curves corresponding to the 95% confidence interval region for the model fit is plotted. To test the fit robustness we performed a bootstrap method.

The mean and the standard deviation of LKB NTCP model parameters obtained for bootstrap samples are D_{50} = 87 Gy (SD = 6 Gy), m = 0.37 (SD = 0.08), n = 0.10 (SD = 0.03). The mean values of m and n parameters are close to the exact fit to the whole patient cohort. Accordingly to the multivariable model presented in [135], the risk of G1-2 late GI toxicity increased as V65 increased, and it was higher for patients experiencing previous acute toxicity and lower for patients taking antihypertensive and/or anticoagulant drugs. The model exhibited a good predictive performance (AUC = 0.79). When applied to the present extended dataset, the logistic NTCP performance is still good with an AUC value of 0.75 (95% CI 0.613 - 0.891).

For comparison, the ROC curves are showed in Figure 4.31 and AUC and R_s values of the multivariate logistic and LKB models are reported in Table 4.8.

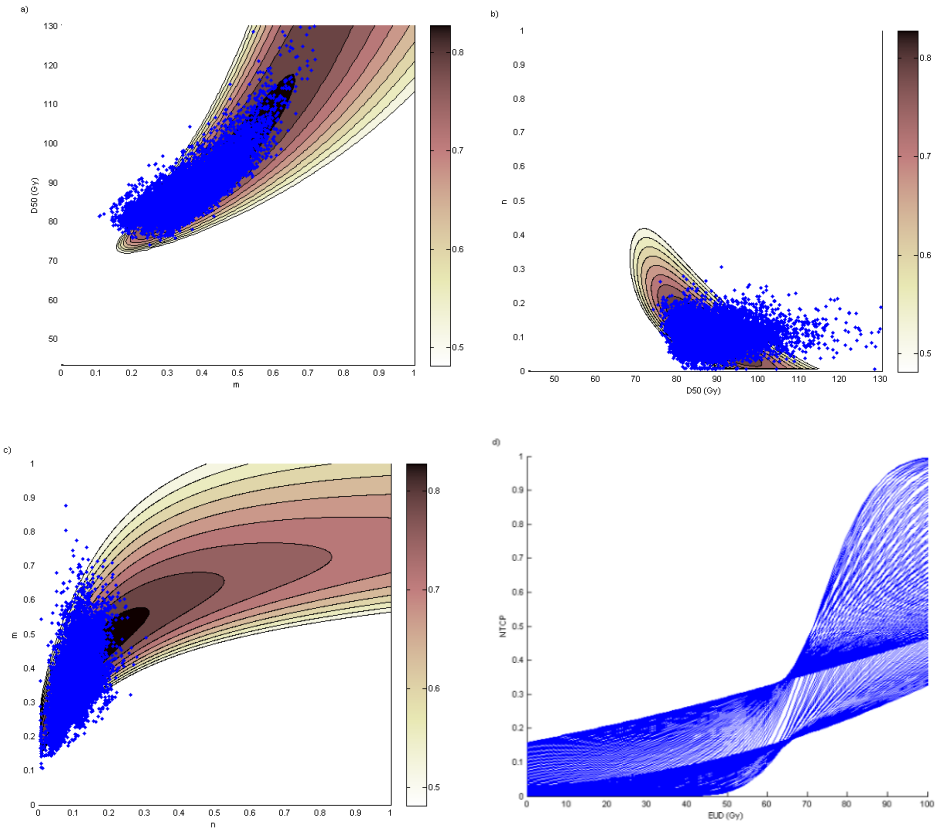

Figure 4.30. Likelihood estimation values plotted as a function of rectum LKB parameters. a) m and D_{50} for fixed value of n = 0.10; b) D_{50} and n for a fixed value of m = 0.37; c) n and m for a fixed value of D_{50} = 87.3 Gy; d) NTCP bundle curves showing 95% confidence interval region fit for the model. Blue points represent the results of bootstrap resample runs [141].

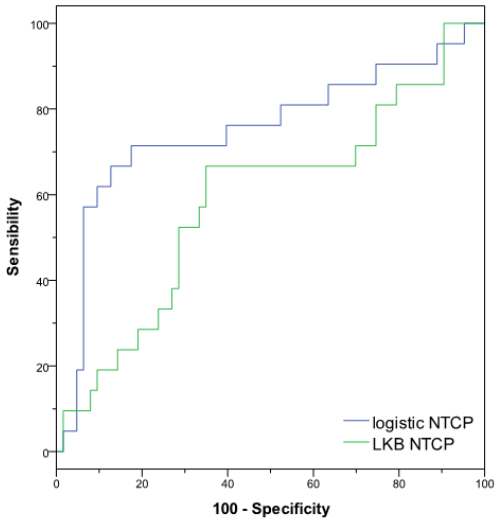

Figure 4.31. ROC comparison. Logistic regression model vs. LKB model for gastrointestinal toxicity [141].

Table 4.8. AUC values of ROC curves and Spearman's correlation coefficient (R_s) of LKB and logistic NTCP models with 95% confidence intervals.

Model	*AUC*	R_s
LKB	0.60 (0.442, 0.736)	0.133
Logistic	0.75 (0.613, 0.891)	0.378

4.5.3 Multivariate Normal Tissue Complication Probability Modeling of Heart Valve Dysfunction in Hodgkin Lymphoma Survivors

Fifty-six patients treated with sequential chemoradiation therapy for Hodgkin lymphoma (HL) were retrospectively reviewed for radiation-induced asymptomatic heart valvular defects (RVD).

A total median dose of 32 Gy (range, 30 - 36 Gy) in 20 daily fractions of 1.5-1.8 Gy was planned. Dosimetric parameters for heart, cardiac chambers, and total lung were extracted from the dose/volume histograms for modeling. Dosimetric parameters included the maximum (D_{max}) and mean (D_{mean}) doses and the percentage volume exceeding X Gy (V_x) in increments of 5 Gy. We corrected the dosimetric parameters for diverse dose fractions using an α/β ratio[5] of 2 for the cardiac structures and of 4 for the lung.

Figure 4.32a shows the cross-correlation matrices for representative variables for the whole heart and for each chamber. A 3-variable model was suggested as the optimal order by the bootstrap method. Figure 4.32b shows the 5 most frequently selected models within the bootstrapped subpopulations.

The optimal model ($R_s = 0.573$, $p < .001$) includes D_{max}, heart volume, and lung volume (model 1). According to this model, the NTCP for RVDs increases with D_{max} and with heart volumes, and it decreases with larger lung volumes.

The AUC was 0.83 (95% CI 0.71 - 0.92) and the discrimination value was 0.33.

[5] α/β ratio describes the curvature of a cell survival curve. It is the dose where cell killing due to the linear and quadratic components are equal. It enters in the definition of the biologically effective dose (BED) aimed to indicate quantitatively the biological effect of any radiotherapy treatment, taking account of changes in dose-per-fraction or dose rate and total dose.

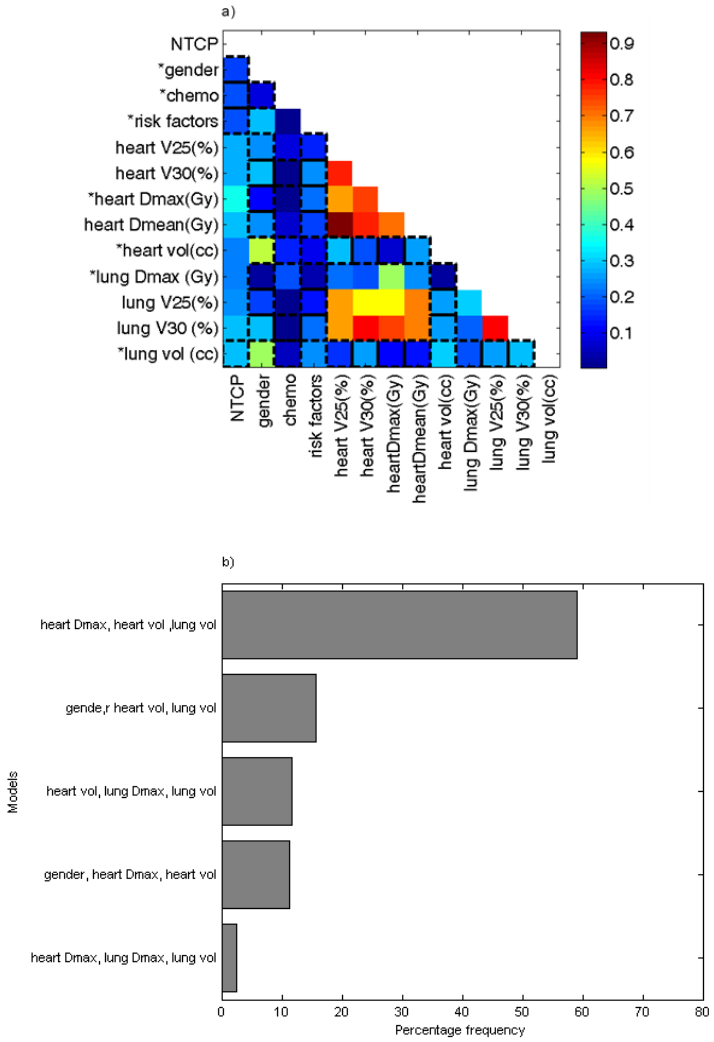

*Figure 4.32. (a) Whole heart cross-correlation matrix. (b) The 5 most frequently selected models by bootstrap sampling technique. Color bar represents the Spearman's rank correlation coefficient value. Black boxes represent negative correlation coefficient values. D_{ma} = maximum dose; NTCP = normal tissue complication probability; V_x (%) = percentage of volume exceeding X Gy. *Variables included in the multivariate analysis [143].*

With regard to the left chambers, by analyzing left-sided RVD, the optimal order model was again based on 3 variables. For both the atrium (model 2, R_s = 0.539, $p < .001$) and the ventricle (model 3, R_s = 0.557, $p < .001$), the best model includes the percentage volume exceeding 30 Gy (V_{30}), cardiac chamber volume, and lung. The best-fitted regression coefficients and the odds ratios (ORs) are given in Table 4.9.

The AUC for model 2 and model 3 were 0.84 (95% CI 0.71 - 0.92) and 0.82 (95% CI 0.70 - 0.91), with discrimination values of 0.22 and 0.20, respectively. There are no differences in the prediction capabilities of all 3 models ($z < 0.13$, $p > .89$).

Table 4.9. Best-fitted regression coefficients for NTCP models and odds ratios for the heart (model 1), the left atrium (model 2), and the left ventricle (model 3).

Model	Parameter	Estimated coefficient	SE	p value	OR
Model 1					
	Dmax (Gy)	0.1430	0.0751	.043	1.150
	Heart volume (cc)	0.0095	0.0036	.020	1.010
	Lung volume (cc)	-0.0017	0.0006	.011	0.998
	constant	-5.65			
Model 2					
	Left atrium V_{30} (%)	0.0219	0.0086	.011	1.022
	Left atrium volume (cc)	0.0871	0.0363	.016	1.091
	Lung volume (cc)	-0.0016	0.0006	.028	0.998
	constant	-3.58			
Model 3					
	Left ventricle V_{30} (%)	0.0346	0.0152	.023	1.035
	Left ventricle volume (cc)	0.0366	0.0131	.009	1.037
	Lung volume (cc)	-0.0018	0.0006	.005	0.998
	Constant	-2.26			

The models' NTCP surfaces for the whole heart, the left atrium, and the left ventricle are represented in Figure 4.33.

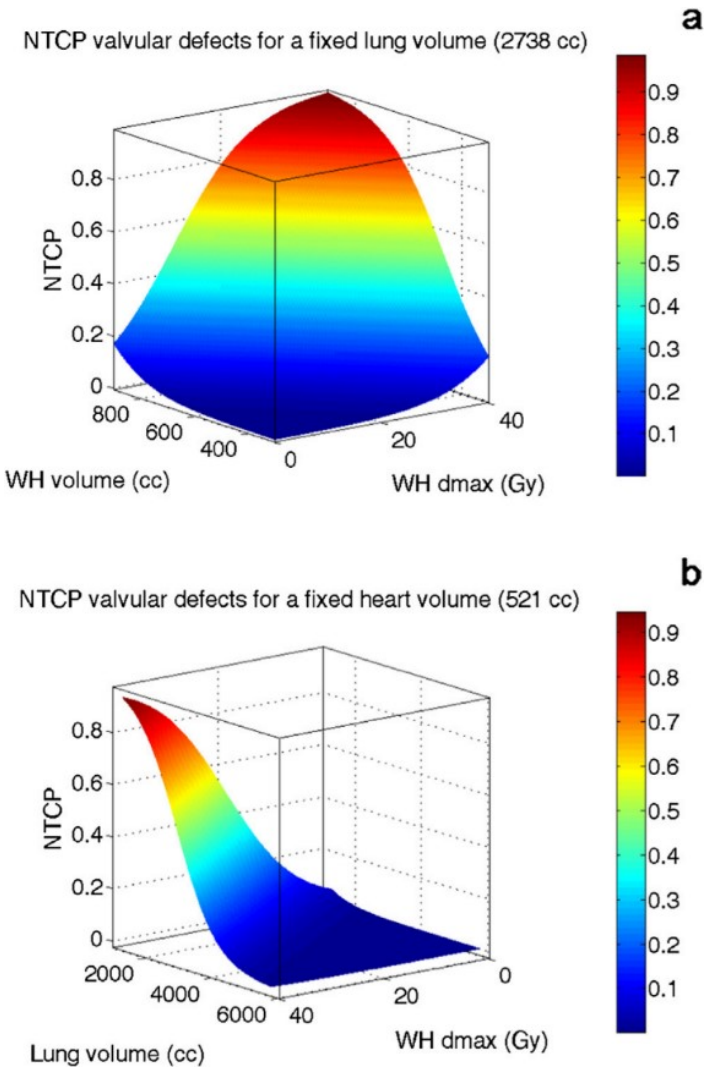

Figure 4.33. Whole heart (WH) normal tissue complication probability (NTCP) surfaces as a function of maximum dose (D_{max}) and heart volume (a) or lung volume (b) [143].

Successively we extended the patient data set up to 90 to test the predictive power of traditional LKB and the RS NTCP models for the induction of asymptomatic RVDs using.

We proceed by fitting the NTCP model parameters first from heart dose-volume parameters, and separately lung dose-volume parameters (Table 4.10). The mean and standard deviations of LKB and RS NTCP model parameters obtained with maximum likelihood estimation for bootstrap samples are shown in Table 4.11.

Table 4.10. Parameters estimates and 95% confidence intervals of LKB and RS NTCP models for heart and lung DVHs fitting. For each model the Spearman's correlation coefficient (R_s), the area under the receiver operator characteristic curve (AUC) and the log-likelihood (LLH) values are provided.

LKB	*D_{50} (Gy)*	*m*	*n*	*R_s*	*AUC*	*LLH*
heart	32.8	0.66	0.16	0.27	0.67	-51.6
	(25.9, 44.7)	(0.41, 1)	(0.10, 0.89)		(0.56, 0.78)	
lung	33.2	0.19	0.01	0.28	0.69	-49.7
	(31.3-35.5)	(0.13-0.32)	(0.01-0.03)		(0.58, 0.78)	
RS	*D_{50} (Gy)*	*γ*	*s*	*R_s*	*AUC*	*LLH*
heart	32.4	0.42	0.99	0.25	0.66	-52.3
	(22.7, 48.5)	(0.24, 0.62)	(0.0-1.0)		(0.55-0.76)	
lung	24.4	2.12	0.99	0.26	0.66	-51.1
	(22.3, 26.7)	(0.3-3.8)	(0.67-1.0)		(0.55-0.76)	

Table 4.11. Summary of mean and standard deviations of LKB and RS NTCP model parameters obtained with maximum likelihood estimation for bootstrap samples.

LKB	*D_{50} (Gy)*	*SD (Gy)*	*m*	*SD*	*n*	*SD*
heart	36.1	5.5	0.67	0.11	0.11	0.12
lung	33.9	1.4	0.22	0.03	0.01	0.02
RS	*D_{50} (Gy)*	*SD (Gy)*	*γ*	*SD*	*s*	*SD*
heart	32.7	3.1	0.43	0.07	0.99	0.06
lung	24.3	0.83	2.16	0.56	0.99	0.04

It's interesting to note that, independently of the organ chosen as the model input, namely heart DVHs or lung DVHs, we obtain similar prediction performances. Of note, we observed a serial behavior of the lung when using heart toxicity as endpoint. This result is different from the generally accepted parallel architecture, with a large volume effect, of the lungs when NTCP models were fit to radiation pneumonitis as endpoint. As a consequence, we can hypothesize a different mechanism of damage and a different contribution of lung irradiation to the heart toxicity potentially due to the difference in patho-physiology, although still unknown.

Given the good results obtained by applying the LKB model to lung DVHs we exploited the influence of combined heart-lung irradiation on RVD performing a multivariate logistic regression modeling with the least absolute shrinkage and selection operator (LASSO). In addition to heart irradiation factors, clinical variables, along with left and right lung dose-volume histogram statistics, were

included in the analysis. Prognostic factors frequently selected (more than 100/500 model fits) by LASSO, included mainly heart and left lung dosimetric variables along with their volume variables. The averaged cross-validated performance was AUC-Cross Validation = 0.685 and R_s = 0.293. The overall performance of a final NTCP model for RVD obtained applying LASSO logistic regression to the full dataset was satisfactory (AUC = 0.84, R_s = 0.55, $p < 0.001$).

Interestingly, applying LASSO, we showed, the importance of jointly considering left lung irradiation and left lung volume size in the prediction of subclinical radiation-related heart disease resulting in RVD [144].

4.5.4 Modeling the risk of radiation-induced lung fibrosis: irradiated heart tissue is as important as irradiated lung

The results reported in the previous section assessed the importance of lung irradiation in the development of heart damage. At this point, naturally, we through to investigate the mutual interaction of the two organs in the radiation induced complications [30, 145].

In the present study clinical and dosimetric records of 148 HL patients from an inter-institutional dataset (117 patients treated at University Federico II of Naples and 31 patients at S. Camillo-Forlanini Hospital in Rome) were retrospectively reviewed. Baseline and follow-up evaluations consisted of history and physical examination along with periodic total body CT scans. A diagnosis of RILF was based on the presence of radiological lung density changes evaluated on follow-up CT scans using the planning CT as baseline comparison. Fourteen out of 148 (9.5%) patients had lung disease at baseline. Thirteen out of 148 (8.8%) experienced toxicity after CHT but before the beginning of RT. We excluded these patients from further evaluations. Six patients were further excluded from analysis because dose maps were not available. Finally 115 patients resulted eligible. DVH and dose-mass-histogramm[6] (DMH) metrics were extracted for modeling: the minimum dose to x% highest dose volume (D_x); the percentage volume or mass receiving at least x dose (V_x or M_x); the absolute volume or mass receiving at least x dose (AV_x or AM_x).

[6] Dose–mass histogram is an important tool for evaluation of treatment plans for organs with variable densities. It describes better the dose distribution delivered to lung since its shape does not change during the breathing cycle.

At a median time of 13 months (range 9 - 83), 18/115 patients (15.6%) developed radiological changes on CT (i.e. any grade of RILF). Nine patients were symptomatic: 4 patients were diagnosed with severe symptomatic fibrosis showing dense radiographic changes (Grade 3), 5 cases developed grade 2 RILF (two slight radiological changes with severe cough and three moderate symptomatic fibrosis with patchy radiographic appearances). Nine patients developed slight CT radiological changes without symptoms (Grade 1).

DMHs and DVHs were generated for all patients and all analyzed organs. As expected, there is a well-marked difference between the DMH and DVH of a heterogeneous organ such as the lung compared with a slight difference observed for the heart (Figures 4.34a-d).

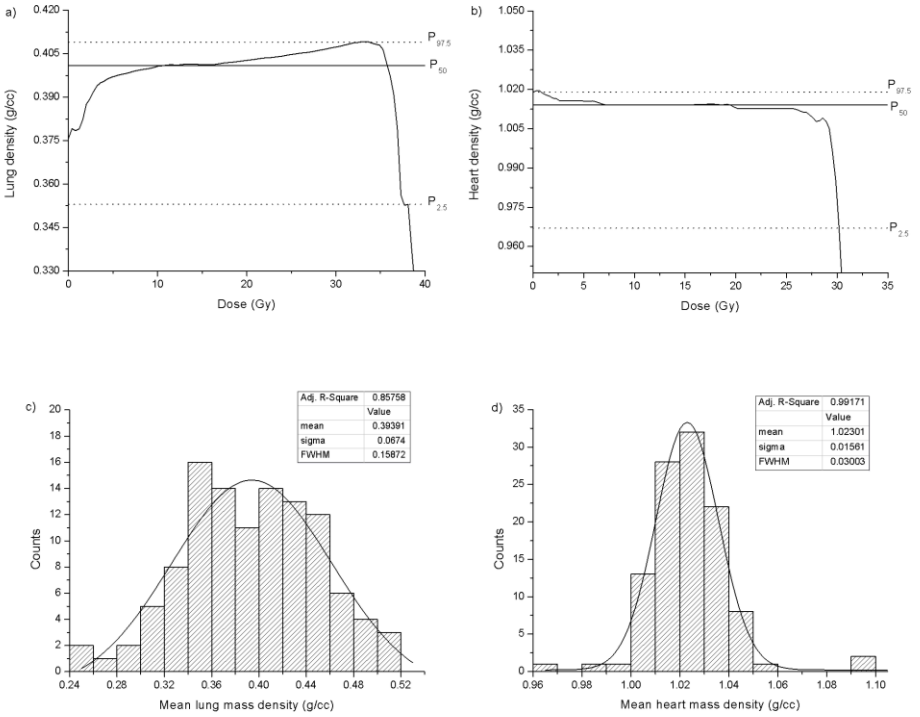

Figure 4.34. Dose-mass density function (DMH/DVH) for the lung (a) and heart (b) for one representative patient. Horizontal lines represent median (P50), 2.5th percentile and 97.5th percentile. Distribution of the means of dose-mass density functions for the lung (c) and for the heart (d) calculated for all patients. For both distributions, at the 0.05 level, the data were significantly drawn from a normally distributed population (Kolmogorov-Smirnov normality test) [146].

The Atlas of Complication Incidence (ACI) method was adopted for reporting toxicity and dose-volume data [147]. For each organ, ACI maps and the associated

probabilities maps for RILF endpoint were generated, as described by Jackson et al., using all patients DMH and DVH (Figure 4.35). The probability maps exhibit areas at high risk for RILF (true complication rate ≥ 20%) at different dose-volume or dose–mass combinations, both in the low dose and in high dose regions.

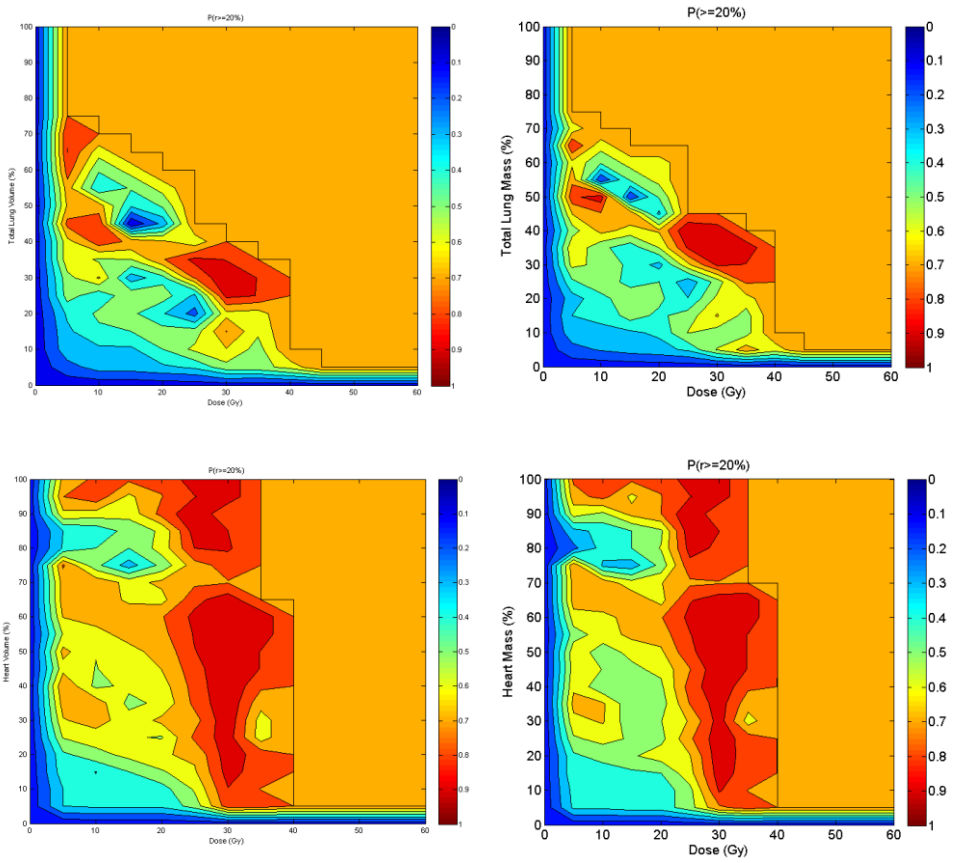

Figure 4.35. Probability maps of RILF incidence obtained using total lung DVH and DMH (upper panel) and using heart DVH and DMH (inferior panel). Iso-probability lines are calculated for a tolerance rate of 20%. The top-right most line, corresponding to the value 0.8, marks the edge of the area of no DVHs/DMHs data.

To derive the best NTCP multivariable model, as a first step, univariate logistic regression analysis for each candidate prognostic (clinical and dosimetric) variable was performed by Spearman's rank correlation coefficient (R_s). Only the variables most highly correlated with RILF (R_s > 0.18) were included in the subsequent analysis. Highly inter-correlated variables (correlation ≥ 0.85) were further removed keeping only the variables with the higher correlation with RILF to avoid a collinearity problem.

Subsequently, we applied multivariate logistic regression methods for NTCP models with the bootstrapping approach in a manner of forward feature selection, and bootstrap resampling to test selection stability.

The bootstrap method suggested a 3–variable model as the optimal one for RILF prediction (Figure 4.36a).

The two models most frequently selected (selection frequency 44.3% vs. 42.3%) by bootstrap sampling included as common features age and heart M_{30}, in combination with left lung V5 (model 1, AUC = 0.78, R_s = 0.35, p < .001) or, alternatively, the total lung $D_{2\%}$ (model 2, AUC = 0.80, R_s = 0.38, p< .001) as shown in Figure 4.35b. Selected variables, regression coefficients and odds ratios (ORs) for both models are given in Table 4.12 along with the models' performance measures.

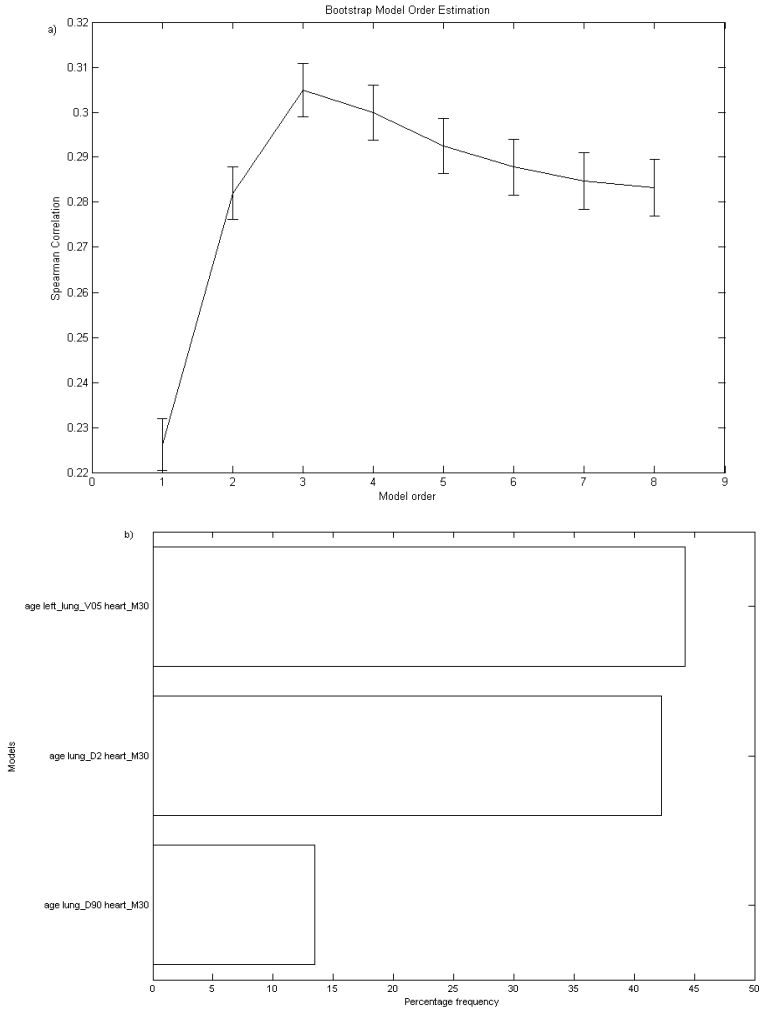

Figure 4.36. Multivariate bootstrap model order estimation and model selection frequency for the three most selected models.

Table 4.12. Best-fitted regression coefficients and odds ratios (OR) for NTCP model 1 and model 2 Performance measures for each model are reported.

		Model 1		
Parameter	Estimated coefficient	SE	*p*-value	OR
Age	.062	.022	.006	1.064
Heart M_{30} (%)	.026	.009	.004	1.027
Left lung V_5 (%)	.027	.016	.094	1.027
Constant	-5.51			
Performance				
R_s	.347			
AUC (95% CI)	.78 (.65-.91)			
Discrimination value	.20			

		Model 2		
Parameter	Estimated coefficient	SE	*p*-value	OR
Age	.068	.023	.003	1.070
Heart M_{30} (%)	.022	.010	.026	1.022
Lung $D_{2\%}$ (Gy)	.115	.084	.171	1.122
Constant	-8.148			
Performance				
R_s	.376			
AUC (95% CI)	.80 (.69-.91)			
Discrimination value	.18			

4.5.5 Dose-surface analysis for prediction of severe acute radio-induced skin toxicity in breast cancer patients

We evaluated 140 consecutive BC patients undergoing conventional three-dimensional conformal 3DCRT after breast conserving surgery in a prospective study assessing severe acute radiation-induced skin toxicity (RIST). The acute RIST was classified according to the RTOG scoring system. Dose-surface

histograms (DSHs) of the body-structure in the breast region were extracted as representative of skin irradiation.

NTCP modeling by Lyman-Kutcher-Burman (LKB) and by multivariate logistic regression using resampling techniques was performed. Models were evaluated by Spearman R_s coefficient and ROC area. By the end of RT, G3 RIST was found in 11 of 140 (8%) patients. Using DSHs for LKB model of RIST severity (RTOG G3vsG2-1), parameter estimates were TD_{50} = 39 Gy, n = 0.38 and m = 0.14 [R_s=0.25, area under the curve AUC = 0.77, p = 0.003]. On multivariate analysis the most predictive model of RIST severity was a 2-variable model and included the skin receiving ≥ 30 Gy (S_{30}) and psoriasis [R_s = 0.32, AUC = 0.84, p < .001].

In Figure 4.37 we reported the ROC curves of the two models, the values of the parameters for LKB model and the best fit coefficients for logistic model were reported in Table 4.13. We obtained similar good prediction performances for both NTCP modeling approaches as shown by R_s and AUC values and by ROC curves. Logistic regression model including a dosimetric factor and psoriasis as a clinical variable has a slightly better performance. However, the difference between the AUC values has not statistical significance at the Z-test.

In conclusion, we found that the calculation of DSHs represents an extremely valuable tool to take into account the dose received by the skin. Robust NTCP models for skin toxicity can be derived using the body DSHs of the irradiated area. A good prediction performance for acute RIST was obtained using a data-driven multivariate model including breast skin S_{30} and psoriasis.

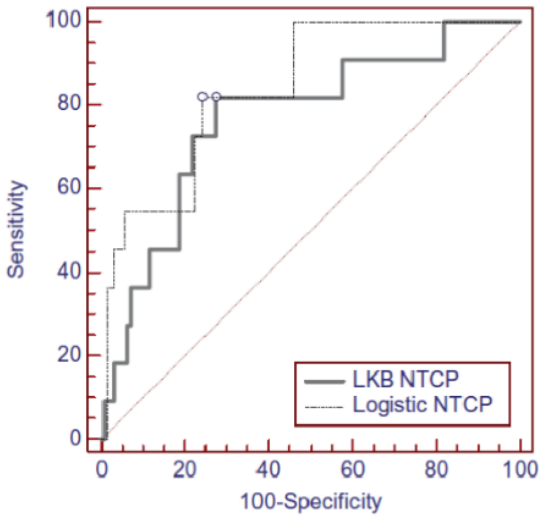

Figure 4.37. ROC curves for LKB and logistic models.

Table 4.13. NTCP models: parameters estimates and 95% confidence intervals of LKB model and best-fit coefficients for logistic model with odds ratios. Performance measures for LKB and logistic NTC models.

NTCP model			R_S	p-value	AUC	95% CI
LKB			0.25	<0.001	0.77	0.62-0.92
Parameter	*Value*	*95% CI*				
TD50	39.0	37.1-41.4				
m	0.14	0.10-0.17				
n	0.38	0.31-0.44				

Logistic

Parameter	*Coefficient*	*SE*	*p-value*	*OR*
Psoriasis	2.68	0.74	<0.001	14.54
S_{30} (%)	0.18	0.08	0.026	1.20
Constant	-15.54	5.75	0.007	

Conclusions and perspectives

The work described in this thesis focused on dosimetric optimization in radiation therapy. Precise dose detection as well as risk prediction of radiation induced side effect has a key role in the success of a radiotherapy treatment.

As first step we investigated the use of optical fiber sensors as radiation dosimeters. In particular, we investigated the effect of ionizing radiation on germane-silicate optical fibers. The interaction process between ionizing radiation and the sensor material was modelled and the physical quantities involved in the interaction identified. The water equivalency property, over the energy range of clinical interest, was assessed by the calculation of the effective atomic number of the fiber materials. Our results demonstrate that the optical fiber sensor can be considered radiologically water equivalent for dosimetry in the clinical dose levels.

After the assessment of the radiological properties of optical fiber material, we investigated the response of the passive fiber-optic sensors based on Fiber Bragg-Gratings to gamma-rays, generated by a 6 MV medical linear accelerator in the dose level range of 0 - 30 Gy. The interrogation of the optical fiber sensors revealed that the effect of the exposure to ionizing radiation is a change of both the refractive index and thermo-optic response of the fiber grating itself. In particular, the variations of the thermo-optic coefficient showed a linear trend as a function of the dose. Exploiting this effect, an ultimate detection limit of 160 mGy was demonstrated. We then extended the investigation on passive optical fiber dosimetry exploiting the detection response of an optical fiber resonator formed by two identical FBGs. The thermo-optic response for doses in the range of 5-20 Gy showed an evident dependence of the slope of the curves on the dose. The experiment has been performed with a 2-cm long fiber providing a detection limit of 180 mGy/cm, but, in principle, longer fibers can be used to increase the irradiated length and thus the sensitivity. This configuration opens the way to a new class of very sensitive, cheap and disposable dosimeters based on doped fibers. The fiber could be irradiated alone and then placed within a fiber cavity made up of two FBGs or a fiber-loop. The sensitive fiber could reach harsh and hardly accessible regions in a minimally invasive manner, such as in medical settings or

industrial equipment. On the contrary, a grid of fibers could be placed over large areas, embedded in large structures or underground, e.g., in environmental monitoring and radioprotection applications. The results of the investigation has demonstrated the great potential of optical fiber sensors in radiation therapy procedures as well as in radiation monitoring and protection in medicine, aerospace, and nuclear power plant. Thanks to their properties, such optical fiber detector could be also applied for real time internal *in-vivo* dosimetry. When special radiation treatment technique are employed, as the Intraoperative Electron Radiation Therapy (IOERT) using high energy and high dose-per-pulse electron beams, dose-rate independent dosimeters are necessary. In this framework, in order to check *in-vivo* dosimetry capabilities of optical fiber sensors is necessary to compare their performance with dosimeters currently adopted for *in-vivo* dosimetry. Thermoluminescent dosimeters (TLDs) are routinely used in standard external beam radiotherapy but their employment in IOERT has not been completely investigated yet. Consequently, thermoluminescent response of TLD-100 to IOERT electron beams was first investigated. Our study proved that the TLD dose response in high dose-per-pulse electron beams has a parabolic behavior for doses under 10 Gy demonstrating TLD-100 may be useful detectors for IOERT patient dosimetry if a proper calibration is provided.

The accuracy of the verification of the delivered dose is strictly linked to clinical efficacy of radiotherapy treatments. However, the optimization of radiation treatment also requires the improving of the balance between the tumor control probability (TCP) and the normal tissue complication probability (NTCP), i.e. maximizing tumor control while maintaining tissue complications at an acceptable level. In the present work different toxicity endpoints were considered with the aim of establishing NTCP models for radiation induced side-effects. We evaluated the radiation induced effects on organs-at-risk such as thyroid, heart, lung and rectum. Applying advanced machine learning technique, we developed multivariable NTCP logistic models which take into account relationships among different patient-related (i.e. age, gender, assumption of drugs, organ volumes) and dosimetric factors. The predictive performance of the data-driven multivariable models resulted to be higher than that obtained with classical models based only on organ dose distribution. These results confirm the importance of considering both dosimetric and patient specific clinical factors in the prediction of radio induced complications. Interestingly, the study of heart valve dysfunction in Hodgkin lymphoma survivors, besides the heart dosimetric parameters and cardiac

volumes, establishes the statistical importance of the lung volume size in the risk prediction. We found that the risk decreases as the lung volume increases supporting the hypothesis of a reserve capacity in the lung (functional reserve) together with a cardiac effect indirectly caused by lung irradiation. This result suggested us to explore the impact of heart irradiation on the risk of pulmonary complications. Considering lung fibrosis as outcome we obtained a multivariable model including a dose/volume parameter of the heart. Our results suggest that both heart and lung irradiation plays a fundamental role in the risk of developing valvular disease as well as lung fibrosis. Radiation-induced fibrosis of the lung and its vessels may affect cardiac functions. A heart-lung interaction in radio-induced toxicity to cardiopulmonary system have been evidenced and an indirect effect of the chest irradiation on the cardiovascular system has been recognized. Multi-organ interaction in affecting organ diseases, suggests the need to consider the normal tissue complication modelling a complex process involving multiple biological pathways and systems.

The obtained results pave the way to further studies. In the perspective of using optical detectors for *in-vivo* dosimetry in real time, we planned to perform on line reading with a portable reading unit with photons and electron beams. In order to re-use the optical fiber dosimeter after reaching the saturation level, an appropriate annealing process to re-generate the optical fiber sensors will be investigated.

Furthermore, to better clarify the relationship between organs (lung and heart) in the development of radiation induced toxicity, larger datasets and innovative image-based approaches will be considered. A further purpose of our research is to overcome the limit of current DVH-based models for toxicity prediction. Due to lack of spatial information of the DVH, these models are not able to correlate the treatment outcome with the spatial dose distribution. We plan to propose a new framework using a voxel-based approach to investigate the relationship between local dose and toxicity. This promising approach provide the way forward for complex voxel-based toxicity models based on more accurate inter-individual matching.

Appendix A

Table A1. Overview of dosimetry systems [6] http://dx.doi.org/10.6028/jres.118.021.

Dosimeter type	Applications	Advantages	Possible Disadvantages	Absorbed Dose Range	Uncertainty	Physical Resolution
Air-filed Ionization Chambers	• Radiation machine characterization (commissioning) • Absolute dose calibration (cGy/min, cGy/MU) • Quality Assurance (QA)	• Provides measurements traceable to Primary Standard Dosimetry Lab (PSDL) and Accredited Dosimetry Calibration Labs (ADCL) • Excellent reference class instruments. Reproducibility of the order of 0.5% or better • High precision and accuracy • Large selection of active volumes, vendors and models commercially available • Charge to dose corrections well understood • Dose rate independent • Energy dependence between 50 keV and 2 MeV is relatively constant • Instant readout • Waterproof models available	• High voltage and cables required (up to 1000 V) • Relatively large volume of some models • Fragile – must be handled with care	< 0.001 Gy to >1000 Gy	1% to 5%	≈ 1mm to 5mm depending on physical air volume
Radiographic Film	• Imaging • Qualitative and quantitative Dosimetry • Measurements in solid water and anthropomorphic phantoms	• Superb 2D spatial resolution • Measurement of planar dose distributions • Dose rate independent • Variety of film types with broad range of linear response to irradiation • Good measurements of radiation field size and flatness and symmetry	• Darkroom for processing required • Processing complex to control • For identical irradiation conditions response varies between film types and batches • Dose calibration against ion chamber required • Energy dependence • Sensitive to visible light • Not reusable • Great care in processing and batch calibration if used for dose calibration	0.1 – 5 Gy	2% to 5%	Capable of sub-millimeter resolution depending on the properties of the reading device
Radiochromic Film	• Imaging • Qualitative and quantitative Dosimetry Measurements in solid and liquid water and anthropomorphic phantoms	• Self-processing • Insensitive to visible light • Tissue equivalent • Energy independent • Dose rate independent • Super 2D spatial resolution • Measurement of planar dose distributions • Good measure of radiation field size and flatness and symmetry • Relatively easy to read with current flatbed scanners	• For identical irradiation conditions response varies between film types and batches • Dose calibration against ion chamber required • Not reusable • Great care handling film and scanner if used for dose calibration • When flatbed scanners are used, well defined protocols must be followed to disable the scanner imaging optimization features	0.1 – 200 Gy	1% to 5%	Capable of sub-millimeter resolution depending on the properties of the reading device
Thermo-luminescent Detectors (TLD)	• *In vivo* dosimetry • Measurements in anthropomorphic and slab phantoms • Intercomparisons between centers	• Small size – point dose measurements • Multiple measurements points in a single irradiation • Various forms and compositions available • Reusable after thermal annealing	• Time consuming calibration • Delayed readout • Elaborate care for accurate readout • Signal erased during readout • For identical irradiation conditions response varies within the same batch • Light sensitivity • Fading – signal loss over time for some materials	0.0005 to 200 Gy Supralinear range > 5 Gy	1.5% to 5% (w/93% confidence)	Typically limited to 2 mm to 5mm resolution depending on the physical size detector
Optically Stimulated Luminescent Detectors (OSLD)	• *In vivo* dosimetry • Measurements in anthropomorphic and slab phantoms • Intercomparisons between centers	• Moderate size – point dose measurements • Multiple measurement points in a single irradiation • Fast readout • Multiple readouts possible • Dose rate independent	• Sensitivity to light – light-tight requirement prior to readout • Supralinear response at high doses • Limited selection of vendors • Not recommended for dose calibration • Energy dependence	0.005 – 10 Gy	1.1% to 3.7%	Typically limited to 2 mm to 5mm resolution depending on the physical size detector
Silicon Diodes	• *In vivo* dosimetry • Small field dosimetry • Detector arrays • Relative dosimetry (depth dose, profiles, output)	• Moderate size – point dose measurements • Instant readout • Great sensitivity relative to ion chambers • No external bias voltage	• Connecting cables required • Variability of calibration with temperature • Directional dependence • Special care needed for constancy of response • Cannot be used for dose calibration • Changes in sensitivity with high dose accumulation	0.005 – 10 Gy	3% to 5%	Capable of ≈ 0.5 mm resolution while maintaining adequate sensitivity
Metal Oxide Semiconductors Field Effect Transistor (MOSFET)	• *In vivo* dosimetry • Small field dosimetry • Detector arrays	• Small size – point dose measurements • Multiple measurements points in a single irradiation • Great sensitivity compared to ion chambers • Fast readout	• Calibration needed for every dosimeter • Energy dependence • Temperature dependence • Directional dependence • Not to be used for dose calibration	0.005 – 10 Gy	3% to 5%	Capable of ≈ 0.5 mm resolution while maintaining adequate sensitivity
Diamond Detectors	• *In vivo* dosimetry • Small field dosimetry • Relative dosimetry (depth dose, profiles, output)	• Small size – point dose measurements • Tissue equivalent • High sensitivity • Resistance to radiation damage	• Bias voltage and cables required • Require pre-irradiation • Variability among dosimeters • Not recommended for dose calibration • Hard to obtain	0.005 – 10 Gy	1.3% to 3%	≈ 5 mm
Alanine – Electron Paramagnetic Resonance Detectors	• *In vivo* dosimetry • Measurements in anthropomorphic and slab phantoms • Intercomparisons between centers	• Tissue equivalent • Readout non-destructive • No fading	• Dose readout requires special equipment or must be done by a primary laboratory	10 – 150000 Gy	1.5% to 4%	≈ 0.2 mm to 5 mm
Gel Dosimetry Detectors	• Measurements in complex geometries • Intercomparisons between centers	• Tissue equivalent • Gel acts as both phantom and dosimeter • True 3D dose distribution	• Complex preparation and evaluation • Post-irradiation diffusion of ions and polymerization • limited accuracy and reproducibility • Not to be used for dose calibration	0.005 – 10 Gy	5% to 10%	Typically tens of cm

Appendix B

Table B1. QUANTEC Summary Table-Dose/Volume/Outcome Data for Several Organs Following Conventional Fractionation.

Organ	Endpoint	Dose (Gy), or dose/volume parameters	Rate (%)	Volume segmented	Irradiation type (partial organ unless otherwise stated)
Brain	Symptomatic necrosis	Dmax <60	<3	Whole organ	3D-CRT
		Dmax = 72	5		
		Dmax = 90	10		
Brain stem	Permanent cranial neuropathy or necrosis	Dmax <54	<5	Whole organ	Whole organ
		D1–10 cc * ≤59	<5		3D-CRT
		Dmax <64 Point dose <<1 cc	<5		3D-CRT
Optic nerve/ chiasm	Optic neuropathy	Dmax <55	<3	Whole organ	Given the small size, 3D-CRT is often whole organ
		Dmax 55–60	3–7		
		Dmax >60	>7-20		
Spinal cord	Myelopathy	Dmax = 50	0.2	Partial organ	3D-CRT
		Dmax = 60	6		
		Dmax = 69	50		
Cochlea	Sensory neural hearing loss (hearing at 4 kHz)	Mean dose ≤45	<30	Whole organ	Given the small size, 3D-CRT is often whole organ
Parotid	Long term parotid salivary function reduced to <25% of pre-RT level	Mean dose <25 (for combined parotid glands)**	<20	Bilateral whole parotid glands	3D-CRT
		Mean dose <20 (for single parotid gland)**	<20	Unilateral whole parotid gland	
		Mean dose <39 (for combined parotid glands)**	<50	Bilateral whole parotid glands	
Pharynx constrictors	Symptomatic dysphagia and aspiration	Mean dose <50	<20	Pharyngeal constrictors	Whole organ

Larynx	Vocal dysfunction (with chemo, based on single study)		Dmax <66	<20	Whole organ	3D-CRT
	Aspiration (with chemo, based on single study)		Mean dose <50	<30		
	Edema (without chemo, based on single study in patients without larynx cancer)		Mean dose <44	<20		
			V50 <27%	<20		
Lung	Symptomatic pneumonitis		V20 ≤ 30% (for combined lung)	<20	Whole organ	3D-CRT
			Mean dose = 7	5		3D-CRT (excludes purposeful whole lung irradiation)
			Mean dose = 13	10		
			Mean dose = 20	20		
			Mean dose = 24	30		
			Mean dose = 27	40		
Esophagus	Grade ≥3 acute esophagitis		Mean dose <34	5–20	Whole organ	3D-CRT
	Grade ≥2 acute esophagitis		V35 <50%	<30		
			V50 <40%	<30		
			V70 <20%	<30		
Heart	Pericarditis (based on single study)		Mean dose <26	<15	Pericardium	3D-CRT
			V30 <46%	<15		
	Long-term cardiac mortality		V25 <10%	<1	Whole organ	
Liver	Classic RILD ***	Excluding patients with pre-existing liver disease or HCC	Mean dose <30-32	<5	Whole liver –GTV	3D-CRT or whole organ
			Mean dose <42	<50		3D-CRT
		In patients with Child-Pugh A preexisting liver disease or HCC, excluding hepatitis B reactivation as an endpoint	Mean dose <28	<5		3D-CRT or whole organ
			Mean dose <36	<50		3D-CRT
Kidney (Non-TBI)	Clinically relevant renal dysfunction		Mean dose <15–18	<5	Bilateral whole kidney	Bilateral whole organ or 3D-CRT
			Mean dose <28	<50		Bilateral whole organ
			V12 <55% (for combined kidney) V20 <32% V23 <30% V28 <20%	<5		3D-CRT
Stomach	Ulceration		D100* <45	<7	Whole organ	Whole organ

Small bowel	Grade ≥ 3 acute toxicity (with combined chemotherapy)		V15 <120 cc	<10	Individual small bowel loops (not the entire potential peritoneal space)	3D-CRT
			V45 <195 cc	<10	Entire potential space within peritoneal cavity	
Rectum (Prostate cancer treatment)	Grade ≥ 2 late toxicity Grade ≥ 3 late toxicity		V50 <50%	<15 <10	Whole organ	3D-CRT
	Grade ≥ 2 late toxicity Grade ≥ 3 late toxicity		V60 <35%	<15 <10		
	Grade ≥ 2 late toxicity Grade ≥ 3 late toxicity		V65 <25%	<15 <10		
	Grade ≥ 2 late toxicity Grade ≥ 3 late toxicity		V70 <20%	<15 <10		
	Grade ≥ 2 late toxicity Grade ≥ 3 late toxicity		V75 <15%	<15 <10		
Bladder	Grade ≥ 3 late RTOG	Bladder cancer treatment:	Dmax <65	<6	Whole organ	3D-CRT
		Prostate cancer treatment:	V65 ≤50 % V70 ≤35 % V75 ≤25 % V80 ≤15 %			
Penile bulb	Severe erectile dysfunction		Mean dose to 95% of gland <50	<35	Whole organ	3D-CRT
			D90*<50	<35		
			D60-70 <70	<55		

Vx is the volume of the organ receiving ≥ x Gy.
*Dx = minimum dose received by the "hottest" x% (or x cc's) of the organ.
**Severe xerostomia is related to additional factors including the doses to the submandibular glands.
***Classic Radiation induced liver disease (RILD) involves anicteric hepatomegaly and ascites, typically occurring between 2 weeks and 3 months after therapy. Classic RILD also involves elevated alkaline phosphatase (more than twice the upper limit of normal or baseline value).
HCC - hepatocellular carcinoma

Clinically, these data should be applied with caution. Clinicians are strongly advised to use the individual QUANTEC articles to check the applicability of these limits to the clinical situation at hand. They largely do not reflect modern IMRT.
http://www.redjournal.org/issues?issue_key=S0360-3016%2810%29X0002-5

Appendix C

In Figure C.1 we reported the algorithm for the calculation of the LKB and RS NTCP model parameters with a brief description of the main functions.

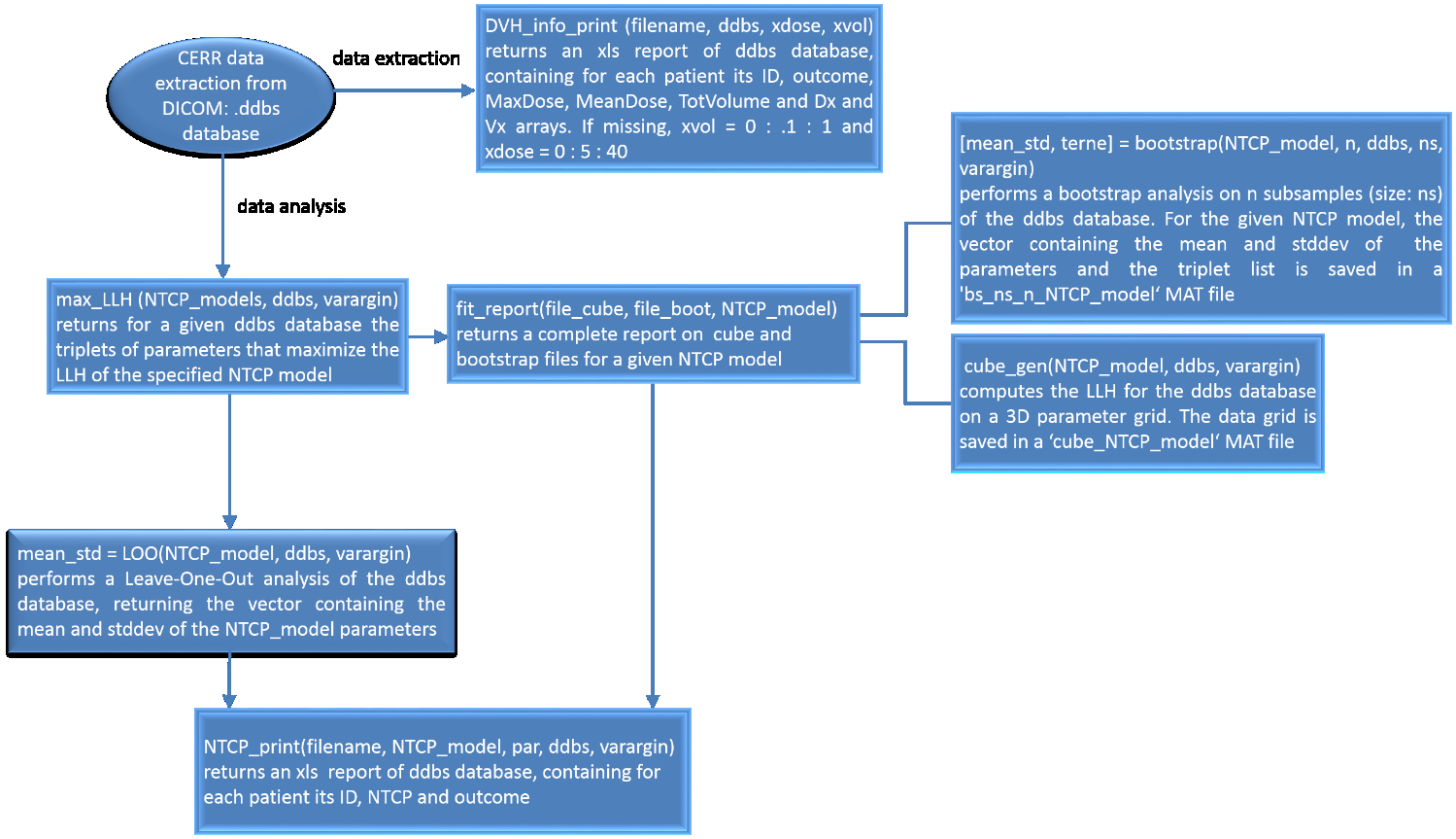

Figure C1. Algorithm for data manipulation and for computation of LKB and RS NTCP model parameters. The start point is the CERR data extraction from DICOM plans to .ddbs database. Once the parameters have been generated by the bootstrap or LOO method. a .xls file is returned by the function NTCP_print containing the NTCP values for each patient.

List of Figures

List of Tables

Bibliography

1. Webb, S., *Advances in three-dimensional conformal radiation therapy physics with intensity modulation*. Lancet Oncol, 2000. **1**(1): p. 30-6.
2. Das, I.J., G.X. Ding, and A. Ahnesjo, *Small fields: nonequilibrium radiation dosimetry*. Med Phys, 2008. **35**(1): p. 206-15.
3. Boyer, A.L., et al., *Intensity-modulated radiotherapy: Current status and issues of interest*. International Journal of Radiation Oncology Biology Physics, 2001. **51**(4): p. 880-914.
4. Sanchez-Doblado, F., et al., *Ionization chamber dosimetry of small photon fields: a Monte Carlo study on stopping-power ratios for radiosurgery and IMRT beams*. Phys Med Biol, 2003. **48**(14): p. 2081-99.
5. Aspradakis, M.M., G.D. Lambert, and A. Steele, *Elements of commissioning step-and-shoot IMRT: delivery equipment and planning system issues posed by small segment dimensions and small monitor units*. Med Dosim, 2005. **30**(4): p. 233-42.
6. Desrosiers, M., et al., *The Importance of Dosimetry Standardization in Radiobiology*. Journal of Research of the National Institute of Standards and Technology, 2013. **118**.
7. Higgins, P.D., et al., *Deconvolution of detector size effect for small field measurement*. Med Phys, 1995. **22**(10): p. 1663-6.
8. Garcia-Vicente, F., J.M. Delgado, and C. Peraza, *Experimental determination of the convolution kernel for the study of the spatial response of a detector*. Med Phys, 1998. **25**(2): p. 202-7.
9. Agency, I.A.E., *Development of Procedures for In vivo Dosimetry in Radiotherapy*. IAEA report. 2013, Vienna: International Atomic Energy Agency. x, 185 p.
10. Kawasaki, B.S., et al., *Narrow-band Bragg reflectors in optical fibers*. Opt Lett, 1978. **3**(2): p. 66-8.
11. Butson, M.J., et al., *A new radiotherapy surface dose detector: The MOSFET*. Medical Physics, 1996. **23**(5): p. 655-658.

12. Weaver, R.D., B.J. Gerbi, and K.E. Dusenbery, *Evaluation of Dose Variation during Total Skin Electron-Irradiation Using Thermoluminescent Dosimeters*. International Journal of Radiation Oncology Biology Physics, 1995. **33**(2): p. 475-478.
13. Tailor, R.C., et al., *Lessons from the in-vivo TLD dosimetry practice for patients treated with total skin electron radiation therapy (TSEB) at MD Anderson Cancer Center*. International Journal of Radiation Oncology Biology Physics, 2006. **66**(3): p. S716-S717.
14. Mandiraji, G.A., et al., *Optical fiber based dosimeter sensor: Beyond TLD-100 limits*. Sensors and Actuators a-Physical, 2015. **222**: p. 48-57.
15. Almond, P.R., et al., *AAPM's TG-51 protocol for clinical reference dosimetry of high-energy photon and electron beams*. Med Phys, 1999. **26**(9): p. 1847-70.
16. Mujsolino, S.V., *Absorbed dose determination in external beam radiotherapy: An international code of practice for dosimetry based on standards of absorbed dose to water; technical reports series No. 398*. Health Physics, 2001. **81**(5): p. 592-593.
17. Spencer, L.V. and F.H. Attix, *A theory of cavity ionization*. Radiat Res, 1955. **3**(3): p. 239-54.
18. Seuntjens, J. and F. Verhaegen, *Comments on 'ionization chamber dosimetry of small photon fields: a Monte Carlo study on stopping-power ratios for radiosurgery and IMRT beams'*. Phys Med Biol, 2003. **48**(21): p. L43-5; author reply L46-8.
19. Sauer, O.A. and J. Wilbert, *Measurement of output factors for small photon beams*. Med Phys, 2007. **34**(6): p. 1983-8.
20. AAPM Radiation Therapy Committee. Task Group 24. and AAPM Radiation Therapy Committee. Task Group 22., *Physical aspects of quality assurance in radiation therapy*. AAPM report,. 1984, New York, NY: Published for the American Association of Physicists in Medicine by the American Institute of Physics. 63 p.
21. International Commission on Radiation Units and Measurements, *Determination of absorbed dose in a patient irradiated by beams of X or gamma rays in radiotherapy procedures*. ICRU report. 1976, Washington: International Commission on Radiation Units and Measurements. vii, 67 p.

22. Bentzen, S.M., et al., *Quantitative Analyses of Normal Tissue Effects in the Clinic (QUANTEC): an introduction to the scientific issues.* Int J Radiat Oncol Biol Phys, 2010. **76**(3 Suppl): p. S3-9.
23. Marks, L.B., et al., *Use of Normal Tissue Complication Probability Models in the Clinic.* International Journal of Radiation Oncology Biology Physics, 2010. **76**(3): p. S10-S19.
24. Emami, B., et al., *Tolerance of normal tissue to therapeutic irradiation.* Int J Radiat Oncol Biol Phys, 1991. **21**(1): p. 109-22.
25. Deasy, J.O., C.S. Mayo, and C.G. Orton, *Treatment planning evaluation and optimization should be biologically and not dose/volume based.* Med Phys, 2015. **42**(6): p. 2753.
26. Lyman, J.T., *Complication probability as assessed from dose–volume histograms.* Radiat Res Suppl, 1985. **8**: p. S13–9.
27. Burman, C., et al., *Fitting of normal tissue tolerance data to an analytic function.* Int J Radiat Oncol Biol Phys, 1991. **21**(1): p. 123-35.
28. Kutcher, G.J., et al., *Histogram reduction method for calculating complication probabilities for three-dimensional treatment planning evaluations.* Int J Radiat Oncol Biol Phys, 1991. **21**(1): p. 137-46.
29. Zaider, M., et al., *Methodology for biologically-based treatment planning for combined low-dose-rate (permanent implant) and high-dose-rate (fractionated) treatment of prostate cancer.* Int J Radiat Oncol Biol Phys, 2005. **61**(3): p. 702-13.
30. Cella, L., et al., *Complication probability models for radiation-induced heart valvular dysfunction: do heart-lung interactions play a role?* PLoS One, 2014. **9**(10): p. e111753.
31. van Luijk, P., et al., *The impact of heart irradiation on dose-volume effects in the rat lung.* Int J Radiat Oncol Biol Phys, 2007. **69**(2): p. 552-9.
32. van Luijk, P., et al., *Radiation damage to the heart enhances early radiation-induced lung function loss.* Cancer Res, 2005. **65**(15): p. 6509-11.
33. Wiegman, E.M., et al., *Loco-regional differences in pulmonary function and density after partial rat lung irradiation.* Radiother Oncol, 2003. **69**(1): p. 11-9.
34. El Naqa, I., et al., *Multivariable modeling of radiotherapy outcomes, including dose-volume and clinical factors.* Int J Radiat Oncol Biol Phys, 2006. **64**(4): p. 1275-86.

35. Defraene, G., et al., *The Benefits of Including Clinical Factors in Rectal Normal Tissue Complication Probability Modeling after Radiotherapy for Prostate Cancer*. International Journal of Radiation Oncology Biology Physics, 2012. **82**(3): p. 1233-1242.
36. Beetz, I., et al., *Development of NTCP models for head and neck cancer patients treated with three-dimensional conformal radiotherapy for xerostomia and sticky saliva: the role of dosimetric and clinical factors*. Radiother Oncol, 2012. **105**(1): p. 86-93.
37. Cella, L., et al., *Multivariate normal tissue complication probability modeling of gastrointestinal toxicity after external beam radiotherapy for localized prostate cancer*. Radiat Oncol, 2013. **8**: p. 221.
38. D'Avino, V., et al., *Prediction of gastrointestinal toxicity after external beam radiotherapy for localized prostate cancer*. Radiat Oncol, 2015. **10**(1): p. 80.
39. Niemierko, A., *Reporting and analyzing dose distributions: a concept of equivalent uniform dose*. Med Phys, 1997. **24**(1): p. 103-10.
40. Agrawal, G.P., *Fiber-optic communication systems*. 2nd ed. Wiley series in microwave and optical engineering. 1997, New York: Wiley. xviii, 555 p.
41. Hill, K.O., F. Y., and D.C.a.K.B.S. Johnson, *Photosensitivity in optical fiber waveguides: Application to reflection filter fabrication* Appl. Phys. Lett, 1978. **32**(10).
42. Meltz, G., W.W. Morey, and W.H. Glenn, *Formation of Bragg gratings in optical fibers by a transverse holographic method*. Opt Lett, 1989. **14**(15): p. 823-5.
43. Zachariasen, W.H., *The atomic arrangement in glass*. J. Am. Chem. Soc. , 1932. **54**.
44. Salh, R., *Defect Related Luminescence in Silicon Dioxide Network: A Review*. Crystalline Silicon - Properties and Uses. 2011.
45. Stevens-Kalceff, M.A., *Electron-irradiation-induced radiolytic oxygen generation and microsegregation in silicon dioxide polymorphs*. Physical Review Letters, 2000. **84**(14): p. 3137-3140.
46. Lu, Z.Y., et al., *Structure, properties, and dynamics of oxygen vacancies in amorphous SiO2*. Phys Rev Lett, 2002. **89**(28 Pt 1): p. 285505.
47. Weeks, R.A., *Paramagnetic Resonance of Lattice Defects in Irradiated Quartz*. J. Appl. Phys., 1956. **27**.

48. Griscom, D.L., E.J. Friebele, and G.H. Sigel Jr., *Observation and analysis of the primary ^{29}Si hyperfine structure of the E′ center in non-crystalline SiO_2*. Solid State Communications, 1974. **15**(3): p. 479-483.
49. Hanafusa, H., Y. Hibino, and F. Yamamoto, *Formation mechanism of drawing-induced E' centers in silica optical fibers*. J. Appl. Phys., 1985. **58**.
50. Hibino, Y. and H. Hanafusa, *ESR Study on E'-Centers Induced by Optical Fiber Drawing Process*. Jpn. J. Appl. Phys., 1983. **22**.
51. Stapelbroek, M., et al., *Oxygen-associated trappedhole centers in high-purity fused silicas*. J. Non-Cryst. Solids 1979. **32**.
52. Friebele, E.J., et al., *Fundamental Defect Centers in Glass: The Peroxy Radical in Irradiated, High-Purity, Fused Silica*. Phys. Rev. Lett., 1979. **42**.
53. Griscom, D.L., *Radiation hardening of pure-silica-core optical fibers: Reduction of induced absorption bands associated with self-trapped holes*. Applied Physics Letters, 1997. **71**(2): p. 175-177.
54. Skuja, L., *Isoelectronic Series of Twofold Coordinated Si, Ge, and Sn Atoms in Glassy Sio2 - a Luminescence Study*. Journal of Non-Crystalline Solids, 1992. **149**(1-2): p. 77-95.
55. Neustruev, V.B., *Colour centres in germanosilicate glass and optical fibres*. J. Phys. Condens. Matter, 1994. **6**(35): p. 6901.
56. Carbonaro, C.M., V. Fiorentini, and F. Bernardini, *Stability of Ge-related point defects and complexes in Ge-doped SiO2*. Physical Review B, 2002. **66**(23).
57. Fujimaki, M., et al., *Structural changes induced by KrF excimer laser photons in H-2-loaded Ge-doped SiO2 glass*. Physical Review B, 1999. **60**(7): p. 4682-4687.
58. Nishii, J., et al., *Pair generation of Ge electron centers and self-trapped hole centers in GeO2-SiO2 glasses by KrF excimer-laser irradiation*. Physical Review B, 1999. **60**(10): p. 7166-7169.
59. Hosono, H., et al., *Nature and origin of the 5-eV band in SiO_2:GeO_2 glasses*. Phys Rev B Condens Matter, 1992. **46**(18): p. 11445-11451.
60. Nishii, J., et al., *Photochemical reactions in GeO_2-SiO_2 glasses induced by ultraviolet irradiation: Comparison between Hg lamp and excimer laser*. Phys Rev B Condens Matter, 1995. **52**(3): p. 1661-1665.

61. Cannas, M. and G. Origlio, *Ultraviolet optical properties of silica controlled by hydrogen trapping at Ge-related defects*. Physical Review B, 2007. **75**(23).
62. Griscom, D.L., *Trapped-electron centers in pure and doped glassy silica: A review and synthesis*. Journal of Non-Crystalline Solids, 2011. **357**(8-9): p. 1945-1962.
63. Griscom, D.L., *A Minireview of the Natures of Radiation-Induced Point Defects in Pure and Doped Silica Glasses and Their Visible/Near-IR Absorption Bands, with Emphasis on Self-Trapped Holes and How They Can Be Controlled*. Physics Research International, 2013. **2013**: p. 14.
64. Podgoršak, E.B. and International Atomic Energy Agency., *Radiation oncology physics : a handbook for teachers and students*. 2005, Vienna: International Atomic Energy Agency. 657 p.
65. Seltzer, S.M., *Calculation of Photon Mass Energy-Transfer and Mass Energy-Absorption Coefficients*. Radiation Research, 1993. **136**(2): p. 147-170.
66. Manohara, S.R., et al., *On the effective atomic number and electron density: A comprehensive set of formulas for all types of materials and energies above 1 keV*. Nuclear Instruments & Methods in Physics Research Section B-Beam Interactions with Materials and Atoms, 2008. **266**(18): p. 3906-3912.
67. Akkurt, I., et al., *Photon attenuation coefficients of concrete includes barite in different rate*. Annals of Nuclear Energy, 2010. **37**(7): p. 910-914.
68. Crawford, J.H. and L.M. Slifkin, *Point defects in solids*. 1972, Plenum Press New-York.
69. Devine, R.A.B., J.P. Duraud, and E. Dooryhée, *Structure and imperfections in amorphous and crystalline silicon dioxide*. 2000. 528.
70. Gupta, R.P., *Electronic-Structure of Crystalline and Amorphous-Silicon Dioxide*. Physical Review B, 1985. **32**(12): p. 8278-8292.
71. Martin, B., et al., *Electron irradiation damage in quartz, SiO2*. Physics and Chemistry of Minerals, 1996. **23**(7): p. 409-417.
72. Othonos, A., *Fiber Bragg gratings*. Review of Scientific Instruments, 1997. **68**(12): p. 4309-4341.
73. Cuevas, R.F., et al., *Dependence of H-2/O-2 ratio and GeO2 content on the enhancement of second-order non-linearity related defects in Ge-doped*

optical fiber preforms. Materials Science and Engineering B-Solid State Materials for Advanced Technology, 2004. **111**(2-3): p. 135-141.

74. Ho, C.K.F., et al., *Optical functions of (x)GeO2 :(1-x)SiO2 films determined by multi-sample and multi-angle spectroscopic ellipsometry*. Optics Express, 2005. **13**(3): p. 1049-1054.
75. Cuevas, R.F., et al., *Effect of processing parameters on control of defect centers associated with second-order harmonic generation and photosensitivity in SiO2 : GeO2 glass preforms*. Nuclear Instruments & Methods in Physics Research Section B-Beam Interactions with Materials and Atoms, 2006. **247**(2): p. 285-289.
76. Le Parc, R., et al., *Density and concentration fluctuations in SiO(2)-GeO(2) optical fiber glass investigated by small angle x-ray scattering*. Journal of Applied Physics, 2008. **103**(9).
77. Plotnichenko, V.G., et al., *Hydroxyl groups in GeO2 glass*. Inorganic Materials, 2002. **38**(7): p. 738-745.
78. Butov, O.V., et al., *Refractive index dispersion of doped silica for fiber optics*. Optics Communications, 2002. **213**(4-6): p. 301-308.
79. Huston, A.L., et al., *Remote optical fiber dosimetry*. Nuclear Instruments & Methods in Physics Research Section B-Beam Interactions with Materials and Atoms, 2001. **184**(1-2): p. 55-67.
80. Paul, M.C., et al., *Gamma ray radiation induced absorption in Ti doped single mode optical fibres at low dose levels*. Optical Materials, 2007. **29**(6): p. 738-745.
81. Fernandez, A.F., et al., *Real-time fibre optic radiation dosimeters for nuclear environment monitoring around thermonuclear reactors*. Fusion Engineering and Design, 2008. **83**(1): p. 50-59.
82. Jones, A.K. and D. Hintenlang, *Potential clinical utility of a fibre optic-coupled dosemeter for dose measurements in diagnostic radiology*. Radiation Protection Dosimetry, 2008. **132**(1): p. 80-87.
83. Faustov, A., et al., *Highly Radiation Sensitive Type IA FBGs for Future Dosimetry Applications*. Ieee Transactions on Nuclear Science, 2012. **59**(4): p. 1180-1185.
84. Jang, K.W., et al., *Multi-dimensional fiber-optic radiation sensor for ocular proton therapy dosimetry*. Nuclear Instruments & Methods in Physics Research Section a-Accelerators Spectrometers Detectors and Associated Equipment, 2012. **695**: p. 322-325.

85. Sporea, D., et al., *An Electron Beam Profile Instrument Based on FBGs*. Sensors, 2014. **14**(9): p. 15786-15801.
86. Krebber, K., H. Henschel, and U. Weinand, *Fibre Bragg gratings as high dose radiation sensors?* Measurement Science & Technology, 2006. **17**(5): p. 1095-1102.
87. Grattan, K.T.V. and A.W. Palmer, *Optical-Fiber Sensor Technology - a Challenge to Microelectronic Sensors*. Sensors and Actuators a-Physical, 1992. **30**(1-2): p. 129-137.
88. Bartelt, H., *Trends in Bragg Grating Technology for Optical Fiber Sensor Applications*. Measurement Technology and Intelligent Instruments Ix, 2010. **437**: p. 304-308.
89. Alwis, L., T. Sun, and K.T.V. Grattan, *Optical fibre-based sensor technology for humidity and moisture measurement: Review of recent progress*. Measurement, 2013. **46**(10): p. 4052-4074.
90. Peeters, B., et al., *On the use of Optical Fiber Bragg Grating (FBG) Sensor Technology for Strain Modal Analysis*. 11th International Conference on Vibration Measurements by Laser and Noncontact Techniques - Aivela 2014: Advances and Applications, 2014. **1600**: p. 39-49.
91. Gusarov, A.I., et al., *High total dose radiation effects on temperature sensing fiber Bragg gratings*. Ieee Photonics Technology Letters, 1999. **11**(9): p. 1159-1161.
92. Volchek, A.O., A.I. Gusarov, and F.N. Ignatev, *The Influence of Radiation-Induced Distortions of Dielectrical and Mechanical Characteristics of Optical-Materials on the Image Structure*. Optika I Spektroskopiya, 1994. **76**(5): p. 822-827.
93. Henschel, H., O. Kohn, and H.U. Schmidt, *Optical Fibers as Radiation Dosimeters*. Nuclear Instruments & Methods in Physics Research Section B-Beam Interactions with Materials and Atoms, 1992. **69**(2-3): p. 307-314.
94. Piao, F., W.G. Oldham, and E.E. Haller, *The mechanism of radiation-induced compaction in vitreous silica*. Journal of Non-Crystalline Solids, 2000. **276**(1-3): p. 61-71.
95. Buscarino, G., et al., *The role of impurities in the irradiation induced densification of amorphous SiO(2)*. J Phys Condens Matter, 2010. **22**(25): p. 255403.

96. Liu, Y.G. and P.H. Daum, *Relationship of refractive index to mass density and self-consistency of mixing rules for multicomponent mixtures like ambient aerosols*. Journal of Aerosol Science, 2008. **39**(11): p. 974-986.
97. Primak, W., *The compacted states of vitreous silica*. Studies in radiation effects in solids. 1975, New York: Gordon and Breach Science Publishers. xvii, 184 p.
98. Ruller, J.A. and E.J. Friebele, *The Effect of Gamma-Irradiation on the Density of Various Types of Silica*. Journal of Non-Crystalline Solids, 1991. **136**(1-2): p. 163-172.
99. Galeener, F.L., *Nonlinear Gamma-Ray Activation of Defect Spins in Vitreous Silica*. Journal of Non-Crystalline Solids, 1992. **149**(1-2): p. 27-31.
100. Higby, P.L., et al., *Radiation Effects on the Physical-Properties of Low-Expansion-Coefficient Glasses and Ceramics*. Journal of the American Ceramic Society, 1988. **71**(9): p. 796-802.
101. Rothschild, M., D.J. Ehrlich, and D.C. Shaver, *Effects of Excimer Laser Irradiation on the Transmission, Index of Refraction, and Density of Ultraviolet Grade Fused-Silica*. Applied Physics Letters, 1989. **55**(13): p. 1276-1278.
102. Schenker, R., F. Piao, and W.G. Oldham, *Material limitations to 193-nm lithographic system lifetimes*. Optical Microlithography Ix, 1996. **2726**: p. 698-706.
103. Allan, D.C., et al., *Glass densification under 193nm laser exposure: Experiment and theory*. Abstracts of Papers of the American Chemical Society, 1997. **213**: p. 23-Comp.
104. Cella, L., R. Liuzzi, and M. Salvatore, *The Italian affair: The employment of parallel-plate ionization chambers for dose measurements in high dose-per-pulse IORT electron beams*. Medical Physics, 2010. **37**(6): p. 2918-2924.
105. Chen, R. and P.L. Leung, *Nonlinear dose dependence and dose-rate dependence of optically stimulated luminescence and thermoluminescence*. Radiation Measurements, 2001. **33**(5): p. 475-481.
106. Montano-Garcia, C. and I. Gamboa-deBuen, *Measurements of the optical density and the thermoluminescent response of LiF : Mg,Ti exposed to high doses of Co-60 gamma rays*. Radiation Protection Dosimetry, 2006. **119**(1-4): p. 230-232.

107. Massillon-JL, G., I. Gamboa-deBuen, and M.E. Brandan, *Onset of supralinear response in TLD-100 exposed to Co-60 gamma-rays*. Journal of Physics D-Applied Physics, 2006. **39**(2): p. 262-268.
108. Orecchia, R., et al., *Intraoperative electron beam radiotherapy (ELIOT) to the breast: A need for a quality assurance programme*. Breast, 2005. **14**(6): p. 541-546.
109. Wood, J.I., *Computational methods in reactor shielding*. 1st ed. Pergamon international library of science, technology, engineering, and social studies. 1982, Oxford ; New York: Pergamon Press. vii, 441 p.
110. Gowda, S., S. Krishnaveni, and R. Gowda, *Studies on effective atomic numbers and electron densities in amino acids and sugars in the energy range 30-1333 keV*. Nuclear Instruments & Methods in Physics Research Section B-Beam Interactions with Materials and Atoms, 2005. **239**(4): p. 361-369.
111. El-Kateb, A.H., R.A.M. Rizk, and A.M. Abdul-Kader, *Determination of atomic cross-sections and effective atomic numbers for some alloys*. Annals of Nuclear Energy, 2000. **27**(14): p. 1333-1343.
112. Murty, V.R.K., D.P. Winkoun, and K.R.S. Devan, *Effective atomic numbers for W/Cu alloy using transmission experiments*. Applied Radiation and Isotopes, 2000. **53**(4-5): p. 945-948.
113. Akkurt, I., S. Kilincarslan, and C. Basyigit, *The photon attenuation coefficients of barite, marble and limra*. Annals of Nuclear Energy, 2004. **31**(5): p. 577-582.
114. Icelli, O., et al., *Effective atomic numbers for CoCuNi alloys using transmission experiments*. Journal of Quantitative Spectroscopy & Radiative Transfer, 2005. **91**(4): p. 485-491.
115. Singh, K., et al., *Gamma-ray attenuation coefficients in bismuth borate glasses*. Nuclear Instruments & Methods in Physics Research Section B-Beam Interactions with Materials and Atoms, 2002. **194**(1): p. 1-6.
116. Singh, S., et al., *Barium-borate-flyash glasses: As radiation shielding materials*. Nuclear Instruments & Methods in Physics Research Section B-Beam Interactions with Materials and Atoms, 2008. **266**(1): p. 140-146.
117. Singh, N., et al., *Comparative study of lead borate and bismuth lead borate glass systems as gamma-radiation shielding materials*. Nuclear Instruments & Methods in Physics Research Section B-Beam Interactions with Materials and Atoms, 2004. **225**(3): p. 305-309.

118. Singh, K.J., et al., *Gamma-ray shielding and structural properties of PbO-SiO2 glasses*. Nuclear Instruments & Methods in Physics Research Section B-Beam Interactions with Materials and Atoms, 2008. **266**(6): p. 944-948.
119. Gerward, L., et al., *WinXCom - a program for calculating X-ray attenuation coefficients*. Radiation Physics and Chemistry, 2004. **71**(3-4): p. 653-654.
120. Prasad, S.G., K. Parthasaradhi, and W.D. Bloomer, *Effective atomic numbers for photoabsorption in alloys in the energy region of absorption edges*. Radiation Physics and Chemistry, 1998. **53**(5): p. 449-453.
121. Drever, R.W.P., et al., *Laser phase and frequency stabilization using an optical resonator*. Appl. Phys. B, 1983. **31**: p. 97-105.
122. Gay, H.A., et al., *Pelvic Normal Tissue Contouring Guidelines for Radiation Therapy: A Radiation Therapy Oncology Group Consensus Panel Atlas*. International Journal of Radiation Oncology Biology Physics, 2012. **83**(3): p. E353-E362.
123. Feng, M., et al., *Development and validation of a heart atlas to study cardiac exposure to radiation following treatment for breast cancer*. Int J Radiat Oncol Biol Phys, 2011. **79**(1): p. 10-8.
124. Kong, F.M., et al., *Consideration of dose limits for organs at risk of thoracic radiotherapy: atlas for lung, proximal bronchial tree, esophagus, spinal cord, ribs, and brachial plexus*. Int J Radiat Oncol Biol Phys, 2011. **81**(5): p. 1442-57.
125. Moiseenko, V., J.O. Deasy, and J. Van Dyk, *The Modern Technology of Radiation Oncology: A Compendium for Medical Physicists and Radiation Oncologists*, in *Radiobiological modeling for treatment planning*. 2005, J Van Dyk (Madison, WI: Medical Physics Publishing).
126. Hosmer, D.W. and S. Lemeshow, *Applied logistic regression*. 2nd ed. Wiley series in probability and statistics Texts and references section. 2000, New York: Wiley. xii, 373 p.
127. Kleinbaum, D.G., M. Klein, and E.R. Pryor, *Logistic regression : a self-learning text*. 2nd ed. Statistics for biology and health. 2002, New York: Springer. xiv, 513 p.
128. Vittinghoff, E., *Regression methods in biostatistics : linear, logistic, survival, and repeated measures models*. Statistics for biology and health. 2005, New York: Springer. xv, 340 p.

129. McCullagh, P. and J.A. Nelder, *Generalized linear models*. 2nd ed. Monographs on statistics and applied probability. 1998, Boca Raton: Chapman & Hall/CRC. xix, 511 p.
130. Venzon, D.J. and S.H. Moolgavkar, *A Method for Computing Profile-Likelihood-Based Confidence-Intervals*. Applied Statistics-Journal of the Royal Statistical Society Series C, 1988. **37**(1): p. 87-94.
131. Cheung, R., et al., *Characterization of rectal normal tissue complication probability after high-dose external beam radiotherapy for prostate cancer*. International Journal of Radiation Oncology Biology Physics, 2004. **58**(5): p. 1513-1519.
132. Rancati, T., et al., *Fitting late rectal bleeding data using different NTCP models: results from an Italian multi-centric study (AIROPROS0101)*. Radiotherapy and Oncology, 2004. **73**(1): p. 21-32.
133. Peeters, S.T.H., et al., *Rectal bleeding, fecal incontinence, and high stool frequency after conformal radiotherapy for prostate cancer: Normal tissue complication probability modeling*. International Journal of Radiation Oncology Biology Physics, 2006. **66**(1): p. 11-19.
134. Deasy, J.O. and I. El Naqa, *Image-based modeling of normal tissue complication probability for radiation therapy*. Cancer Treat Res, 2008. **139**: p. 215-56.
135. Cella, L., et al., *Multivariate normal tissue complication probability modeling of gastrointestinal toxicity after external beam radiotherapy for localized prostate cancer*. Radiation Oncology, 2013. **8**.
136. Avino, S., et al., *Detecting ionizing radiation with optical fibers down to biomedical doses*. Applied Physics Letters, 2013. **103**(18).
137. Avino, S., et al., *Ionizing Radiation Detectors Based on Ge-Doped Optical Fibers Inserted in Resonant Cavities*. Sensors, 2015. **15**(2): p. 4242-4252.
138. Liuzzi, R., et al., *Evaluation of LiF:Mg,Ti (TLD-100) for Intraoperative Electron Radiation Therapy Quality Assurance*. PLoS One, 2015. **10**(10): p. e0139287.
139. Cella, L., et al., *Development of multivariate NTCP models for radiation-induced hypothyroidism: a comparative analysis*. Radiat Oncol, 2012. **7**: p. 224.
140. Boomsma, M.J., et al., *A prospective cohort study on radiation-induced hypothyroidism: development of an NTCP model*. Int J Radiat Oncol Biol Phys, 2012. **84**(3): p. e351-6.

141. D'Avino, V., et al., *Prediction of gastrointestinal toxicity after external beam radiotherapy for localized prostate cancer*. Radiation Oncology, 2015. **10**.
142. Gulliford, S.L., et al., *Parameters for the Lyman Kutcher Burman (LKB) model of Normal Tissue Complication Probability (NTCP) for specific rectal complications observed in clinical practise*. Radiother Oncol, 2012. **102**(3): p. 347-51.
143. Cella, L., et al., *Multivariate Normal Tissue Complication Probability Modeling of Heart Valve Dysfunction in Hodgkin Lymphoma Survivors*. International Journal of Radiation Oncology Biology Physics, 2013. **87**(2): p. 304-310.
144. Cella, L., et al., *Predicting radiation-induced valvular heart damage*. Acta Oncol, 2015: p. 1-9.
145. Cella, L., et al., *Pulmonary damage in Hodgkin's lymphoma patients treated with sequential chemo-radiotherapy: Predictors of radiation-induced lung injury*. Acta Oncol, 2014. **53**(5): p. 613-9.
146. Cella, L., et al., *Modeling the risk of radiation-induced lung fibrosis: Irradiated heart tissue is as important as irradiated lung*. Radiother Oncol, 2015. **117**(1): p. 36-43.
147. Avino, S., et al., *Radiation dosimetry with fiber Bragg gratings*. 23rd International Conference on Optical Fibre Sensors, 2014. **9157**.